

# Influence of Deep Ocean Ventilation on Northwest Pacific Productivity and Carbonate Preservation Patterns During the Past 500,000 Years

Dissertation

zur Erlangung des Doktorgrades der Naturwissenschaften

am Fachbereich Geowissenschaften

der Universität Bremen

vorgelegt von

Weng-Si (JC) Chao

Colloquium Date : 24<sup>th</sup> February, 2023

Bremen, Jan 2023

Gutachter :

Prof. Dr. Ralf Tiedemann

Prof. Dr. Cristiano M. Chiessi

The work on this PhD thesis was carried out within the Marine Geology section of the Alfred-Wegener-Institut Helmholtz-Zentrum für Polar- und Meeresforschung (AWI) in Bremerhaven between September 2018 and September 2022. The study was embedded in the collaborative project “*SO264 SONNE-EMPEROR: The Plio/Pleistocene to Holocene development of the pelagic North Pacific from surface to depth – assessing its role for the global carbon budget and Earth’s climate*” AWI and GEOMAR Helmholtz-Zentrum für Ozeanforschung Kiel, and funded by the German Federal Ministry of Education and Research (BMBF).

## Versicherung an Eides Statt / *Affirmation in lieu of an oath*

gem. § 5 Abs. 5 der Promotionsordnung vom 18.06.2018 /  
*according to § 5 (5) of the Doctoral Degree Rules and Regulations of 18 June, 2018*

Ich / I, Weng-Si, Chao , Ellhornstraße 39 Bremen , 3199416  
(Vorname / First Name, Name / Name, Anschrift / Address, ggf. Matr.-Nr. / student ID no., if applicable)

versichere an Eides Statt durch meine Unterschrift, dass ich die vorliegende Dissertation selbständig und ohne fremde Hilfe angefertigt und alle Stellen, die ich wörtlich dem Sinne nach aus Veröffentlichungen entnommen habe, als solche kenntlich gemacht habe, mich auch keiner anderen als der angegebenen Literatur oder sonstiger Hilfsmittel bedient habe und die zu Prüfungszwecken beigelegte elektronische Version (PDF) der Dissertation mit der abgegebenen gedruckten Version identisch ist. / *With my signature I affirm in lieu of an oath that I prepared the submitted dissertation independently and without illicit assistance from third parties, that I appropriately referenced any text or content from other sources, that I used only literature and resources listed in the dissertation, and that the electronic (PDF) and printed versions of the dissertation are identical.*

Ich versichere an Eides Statt, dass ich die vorgenannten Angaben nach bestem Wissen und Gewissen gemacht habe und dass die Angaben der Wahrheit entsprechen und ich nichts verschwiegen habe. / *I affirm in lieu of an oath that the information provided herein to the best of my knowledge is true and complete.*

Die Strafbarkeit einer falschen eidesstattlichen Versicherung ist mir bekannt, namentlich die Strafandrohung gemäß § 156 StGB bis zu drei Jahren Freiheitsstrafe oder Geldstrafe bei vorsätzlicher Begehung der Tat bzw. gemäß § 161 Abs. 1 StGB bis zu einem Jahr Freiheitsstrafe oder Geldstrafe bei fahrlässiger Begehung. / *I am aware that a false affidavit is a criminal offence which is punishable by law in accordance with § 156 of the German Criminal Code (StGB) with up to three years imprisonment or a fine in case of intention, or in accordance with § 161 (1) of the German Criminal Code with up to one year imprisonment or a fine in case of negligence.*

Bremen , 16 Jan 2023  
Ort / Place, Datum / Date

JC Chao  
Unterschrift / Signature

## Acknowledgements

” The time you enjoy wasting is not wasted time.”

- Bertrand Russell

First of all, I would like to thank everyone who pay tax in Germany for financing my 1-year Arbeitslosengeld I. It was life-saving and fantastic!

I would like to thank my supervisors Prof. Ralf Tiedemann and Lester Lembke-Jene for offering me this position and including me in this joint project. Thank you for all the effective discussions and great supports, and pointing me the right direction throughout my PhD. I am sure without their continuous support and advice this project will not come to a successful end. I would also like to thank Prof. Dirk Nürnberg for the successful cruise and insightful critiques during all the committee meetings. And a special thanks to Prof. Cristiano Chiessi who is so kind and helpful to me during the final stages of the dissertation process.

Integral part of this thesis has made by the technicians operating and maintain all different machines and equipment in Marine Geology section. Valéa, Lisa, Doro and Walter who I especially want to thank for encouraging and helping me with all the measurements. I also thank Linda, Bryan and Tunde for all the valuable HiWi work and the efforts in the lab. I particular thank Linda and Tjördis for the wonderful time on the cruise and the amazing teamwork and vibes we had. Such a good job you did with your master thesis, Linda! Thank you, Jordan, for all the inspiring chats and meetings. Thanks also to Lara for being the PhD partner of this project and the discussion about science and PhD life. Whatever path the future will drive us on, I still wish you: may the force/forams be with you.

There are many people who have been the pleasant wine to my life and I would like to send my deep thanks to some of them here. The core of the “DogTeam”, Bimo, Jenna, Onur, Olga, thanks for the wonderful DokTeam time and sharing all the crazy and unforgettable memories together. I am grateful to have you all from the beginning and we do our PhD in Germany. My crew from the “Pirates of the canoebean”, Diego and Rita, thank you for all the shots of joy and the food adventures. Thank you, Remi, for being the first person to talk to me on the first day going to AWI and my new neighbor. I’d also like to thank Jessica and Coralie for being with me from the beginning of the cruise to Bremen. The last night in Yokohama was the best night ever in Japan. Thanks to my flat-mates Christian and Ramneek for all the encouraging

nights and drinks, and helping me with the English writing and the German translation. To AnSheng 安昇, the Bremen life won't be a satisfaction without you. Thank you for all the home-like and yummy hot pot nights. My dear friends back in Taiwan, 田田, 張沂, 唐懷昱, 小優 and too many other names that I want to name here, my warmest thanks to our beautiful friendship and all lifesaving chats and video-calls especially during the corona time. This PhD journey will not have been half fruitful as it could be without all your companionship. All this international friendship is, like winter and glühwein, indivisible.

Lastly, my beloved Mark, all your love and company since the summer of 2015 are everything for me. No words can express my gratitude to you. I am truly grateful that I am the lucky one. Thanks for being my family in Germany.

Oh! One more: I would like to deeply thank Deutsche Bahn for fulfilling these four years of commute time. Thank you so much really.

JC

16 Jan 2022

## Abstract

The North Pacific has so far been insufficiently studied comparing to other oceans regarding paleoceanographic variations and its interactions with global climate. In particular, the present deep North Pacific acts as a CO<sub>2</sub> sink, and the productivity regime, the carbonate system and other processes in relation to the carbon cycle are not well understood on long geological time-scales due to the lack of available proxies and records. This thesis aims to improve the understanding of the role of the North Pacific Deep Water (NPDW) in the Meridional Overturning Circulation and its sensitivity and response to upper ocean and atmosphere forcings and feedback mechanisms. Here, I present a series of new sediment records from a meridional transect along the Emperor Seamount Chain and on the Hess Rise in the NW Pacific. As a starting point of this thesis, an X-ray fluorescence (XRF)- and benthic foraminiferal isotope-based stratigraphic framework was developed for the sediment cores in this region. The subsequent proxy reconstructions comprise the last 550,000 years (550 ka BP) and focus on variations in paleo-productivity and the deep sea carbonate depositional environment, as well as deep water mass dynamics associated with carbon storage and outgassing. XRF-based productivity records indicate a southward decrease and an out-of-phase pattern in carbonate deposition below 40°N in the NW Pacific over the last 500 ka BP. It is assumed that regional shifts in the subpolar and subtropical gyre circulation, in close association with upper ocean stratification changes were the major factors determining the nutrient regime in this region. On the other hand, coherent interglacial increases in biogenic barium, carbonate flux, alkenone concentration, sand fraction and opal content in the subpolar region indicate that productivity had a more direct impact and depositional contribution on the carbonate system. The weak correlation between carbonate preservation and productivity on the subtropical gyre influenced Hess Rise, however, matched to the deep Pacific carbonate chemistry fluctuations which relate to carbonate dissolution. This mismatch also implies that the boundary shifted between the subpolar and subtropical gyres, which provided different nutrient regime to the NW Pacific region. Furthermore, I compared the stable isotope data from a monospecific benthic foraminiferal (*Cibicidoides wuellerstorfi*) record which reflects the NPDW to the source water masses in order to reconstruct the deep North Pacific ventilation history. A generally more stagnant glacial NPDW during the last four glacial-interglacial cycles is supported by our record. The  $\delta^{13}\text{C}$  composition ( $\Delta\delta^{13}\text{C}$ ) between NPDW and Circumpolar Deep Water suggests a steady southern water mass contributor, but a long-term change in the inflow strength into the North Pacific. During terminations II to V, a breakdown of the mid-depth to deep

stratification in the NW Pacific was inferred by the abrupt decline in  $\Delta\delta^{18}\text{O}$  between NPDW and North Pacific Intermediate Water (NPIW), however, a similar signal in the ventilation was not clearly observed in  $\Delta\delta^{13}\text{C}$ . Based on  $\Delta\delta^{13}\text{C}$  signals, a rapid ventilation change during MIS 10 to 13 occurred from a relatively strongly ventilated interglacial NPDW to better ventilated NPIW during glacial. Taken together, these observations affirm the deep North Pacific as a substantial carbon reservoir via deep water circulation and upwelling during deglacial and interglacial periods. Lastly, I introduce a new integrated approach of using machine learning (ML) to quantify and predict geochemical data in sediments from XRF spectra. By using this approach, the reconstruction of the NW Pacific carbonate deposition patterns in future studies could be built on high-resolution quantitative data, without losing accuracy due to extensive laboratory work or machine bias.

## **Kurzfassung**

Der Nordpazifik ist im Hinblick auf paläozeanographische Veränderungen und seinen Einfluss auf das globale Klima im Vergleich zu den anderen Ozeanen bisher nur unzureichend erforscht. Insbesondere die heutige Rolle des tiefen Nordpazifiks als  $\text{CO}_2$ -Senke, dessen Produktivitätsregime und Karbonatsystem, sowie der Zusammenhang dieser Prozesse mit dem marinen Kohlenstoffkreislauf sind aufgrund des Mangels an verfügbaren Proxies und Zeitserien aus dieser Region bislang nur unzureichend erforscht. Diese Arbeit zielt darauf ab, das Verständnis der Rolle des Nordpazifischen Tiefenwassers (NPDW) in der Meridionalen Umwälzzirkulation, deren spezifische Empfindlichkeit und Reaktion auf Rückkopplungsmechanismen zwischen tiefem und intermediärem Ozean, sowie der Atmosphäre zu verbessern. Hierzu wurde eine neue Serie von Sedimentkernen genutzt und geochemische Daten von einem meridionalen Profilschnitt entlang der Emperor Seamount Kette und am Hess Rise im Nordwestpazifik erstellt. In dieser Arbeit wurde zudem ein auf Röntgenfluoreszenz (XRF)-Scanning basierendes chemostratigraphisches, und durch Sauerstoffisotopen-Stratigraphie abgesichertes, Altersmodell für die Sedimentkerne in dieser Region entwickelt.

Die gewonnenen Rekonstruktionen der letzten 550.000 Jahre im Nordpazifik zu Variationen der Paläoproduktivität und des Karbonatkreislaufes in der Tiefsee, sowie die Dynamik der Wassermassen im Zusammenhang mit dem marinen Kohlenstoffkreislauf, werden in zwei Manuskripten vorgestellt. Die aus XRF-Daten rekonstruierte biologische Produktivität zeigt südlich von  $40^\circ\text{N}$  einen Rückgang der Karbonatablagerungen sowie ein phasenverschobenes

Muster nach Süden hin während der letzten 500.000 Jahre vor heute im NW Pazifik. Dies bestä'tigt die initiale Hypothese, dass regionale Verschiebungen in der subpolaren und subtropischen Wirbelzirkulation und der Schichtung des oberen Ozeans maßgeblich die Nährstoffverteilung in dieser Region definiert. Andererseits deuteten die kohärenten interglazialen Anstiege von biogenem Barium, Karbonatfluss, Alkenonkonzentration, Sandanteil und Opalgehalt darauf hin, dass die Produktivität in der subpolaren Region einen direkteren Einfluss auf das Karbonatsystem hatte und zur Ablagerungsdynamik entscheidend beitrug. Die geringe Korrelation zwischen der Karbonaterhaltung und der Produktivität auf dem Hess Rücken passt jedoch zu Schwankungen der Karbonatchemie im tiefen Pazifik, die wiederum mit überwiegender Karbonatauflösung zusammenhängen. Diese Diskrepanz deutet auch darauf hin, dass sich die ozeanographischen Fronten, die den subpolaren und subtropischen Wirbel verschieben, den NW-Pazifik mit unterschiedlichen Nährstoffen versorgen. Darüber hinaus wurden um den Ablauf der Ventilation im tiefen Nordpazifik zu rekonstruieren, die monospezifischen stabilen Isotopendaten einer epibenthischen Foraminifere (*Cibicidoides wuellerstorfi*), die Charakteristika des NPDW abbildet, mit flacheren nordpazifischen sowie tieferen südpazifischen Ursprungswassermassen verglichen. Meine Ergebnisse belegen eine glaziale Stagnation des NPDW während der letzten vier Glazial-Interglazial-Zyklen. Die Kohlenstoffisotopen ( $\delta^{13}\text{C}$ ) – Gradienten zwischen NPDW und zirkumpolarem Tiefenwasser ( $\Delta\delta^{13}\text{C}$ ) deutet auf einen relativ konstanten Beitrag südlicher abyssaler Wassermassen zur Bildung von NPDW hin, aber auch auf eine langfristige Veränderung der Einströmungsstärke in den Nordpazifik. Während der Zeiträume der glazialen Terminationen II bis V wurde aus dem abrupten Wegfallen des  $\Delta\delta^{18}\text{O}$ -Gradienten zwischen dem NPDW und dem Nordpazifischen Zwischenwasser (NPIW) auf einen Zusammenbruch der Schichtung im NW-Pazifik geschlossen, wohingegen sich die Ventilation im  $\Delta\delta^{13}\text{C}$  nicht ebenso eindeutig veränderte. Die  $\Delta\delta^{13}\text{C}$ -Signale zeigen jedoch, dass während der Marinen Isotopen Stadien (MIS) 10 bis 13 eine rasche Veränderung der Ventilationscharakteristik von einem stark ventilierten NPDW während des Interglazials zu einem besser durchlüftetem NPIW während des Glazials stattfindet. Diese Beobachtungen bestätigen Annahmen, nach denen der tiefe Nordpazifik während der vergangenen Kaltzeiten als signifikantes Kohlenstoffreservoir diente und damit auch eine potentielle Quelle für  $\text{CO}_2$ -Emission in die Atmosphäre über die Tiefenwasserzirkulation während der Deglaziale und Interglaziale repräsentierte. Die genauere Erfassung und Rekonstruktion der Größe und Eigenschaften dieses Kohlenstoffspeichers und eine detaillierte Untersuchung der Funktionsweise des Karbonatkreislaufs wären ein sinnvoller nächster Schritt. Zu diesem Zweck wird im dritten



Manuskript ein neuer integrierter Ansatz des maschinellen Lernens (ML) zur Quantifizierung und Vorhersage geochemischer Daten in Sedimenten aus XRF-Spektren vorgestellt. Mit Hilfe dieses Ansatzes könnte die quantitative Rekonstruktion der Karbonatablagerungen im Nordwestpazifik in vergleichbaren zukünftigen Studien auf hochauflösenden quantitativen Daten aufbauen, ohne dass die Genauigkeit aufgrund umfangreicher Laborarbeiten oder maschineller Einflüsse verloren ginge.

# Table of Contents

<i>Acknowledgements</i> .....	<i>iv</i>
<i>Abstract</i> .....	<i>vi</i>
<b>1. Introduction and Objective</b> .....	<b>1</b>
1.1. Motivation .....	1
1.2. Aims of the Thesis .....	2
1.3. Background and Previous Studies .....	3
1.3.1. The Modern Northwest Pacific Oceanographic Conditions .....	3
1.3.2. Previous North Pacific Paleoceanographic Studies .....	7
1.4. Thesis Structure .....	8
1.5. Thesis declaration of author's contribution .....	9
1.6. References .....	11
<b>2. Material and Methods</b> .....	<b>14</b>
2.1. Sample Material and Selection .....	14
2.2. Methods .....	15
2.2.1. X-ray Fluorescence Scanning .....	15
2.2.2. Sediment Preparation and Properties .....	16
2.2.3. CaCO <sub>3</sub> and TOC Measurements .....	16
2.2.4. Stable Isotope Measurements .....	17
2.2.5. AMS <sup>14</sup> C Measurements .....	18
2.3. Reference .....	18
<b>3. Age Model Approach for the Emperor Seamount Chain Region</b> .....	<b>19</b>
3.1. Reference .....	22
<b>4. Glacial-interglacial variations of productivity and carbonate deposition in the Northwest Pacific during the last 500,000 years</b> .....	<b>23</b>
4.1. Introduction .....	24
4.2. Study area and oceanographic setting .....	26
4.3. Material and Methods .....	29

4.3.1.	X-ray fluorescence (XRF) core scanning .....	30
4.3.2.	Bulk sample processing and physical properties.....	30
4.3.3.	Coarse fraction processing and stable isotopes measurements.....	31
4.3.4.	AMS <sup>14</sup> C ages .....	32
4.3.5.	Alkenone content.....	32
<b>4.4.</b>	<b>Age model.....</b>	<b>32</b>
<b>4.5.</b>	<b>Results and discussion.....</b>	<b>36</b>
4.5.1.	NW Pacific glacial-interglacial productivity variations and their forcing factors over the last 500 ka	36
4.5.2.	NW Pacific variations in carbonate production and preservation .....	41
<b>4.6.</b>	<b>Conclusions .....</b>	<b>49</b>
<b>4.7.</b>	<b>Authors' contributions .....</b>	<b>49</b>
<b>4.8.</b>	<b>Acknowledgements.....</b>	<b>50</b>
<b>4.9.</b>	<b>Data Availability.....</b>	<b>50</b>
<b>4.10.</b>	<b>References .....</b>	<b>50</b>
<b>4.11.</b>	<b>Supplementary.....</b>	<b>57</b>
<b>5.</b>	<b><i>Variations in North Pacific Deep Water characteristics and ventilation patterns over the past 540,000 years.....</i></b>	<b>60</b>
<b>5.1.</b>	<b>Introduction .....</b>	<b>61</b>
<b>5.2.</b>	<b>Material and Methods.....</b>	<b>63</b>
5.2.1.	Sample material and stable isotopes .....	63
5.2.2.	Age model .....	64
<b>5.3.</b>	<b>Results and Discussion .....</b>	<b>64</b>
5.3.1.	CDW characteristics in NW Pacific .....	66
5.3.2.	NPIW influence on NW Pacific .....	69
<b>5.4.</b>	<b>Conclusions .....</b>	<b>72</b>
<b>5.5.</b>	<b>Data Availability.....</b>	<b>73</b>
<b>5.6.</b>	<b>References .....</b>	<b>73</b>
<b>5.7.</b>	<b>Supplementary.....</b>	<b>76</b>

<b>6.</b>	<b><i>Quantifying calcium carbonate and organic carbon content in marine sediments from XRF-scanning spectra with a machine learning approach</i></b>	<b>78</b>
6.1.	Introduction	79
6.2.	Machine Learning: approach and set-up	83
6.2.1.	Pilot test	83
6.2.2.	Model training and evaluation	84
6.3.	Results: Optimization of machine-learning models, evaluations of test set and case study, quantification of CaCO <sub>3</sub> and TOC	85
6.4.	Discussion: Applications in case study and whole dataset, limitations, strengths	88
6.5.	Guidelines for future applications	91
6.6.	Conclusions	92
6.7.	Materials and methods	92
6.7.1.	Sediment cores and bulk measurements	92
6.7.2.	Setting of the Avaatech XRF scanning and data compilation	93
6.7.3.	Use of machine learning programming	94
6.8.	Data availability	94
6.9.	References	94
6.10.	Acknowledgments	97
6.11.	Author contributions	98
6.12.	Supplementary	98
6.12.1.	Detailed grid search results	98
6.12.2.	Evaluation in case study	102
6.12.3.	Info and exported data	102
<b>7.</b>	<b><i>Synthesis and Outlook</i></b>	<b>106</b>
7.1.	Synthesis	106
1.1.	Outlook	108
7.1.1.	High Resolution Reconstruction of Calcium Carbonate Preservation in Northwest Pacific	108
7.1.2.	Ventilation Age Changes in the Northwest Pacific	110
7.2.	References	111
	<b><i>Data Availability of this thesis</i></b>	<b>113</b>

**Appendix ..... 113**

**i. Additional Manuscript Related to The Thesis .....113**

**Appendix 1: Cores and measurements done in this thesis .....115**

# 1. Introduction and Objective

## 1.1. Motivation

Anthropogenic carbon dioxide ( $\text{CO}_2$ ), which accounts for a large part of the anthropogenic emission since the industrial revolution, has raised dramatically and is estimated to increase further throughout the next century. The  $\text{CO}_2$  level has been changing on the thousand-year timescale of glacial/interglacial. To equilibrate the  $\text{CO}_2$  changes, the ocean is found as the largest reservoir of  $\text{CO}_2$  and in particular, the gas exchange between atmosphere and ocean plays an important role in this process. In order to have a better understanding of what the future climate might hold, reconstruction of the past climate and investigation of the ocean contributions associated with the  $\text{CO}_2$  level would be beneficial to the climate projection.

The subarctic oceanic regions contribute significantly to the stability of the global carbon cycle due to their large storage capacity. The Pacific Ocean is the largest body of water on Earth and its deep compartment hosts the oldest water masses. Today, the North Pacific is considered an important region in the oceanic carbon cycle and global climate not only due to its vast size, but also its high, but inefficient biological export production and potential for carbon storage. Apart from this, being the terminus of the Meridional Overturning Circulation (MOC, Figure 1.1) where old, nutrient- and carbon-rich waters accumulate, the North Pacific has been assumed to turn into a potential source of  $\text{CO}_2$  to the atmosphere, thereby contributing to deglacial  $\text{CO}_2$  rise during the past climate transitions. The sea-air gas exchange is regulated by biological and solubility (physical and alkalinity) pumps. The biological pump is driven by photo-autotrophic phytoplankton growth, by which surface organisms fix inorganic carbon into organic matter and sinks to the ocean interior in the form of calcium carbonate ( $\text{CaCO}_3$ ) as export production. On the other hand, the solubility pump is known to be more efficient in the polar regions because cold water can dissolve more gas e.g.,  $\text{CO}_2$ , and denser than warm water so that it sinks and brings carbon into the deep ocean. As a result, both increased export production and reduced exposure of deep water to the atmosphere would contribute to  $\text{CO}_2$  sequestration. Over the course of many years of research, we have a relatively clear grasp of these processes in in the subarctic Atlantic in relation to North Atlantic Deep Water (NADW) formation, its ventilation and its export into other oceanic regions. However, we have only a limited understanding of past climate dynamics and paleoceanography of the subarctic North Pacific, particularly regarding the efficiency and sensitivity of the biological and solubility

pumps which regulate the sea-air exchange. In addition to this, the availability of signal carriers, especially foraminifera and coccolithophores, for proxy reconstructions is hampered by the shallow lysocline and carbonate-corrosive water in the North Pacific.

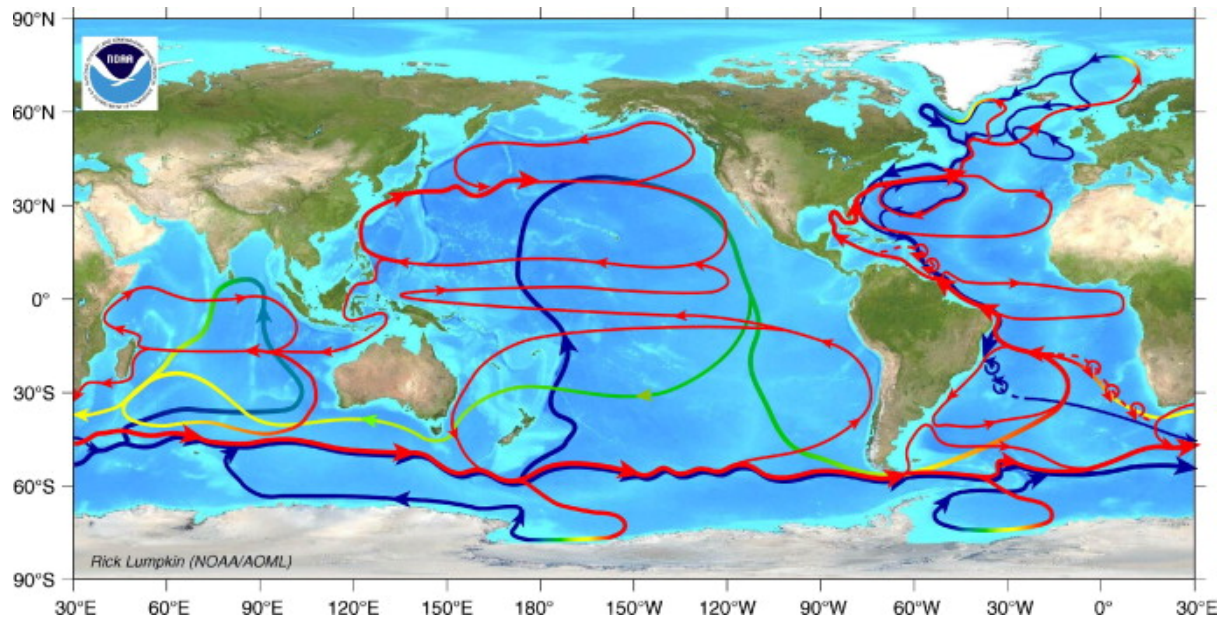


Figure 1.1. Schematic pathways of the global Meridional Overturning Circulation (MOC) and selected recirculation patterns (by Rick Lumpkin, figure from Richardson, 2008) Red: light, upper water, blue: bottom and deep water.

To address these issues in the subpolar Northwest Pacific expedition SO264 was carried out in summer 2018, leading to the collection of sediment cores retrieved along the Emperor Seamount Chain in the Northwest (NW) Pacific. This thesis is principally based on using material from SO264 to improve on present deficits in knowledge and provide new information about the NW Pacific paleoceanography and its closely linked deep water ventilation and circulation changes.

## 1.2. Aims of the Thesis

In order to improve the knowledge of the role of North Pacific in the marine carbon cycle and the particular features of the NW Pacific compared to the rest of the basin, a new set of sediment cores were retrieved along the Emperor Seamount Chain. This thesis aims to reconstruct the paleoceanographic history of deep NW Pacific water masses, their relation to carbonate deposition patterns, and connections to the regional productivity regimes by examining a new compilation of cores and data. Due to the lack of available data and poor preservation in the North Pacific sediments, the carbonate chemistry, productivity changes and the water masses

ventilation history are not well-studied, except for few, but short sediment records that rarely extend beyond the last glacial (Keigwin et al., 1992; Keigwin, 1998; Matsumoto et al., 2002).

Based on a selection of sediment cores, I address the following topics and seek to answer the following questions in this thesis:

- What is the influence of North Pacific marine productivity on the carbonate system and the oceanic carbon storage potential on glacial-interglacial time scales?
- How do the North Pacific subarctic and subtropical gyre regions differ in their productivity and carbonate deposition patterns? What are major causes for different?
- Does the North Pacific feature a singular, coherent domain in its productivity and carbonate deposition regime?
- How sensitive and different was the NPDW ventilation in the past and during warmer-than-present climate stages?
- How much did the physical and chemical mid-depth to deep water stratification in the North Pacific change on orbital time scales?
- Did the source water mass contributions to NPDW from deep southern and shallow northern sources change on orbital time scales?

In this thesis, I examine productivity, carbonate preservation and benthic foraminiferal stable isotopes along a meridional transect crossing the subarctic and subtropical gyre regions, with a view on improving the understanding of the NPDW ventilation and circulation history over the last five glacial-interglacial cycles. Following this, I introduce an integrated method with machine learning (ML) to quantify X-ray fluorescence (XRF) spectra data focusing on calcium carbonate. In order to investigate the spatial and temporal distribution of carbonate deposition in the NW Pacific associated with the biological pump and carbon cycle, this method would be very helpful in producing good amount of data without losing accuracy and bring extra measurement time.

### **1.3. Background and Previous Studies**

#### **1.3.1. The Modern Northwest Pacific Oceanographic Conditions**

The major surface feature of the modern NW Pacific and its marginal seas is the counterclockwise Western Subarctic Gyre, which is divided by several wind-driven circulation cells (Figure 1.2). These surface waters transport heat and nutrients between different ocean



regions. Warm equatorial Pacific waters are transported via the Kuroshio Current and flow into the North Pacific along the east coast of Japan. The western boundary of the Kuroshio Current, Kuroshio Extension, flows eastward into the North Pacific until it splits up into the Northeast Pacific as the southern California Current and the northern Alaska Gyre. From the North American west coast, surface waters are then back westward into the Alaskan Stream. Part of these waters enter into the Bering Sea and the rest continues along the east coast of Kamchatka as East Kamchatka Current. A part of these waters enters the Okhotsk Sea and upon export from that basin modify into the Oyashio Current. The Oyashio Current then transports cold, subarctic, nutrient-rich waters southward until it reaches the Kuroshio Current. Their deflection point defines the North Pacific Subarctic Front, Subarctic Boundary and Subtropical Front.

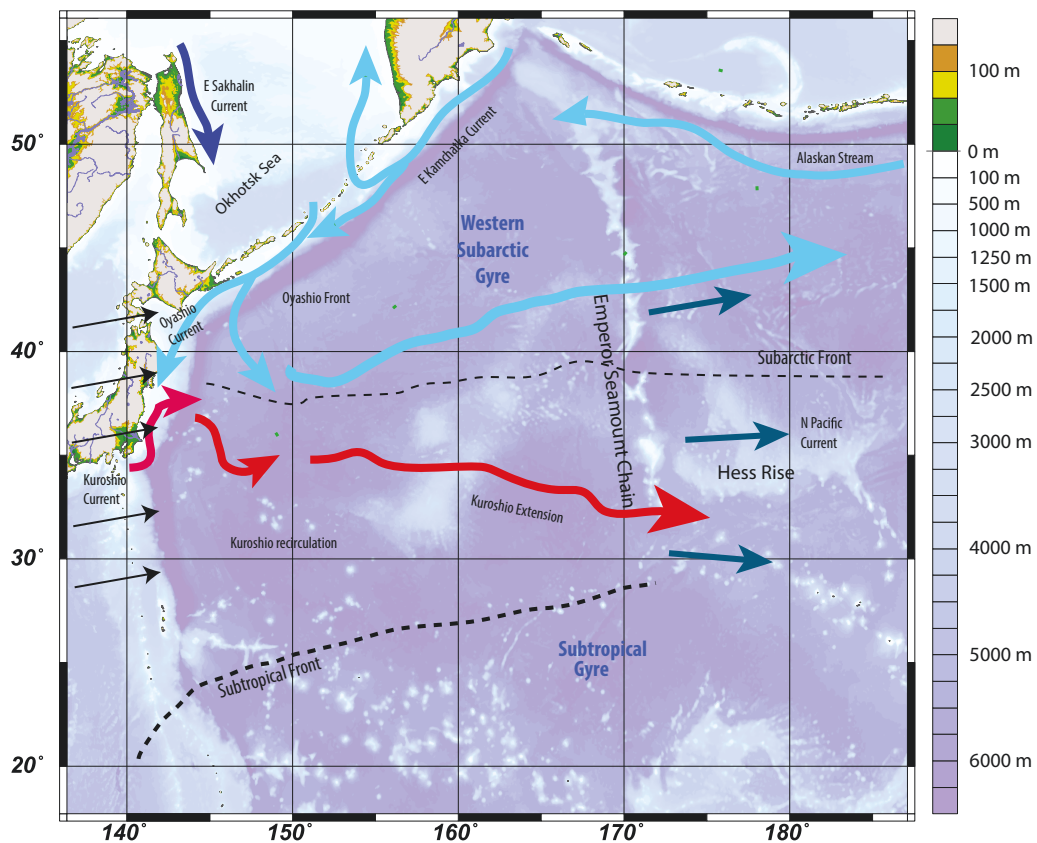


Figure 1.2. Map of North Pacific study area, with schematic representation of major fronts, current systems, topographic and bathymetric features (modified after Nürnberg, 2018b).

The intermediate depths in the NW Pacific are occupied by North Pacific Intermediate Water (NPIW), consisting of major precursor components from the Okhotsk Sea mixed with the surface waters from the Western Subarctic Gyre and Kuroshio Waters (Shcherbina et al., 2003; Talley, 1993). Below 2000 m depth, the North Pacific Deep Water (NPDW) is the dominant water mass, sourced by abyssal and bathyal water masses from the Southern Ocean (Figure

1.3). These are Circumpolar Deep Water (CDW), consisting of Upper Circumpolar Deep Water (UCDW) and Lower Circumpolar Deep Water (LCDW), formed in the Southern Ocean and entering through the Southwest Pacific east of the New Zealand Plateau and Chatman Rise. These waters finally reach the North Pacific, where they constitute, after the long circulation pathway and residence time in the deep ocean, the oldest, most nutrient- and carbon-rich, and oxygen-depleted water masses in the world ocean (see overview in Talley, 2013).. The carbonate-corrosive NPDW fill depths between 2000 to 4000 m in the North Pacific, resulting in a shallow position of the Carbonate Compensation Depth (CCD) at around 2500 m (Archer, 1996; Lyle, 2003). This condition limits the feasibility of obtaining sufficient calcareous materials for geochemical investigations and paleoclimatic reconstructions.

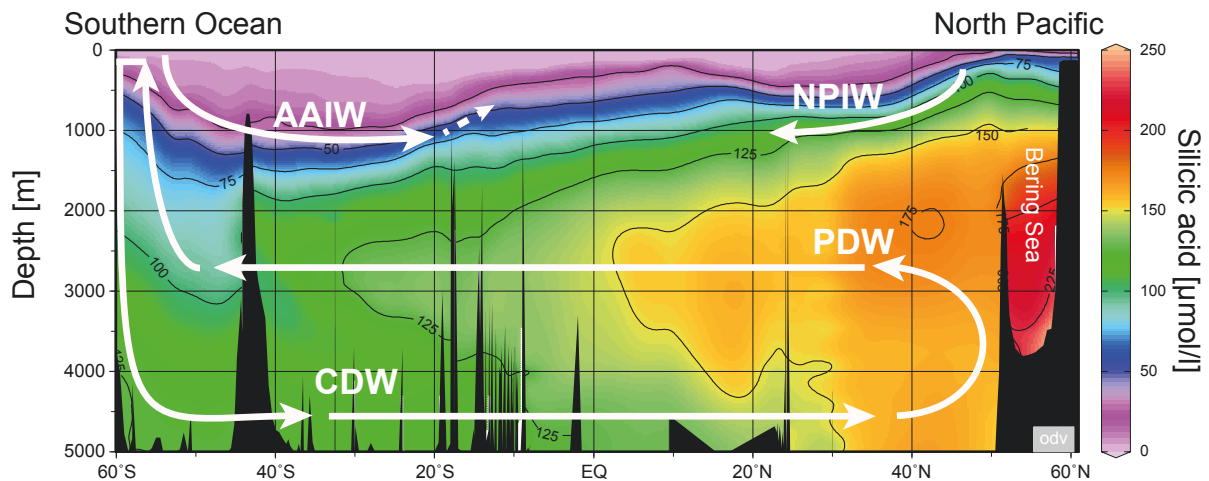


Figure 1.3. Meridional cross-section through Pacific, showing the major water masses based on their modern silicic acid content. Major water masses are noted in white, together with a schematic meridionally projected flow path. AAIW: Antarctic Intermediate Water, NPIW: North Pacific Intermediate Water, PDW: North Pacific Deep Water, CDW: Circumpolar Deep Water. Figure was created with Ocean Data View based on World Ocean Atlas Data (modified after Max et al., 2017).

In contrast to the North Atlantic, due to a significantly low-salinity gradient (halocline) which prevents the surface water sinks into great depth, no deep water forms in the North Pacific. This steep halocline also largely inhibits the mixing of surface water with the underlying nutrient-rich deep water (Haug et al., 1999; Warren, 1983). In addition, the Subarctic Pacific Gyre is isolated by the wind stress pattern and circulation systems from the warmer, but nutrient-depleted subtropical gyre (e.g., Harrison et al., 2004; Yasuda, 2003). Therefore, the water mixing is mostly restricted to the upper to mid-depth at about 200 m to 800 m, due to turbulent mixing by tides, gyres and severe, frequent winter storms (Talley, 1993), which nonetheless result in upwelling of high amounts of nutrients into the upper ocean. The productivity in the North Pacific is relatively inefficient regarding the use of major nutrients, resulting in unused major nutrients remaining in the upper water layer, similar to the Southern

Ocean and the Equatorial Pacific (Figure 1.4). Hence, the subarctic North Pacific is characterized as a high-nutrient, low-chlorophyll zone (HNLC).

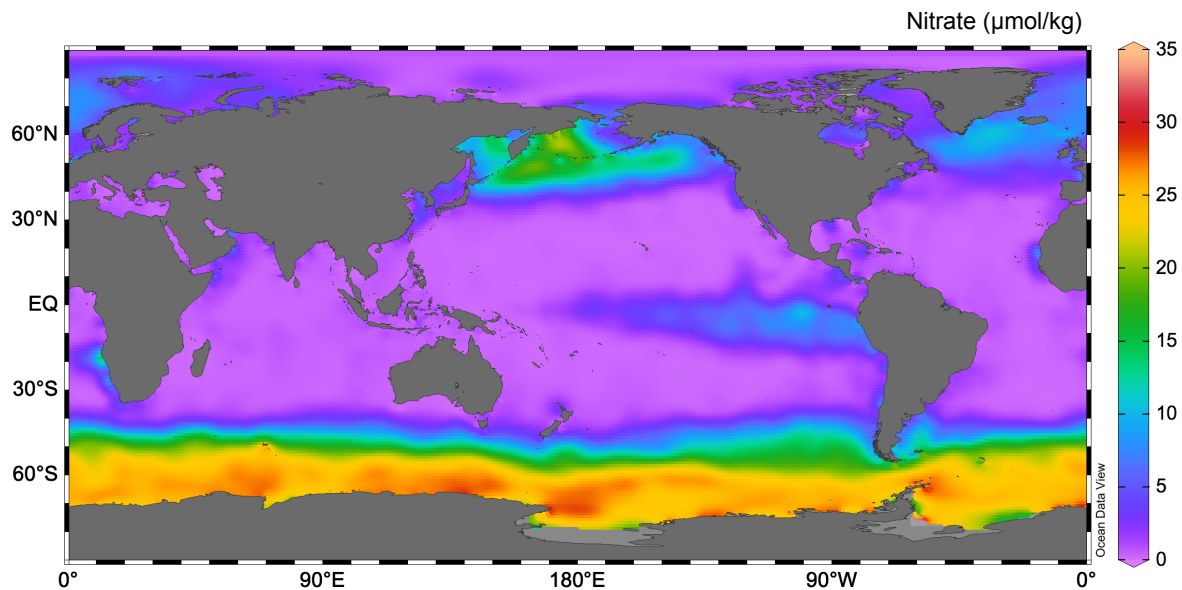


Figure 2.4. Modern global annual surface ocean nitrate concentration. Map is created with Ocean Data View and dataset from World Ocean Atlas 2018 (<https://odv.awi.de/data/ocean/world-ocean-atlas-2018/>).

Similar to the Southern Ocean, the biological pump in the Subarctic Pacific is not fast enough in fixing  $\text{CO}_2$  into organic matter in comparison to the release of previously sequestered  $\text{CO}_2$  from the deep ocean via vertical exchange of water masses in the modern conditions. The unused, or so-called “preformed”, nutrients have missed the chance to sequester  $\text{CO}_2$  into the deep ocean. The  $\text{CO}_2$  contribution is determined by the vertical upwelling or horizontal mixing (physical), as well as nutrients utilization or burial efficiency of organic carbon (biological). Furthermore, the deep ocean regulates the exchange of carbon between the geological reservoir and the hydrosphere or atmosphere system through its control of the carbonate cycle, burial and dissolution of  $\text{CaCO}_3$  on the seafloor (Sigman and Boyle, 2000). The high marine productivity of the modern subarctic Pacific thus constitutes a sink of  $\text{CO}_2$  from the atmosphere to the ocean (Honda et al., 2002; Takahashi et al., 2002). Therefore, it is reasonable to assume, any changes in the relation between the paleo-productivity and carbonate deposition, or deep water ventilation in the NW Pacific would provide details about the complex causes for the atmospheric  $\text{CO}_2$  variations.

### 1.3.2. Previous North Pacific Paleoceanographic Studies

Previous studies have shown that a close interconnection exists between the North Pacific paleoceanographic variations both in upper and deep ocean compartments, and global climate change over the middle to late Pleistocene (e.g., Galbraith et al., 2008; Jaccard et al., 2010; Jacobel et al., 2017; Mix et al., 1991). Based on different proxies, records and observations, the biological production in the North Pacific is thought to have been generally lower during cold intervals, even though an increased dust flux supplied higher amounts of Iron and other micronutrients to foster phytoplankton growth (e.g., Brunelle et al., 2007; Gebhardt et al., 2008; Kienast et al., 2004; Narita et al., 2002; Shigemitsu et al., 2007). Under this scenario, an assumption could be made that the underlying nutrient supply via physical convection was limited and reduced during cold stages. Studies from marginal seas also provided evidence that an enhanced stratification limited the nutrient supply to the surface and led to a more complete nutrient utilization in combination with aeolian iron supply during glacials (e.g., Brunelle et al., 2007; Brunelle et al., 2010; Riethdorf et al., 2016). However, upon closer inspection the North Pacific biogenic export production on a basin-wide scale is rather heterogeneous than commonly thought (e.g., Kohfeld and Chase, 2011). Moreover, due to the shallow CCD, the scarce coverage of carbonate-bearing records leads to an incomplete knowledge of Pacific carbonate chemistry. A limited number of studies, using records from the lower latitude Equatorial and East Pacific, showed higher  $\text{CaCO}_3$  contents during glacial and lower content during interglacial, which provided the baseline for a consensus of an anti-correlation between Atlantic and Pacific  $\text{CaCO}_3$  preservation patterns on orbital time scales for the past ca. 500,000 years before present (ka BP, Sexton and Barker, 2006). The controlling factors of this  $\text{CaCO}_3$  preservation pattern could be attributable to various reasons, such as carbonate production from surface waters, dilution by non-carbonate materials (e.g., opal), or dissolution driven by changes in carbonate ion concentration  $[\text{CO}_3^{2-}]$  of deep-water masses. The causes of these opposed  $\text{CaCO}_3$  cycles have been discussed controversially (e.g., Anderson et al., 2008; Archer and Maier-Reimer, 1994; Farrell and Prell, 1989; Hodell et al., 2001; Sexton and Barker, 2012; Zhang et al., 2007). Yet the subarctic Pacific records showed a perplexing pattern with  $\text{CaCO}_3$  content interglacial maxima otherwise carbonate-free sediments, indicating a different nutrient or geochemical regime occurred in the region (Brunelle et al., 2010; Iwasaki et al., 2012; Jaccard et al., 2010).

On the other hand, there is growing evidence indicating large-scale reorganization of North Pacific deep and intermediate waters occurred on geological time scales, especially during the last deglaciations. Marchitto et al. (2007) provided evidence from the NE Pacific showing that an “old” carbon-rich waters were injected into intermediate waters. Lund et al. (2011) found decreased ventilation in the deeper ocean evidenced by radiocarbon dating on benthic-planktic (B-P) foraminifera, but they concluded that this deep water was not old enough to be the source of shallower “old” carbon-rich water. Evidence from the deep Gulf of Alaska (3647 m water depth), showing dramatic transient increases in carbonate preservation and biogenic fluxes were used to postulate deglacial outgassing of CO<sub>2</sub> from the subpolar North Pacific (Galbraith et al., 2007). Contrary observations from NE Pacific indicated the onset of deep water formation in a record from 3640 m water depth (Rae et al., 2014). In line with these hypotheses, Okazaki et al. (2010) argued that formation of NPDW occurred in the North Pacific down to depths of 2500 to 3000 m. Jaccard and Galbraith (2013) contradicted this hypothesized enhanced ventilation in the NW Pacific during the early deglaciation based on authigenic uranium concentration from 2392 m water depth. Records from the Bering Sea and Okhotsk Sea revealed enhanced ventilation being restricted to the intermediate water layer and provided possible sources of enhanced deglacial NPIW formation (Max et al., 2014a). These results were supported by subsequent modeling simulations (Gong et al., 2019); supporting the notion that this increased ventilation was likely limited to intermediate water depths.

Overall, the ventilation and oceanographical history in the North Pacific remains controversial, including potential asymmetries between the western and eastern parts of the ocean. In addition, existing records are mostly restricted to marginal areas and much of the bathyal to abyssal area in the western basin remains unexplored. Hence, investigations of the deep Pacific are essential in order to reach a more complete knowledge of the role of deep water masses, their origins, configurations and geochemical signatures in the Pacific, to better understand their contributions to the marine carbon cycle.

#### **1.4. Thesis Structure**

In the following Chapter 2, the material and methods used in this thesis are described in detail. Chapter 3 presents the XRF-based age model approach for the studied region to obtain a stratigraphic framework for cores.

Chapter 4 (manuscript 1) describes the relationship between biological export production, deep sea carbonate deposition, and the dynamic changes on orbital timescales along meridional transects in the NW Pacific. This manuscript provides evidence of rapid change of productivity and carbonate cycle between the subpolar and subtropical NW Pacific for the last 500,000 years.

Chapter 5 (manuscript 2) presents a new monospecific benthic foraminiferal *Cibicides wuellerstorfi* stable isotope record from the bathyal North Pacific, which reflects the deep water ventilation signal. A comparison of oxygen and carbon isotopes differences between NPDW and its potential source water masses from the North and South is provided for the last 550,000 years.

Chapter 6 (manuscript 3) introduces a new integrated method of a machine-learning approach to use XRF-scanning-derived spectra to quantify calcium carbonate content (CaCO<sub>3</sub> wt%) on a regional to basin-wide scale. This approach will be beneficial to further studies to obtain high-resolution data, while reducing the need for discrete measurements.

Chapter 7 summarizes the conclusions of this thesis. As an outlook to future works beyond this thesis, brief outlines for two potential manuscripts are provided in this chapter.

In the Appendix, one project-related manuscript is included, presenting past NW Pacific Sea surface and sub-surface temperature changes, which inferred shifts of the Subarctic Front and the dynamics of ENSO changes. A detailed table, listing cores which have been sampled and measurements carried out during this PhD thesis, is also included in the appendix. Relevant references are listed at the end of each chapter.

## **1.5. Thesis declaration of author's contribution**

The results thesis is constituted of three joint-authorship manuscripts that is published, have been submitted or will be submitted to scientific journals. **Me** and the co-authors' contributions to each manuscript are outlined as follows:

**Paper I: Glacial-interglacial variations in productivity and carbonate deposition in the Northwest Pacific during the last 500,000 years**

Authors: **Weng-Si Chao**, Lara Jacobi, Bryan Niederbockstruck, Dirk Nürnberg, Linda Langemann, Gerhard Kuhn, Natalja Bubenchshikova, Jian-Jun Zou, Xue-Fa Shi, Ralf Tiedemann, Lester Lembke-Jene

Publication state: This manuscript is in internal revision and to be submitted to the Journal *Frontiers in Earth Science*.

WSC, LLJ and RT designed study. WSC and LJ carried out XRF-scanning. WSC, BN and LLJ measured stable isotopes. WSC, LJ, LLJ, RT, DN developed age model. WSC, BN and LL analyzed the data. WSC and LLJ wrote the paper, with input from all co-authors. All authors discussed the data and contributed to the final manuscript version.

### **Paper II: Variations in North Pacific Deep Water characteristics and ventilation patterns over the past 540,000 years**

Authors: **Weng-Si Chao**, Ralf Tiedemann, Lester Lembke-Jene

Publication state: This manuscript is in preparation and to be submitted to the Journal *Climate of the Past*.

WSC, LLJ and RT designed study. WSC analyzed the data. WSC and LLJ wrote the paper, with input from all co-authors. All authors discussed the data and contributed to the final manuscript version.

### **Paper III: Quantifying calcium carbonate and organic carbon content in marine sediments from XRF-scanning spectra with a machine learning approach**

Authors: An-Sheng Lee and **Weng-Si Chao**, Sofia Ya Hsuan Liou, Ralf Tiedemann, Bernd Zolitschka, Lester Lembke-Jene

Publication state: This manuscript has been published on the Journal *Scientific Reports*.

ASL and WSC: Conceptualization, Methodology, Investigation, Data curation, Writing – original draft.

RT, LLJ, BZ, and SYHL.: Supervision, Writing – review and editing, Resources, Funding acquisition.

### **Additional paper: ENSO vs glacial-interglacial-induced changes in the Kuroshio-Oyashio transition zone during the Pleistocene**

Authors: Lara Jacobi, Dirk Nürnberg, **Weng-Si Chao**, Lester Lembke- Jene, Ralf Tiedemann  
Publication state: This manuscript has been submitted to the Journal *Frontiers in Marine Science* and is in review.

LJ, **WSC**, DN and LLJ collected the samples at sea. LJ and **WSC** proceeded the XRF scanning. LJ prepared and measured the foraminiferal samples with support from DN's working group. LJ and DN developed the age model and analyzed the data. LJ made all figures and wrote the manuscript, **WSC**, DN and LLJ contributed with ideas and feedback throughout the whole process of designing the study and writing the manuscript. All authors discussed the final manuscript and approved the submitted version.

## 1.6. References

- Anderson, R., Fleisher, M., Lao, Y. and Winckler, G., 2008. Modern CaCO<sub>3</sub> preservation in equatorial Pacific sediments in the context of late-Pleistocene glacial cycles. *Marine Chemistry*, 111(1-2): 30-46.
- Archer, D., 1996. A data-driven model of the global calcite lysocline. *Global Biogeochemical Cycles*, 10(3): 511-526.
- Archer, D. and Maier-Reimer, E., 1994. Effect of deep-sea sedimentary calcite preservation on atmospheric CO<sub>2</sub> concentration. *Nature*, 367(6460): 260-263.
- Brunelle, B.G., Sigman, D.M., Cook, M.S., Keigwin, L.D., Haug, G.H., Plessen, B., Schettler, G. and Jaccard, S.L., 2007. Evidence from diatom-bound nitrogen isotopes for subarctic Pacific stratification during the last ice age and a link to North Pacific denitrification changes. *Paleoceanography*, 22(1).
- Brunelle, B.G., Sigman, D.M., Jaccard, S.L., Keigwin, L.D., Plessen, B., Schettler, G., Cook, M.S. and Haug, G.H., 2010. Glacial/interglacial changes in nutrient supply and stratification in the western subarctic North Pacific since the penultimate glacial maximum. *Quaternary Science Reviews*, 29(19-20): 2579-2590.
- Farrell, J.W. and Prell, W.L., 1989. Climatic change and CaCO<sub>3</sub> preservation: An 800,000 year bathymetric reconstruction from the central equatorial Pacific Ocean. *Paleoceanography*, 4(4): 447-466.
- Galbraith, E.D., Jaccard, S.L., Pedersen, T.F., Sigman, D.M., Haug, G.H., Cook, M., Southon, J.R. and Francois, R., 2007. Carbon dioxide release from the North Pacific abyss during the last deglaciation. *Nature*, 449(7164): 890-893.
- Galbraith, E.D., Kienast, M., Jaccard, S.L., Pedersen, T.F., Brunelle, B.G., Sigman, D.M. and Kiefer, T., 2008. Consistent relationship between global climate and surface nitrate utilization in the western subarctic Pacific throughout the last 500 ka. *Paleoceanography*, 23(2).
- Gebhardt, H., Sarnthein, M., Grootes, P.M., Kiefer, T., Kuehn, H., Schmieder, F. and Röhl, U., 2008. Paleonutrient and productivity records from the subarctic North Pacific for Pleistocene glacial terminations I to V. *Paleoceanography*, 23(4).
- Gong, X., Lembke-Jene, L., Lohmann, G., Knorr, G., Tiedemann, R., Zou, J. and Shi, X., 2019. Enhanced North Pacific deep-ocean stratification by stronger intermediate water formation during Heinrich Stadial 1. *Nature communications*, 10(1): 1-8.



- Harrison, P.J., Whitney, F.A., Tsuda, A., Saito, H. and Tadokoro, K., 2004. Nutrient and plankton dynamics in the NE and NW gyres of the subarctic Pacific Ocean. *Journal of Oceanography*, 60(1): 93-117.
- Haug, G.H., Sigman, D.M., Tiedemann, R., Pedersen, T.F. and Sarnthein, M., 1999. Onset of permanent stratification in the subarctic Pacific Ocean. *Nature*, 401(6755): 779-782.
- Hodell, D., Charles, C. and Sierro, F., 2001. Late Pleistocene evolution of the ocean's carbonate system. *Earth and Planetary Science Letters*, 192(2): 109-124.
- Honda, M.C., Imai, K., Nojiri, Y., Hoshi, F., Sugawara, T. and Kusakabe, M., 2002. The biological pump in the northwestern North Pacific based on fluxes and major components of particulate matter obtained by sediment-trap experiments (1997–2000). *Deep Sea Research Part II: Topical Studies in Oceanography*, 49(24-25): 5595-5625.
- Iwasaki, S., Takahashi, K., Maesawa, T., Sakamoto, T., Sakai, S. and Iijima, K., 2012. Paleoceanography of the last 500 kyrs in the central Okhotsk Sea based on geochemistry. *Deep Sea Research Part II: Topical Studies in Oceanography*, 61: 50-62.
- Jaccard, S., Galbraith, E., Sigman, D.M. and Haug, G., 2010. A pervasive link between Antarctic ice core and subarctic Pacific sediment records over the past 800 kyrs. *Quaternary Science Reviews*, 29(1-2): 206-212.
- Jaccard, S.L. and Galbraith, E.D., 2013. Direct ventilation of the North Pacific did not reach the deep ocean during the last deglaciation. *Geophysical Research Letters*, 40(1): 199-203.
- Jacobel, A., McManus, J., Anderson, R. and Winckler, G., 2017. Climate-related response of dust flux to the central equatorial Pacific over the past 150 kyr. *Earth and Planetary Science Letters*, 457: 160-172.
- Keigwin, L., Jones, G. and Froelich, P., 1992. A 15,000 year paleoenvironmental record from Meiji Seamount, far northwestern Pacific. *Earth and Planetary Science Letters*, 111(2-4): 425-440.
- Keigwin, L.D., 1998. Glacial-age hydrography of the far northwest Pacific Ocean. *Paleoceanography*, 13(4): 323-339.
- Kienast, S.S., Hendy, I.L., Crusius, J., Pedersen, T.F. and Calvert, S.E., 2004. Export production in the subarctic North Pacific over the last 800 kyrs: No evidence for iron fertilization? *Journal of Oceanography*, 60(1): 189-203.
- Kohfeld, K.E. and Chase, Z., 2011. Controls on deglacial changes in biogenic fluxes in the North Pacific Ocean. *Quaternary Science Reviews*, 30(23-24): 3350-3363.
- Lund, D.C., Mix, A.C. and Southon, J., 2011. Increased ventilation age of the deep northeast Pacific Ocean during the last deglaciation. *Nature Geoscience*, 4(11): 771-774.
- Lyle, M., 2003. Neogene carbonate burial in the Pacific Ocean. *Paleoceanography*, 18(3).
- Marchitto, T.M., Lehman, S.J., Ortiz, J.D., Flückiger, J. and van Geen, A., 2007. Marine radiocarbon evidence for the mechanism of deglacial atmospheric CO<sub>2</sub> rise. *science*, 316(5830): 1456-1459.
- Matsumoto, K., Oba, T., Lynch-Stieglitz, J. and Yamamoto, H., 2002. Interior hydrography and circulation of the glacial Pacific Ocean. *Quaternary Science Reviews*, 21(14-15): 1693-1704.
- Max, L., Belz, L., Tiedemann, R., Fahl, K., Nürnberg, D. and Riethdorf, J.-R., 2014. Rapid shifts in subarctic Pacific climate between 138 and 70 ka. *Geology*, 42(10): 899-902.
- Max, L., Rippert, N., Lembke-Jene, L., Mackensen, A., Nürnberg, D. and Tiedemann, R., 2017. Evidence for enhanced convection of North Pacific Intermediate Water to the low-latitude Pacific under glacial conditions. *Paleoceanography*, 32(1): 41-55.
- Mix, A., Pisias, N., Zahn, R., Rugh, W., Lopez, C. and Nelson, K., 1991. Carbon 13 in Pacific Deep and Intermediate Waters, 0-370 ka: Implications for ocean circulation and Pleistocene CO<sub>2</sub>. *Paleoceanography*, 6(2): 205-226.

- Narita, H., Sato, M., Tsunogai, S., Murayama, M., Ikehara, M., Nakatsuka, T., Wakatsuchi, M., Harada, N. and Ujiie, Y., 2002. Biogenic opal indicating less productive northwestern North Pacific during the glacial ages. *Geophysical Research Letters*, 29(15): 22-1-22-4.
- Nürnberg, D., 2018. RV SONNE Fahrtbericht / Cruise Report SO264 - SONNE-EMPEROR: The Plio/Pleistocene to Holocene development of the pelagic North Pacific from surface to depth – assessing its role for the global carbon budget and Earth's climate, Suva (Fiji) – Yokohama (Japan), 30.6. – 24.8.2018, GEOMAR Helmholtz-Zentrum für Ozeanforschung, Kiel, Germany.
- Okazaki, Y., Timmermann, A., Menviel, L., Harada, N., Abe-Ouchi, A., Chikamoto, M., Mouchet, A. and Asahi, H., 2010. Deepwater formation in the North Pacific during the last glacial termination. *Science*, 329(5988): 200-204.
- Rae, J.W.B., Sarnthein, M., Foster, G.L., Ridgwell, A., Grootes, P.M. and Elliott, T., 2014. Deep water formation in the North Pacific and deglacial CO<sub>2</sub> rise. *Paleoceanography*, 29(6): 645-667.
- Richardson, P.L., 2008. On the history of meridional overturning circulation schematic diagrams. *Progress in Oceanography*, 76(4): 466-486.
- Riethdorf, J.-R., Thibodeau, B., Ikehara, M., Nürnberg, D., Max, L., Tiedemann, R. and Yokoyama, Y., 2016. Surface nitrate utilization in the Bering sea since 180 ka BP: Insight from sedimentary nitrogen isotopes. *Deep Sea Research Part II: Topical Studies in Oceanography*, 125-126: 163-176.
- Sexton, P.F. and Barker, S., 2012. Onset of 'Pacific-style' deep-sea sedimentary carbonate cycles at the mid-Pleistocene transition. *Earth and Planetary Science Letters*, 321: 81-94.
- Shcherbina, A.Y., Talley, L.D. and Rudnick, D.L., 2003. Direct observations of North Pacific ventilation: Brine rejection in the Okhotsk Sea. *Science*, 302(5652): 1952-1955.
- Shigemitsu, M., Narita, H., Watanabe, Y.W., Harada, N. and Tsunogai, S., 2007. Ba, Si, U, Al, Sc, La, Th, C and <sup>13</sup>C/<sup>12</sup>C in a sediment core in the western subarctic Pacific as proxies of past biological production. *Marine Chemistry*, 106(3-4): 442-455.
- Sigman, D.M. and Boyle, E.A., 2000. Glacial/interglacial variations in atmospheric carbon dioxide. *Nature*, 407(6806): 859-869.
- Takahashi, T., Sutherland, S.C., Sweeney, C., Poisson, A., Metzl, N., Tilbrook, B., Bates, N., Wanninkhof, R., Feely, R.A. and Sabine, C., 2002. Global sea-air CO<sub>2</sub> flux based on climatological surface ocean pCO<sub>2</sub>, and seasonal biological and temperature effects. *Deep Sea Research Part II: Topical Studies in Oceanography*, 49(9-10): 1601-1622.
- Talley, L.D., 1993. Distribution and formation of North Pacific intermediate water. *Journal of Physical Oceanography*, 23(3): 517-537.
- Talley, L.D., 2013. Closure of the global overturning circulation through the Indian, Pacific, and Southern Oceans: Schematics and transports. *Oceanography*, 26(1): 80-97.
- Warren, B.A., 1983. Why is no deep water formed in the North Pacific? *Journal of Marine Research*, 41(2): 327-347.
- Yasuda, I., 2003. Hydrographic structure and variability in the Kuroshio-Oyashio transition area. *Journal of Oceanography*, 59(4): 389-402.
- Zhang, J., Wang, P., Li, Q., Cheng, X., Jin, H. and Zhang, S., 2007. Western equatorial Pacific productivity and carbonate dissolution over the last 550 kyr: Foraminiferal and nannofossil evidence from ODP Hole 807A. *Marine Micropaleontology*, 64(3-4): 121-140.

## **2. Material and Methods**

This thesis is involved in the AWI-GEOMAR joint project “SO264 SONNE-EMPEROR: The Plio/Pleistocene to Holocene development of the pelagic North Pacific from surface to depth – assessing its role for the global carbon budget and Earth’s climate”. Research project SO264 SONNE-EMPEROR was a marine research project aiming to advance the understanding of the North Pacific’s role in regulating ocean-atmosphere greenhouse gas exchanges before anthropogenic timescales. It focused on scientific questions related to paleoceanographic, paleoclimatic, chemical-oceanographic, and marine biological studies with an integrated approach and sampled from a broad meridional transect along the Emperor Seamount Chain in the NW Pacific in 2018. Research topics involved with different disciplines and focused on the long-term evolution of climate patterns in the area, the atmosphere-ocean exchange processes, the inter-dynamic development of different water masses, ocean circulation variability. The project was carried out systematically with different themes and contributed by both institutes on each theme.

Certain topics were assigned to be tackled by AWI, including dust supply, marine productivity, mode, intermediate, and deep water ventilation, formation, and circulation changes. This thesis was conducted within these topics which aimed to reconstruct the Pleistocene to Holocene climate development and oceanography in the subarctic to subtropical NW Pacific on millennial to orbital timescales.

### **2.1. Sample Material and Selection**

An extensive and successful coring result was carried out during cruise SO264 along the Emperor Seamount Chain from 33°N up to 51°N, covering from ~1700 m to ~5800 m water depth. Numerous long sediments cores were retrieved. In total, 40 gravity corers, 20 piston corers and 5 kasten corers were deployed with an overall sediment core recovery of ~640 m (Nürnberg, 2018b). Cores were logged, color-scanned, sampled and lithostratigraphic-described jointly by the Shipboard Science Party. Based on this initial shipboard results and difference interests from the project cooperating institutions, we prioritized a list of cores for X-ray fluorescence scanning (chapter 2.2.1). Considering the different topics, which related to different water depth, from both institutes, further selection of cores was done and sampled. A complete overview of all the scanned cores and the measurements that were accomplished is listed in Appendix 1.

For this thesis, deep sediment cores were mainly selected from SO264 and one additional core from another cruise SO202, which are all from the water depth around or deeper than 3000 m. An overview of the cores used in this thesis is given below in Table 2.1. In addition, in chapter 6, specific selection of cores from five more different cruises which are not listed in Table 2.1.

Table 2.1 Locations of the cores used in this thesis.

Core ID	Area/Seamount	Latitude	Longitude	Water depth (m)	Remarks
SO264-66-2	south of Detroit	50°15.064'N	168°17.818'E	2751	Chapter 4 and 6
SO264-64-1	south of Detroit	50°15.064'N	168°17.818'E	3495	Chapter 4 and 6
SO264-56-2	Minnetonka	47°44.752'N	168°40.398'E	3973	Chapter 6
SO264-55-1	Minnetonka	47°10.553'N	169°25.291'E	2936	Chapter 4 and 6
SO264-51-2	Minnetonka	47°10.548'N	169°25.282'E	2933	Chapter 4
SO264-45-2	Jimmu	46°33.792'N	169°36.072'E	2425	Appendix i
SO264-28-2	Suiko	44°51.546'N	170°03.983'E	1935	Chapter 6
SO264-15-2	east of Ninigi	41°36.917'N	170°25.340'E	3662	Chapter 4 and 6
SO264-13-2	Ojin & Jingu	37°47.865'N	170°43.327'E	3935	Chapter 6
SO202-37-2	north of Hess Rise	37°46.07'N	176°16.13'E	3568	Chapter 4, 5 and 6

## 2.2. Methods

While on board, all sediment cores were split into archive half and working half, and 10 cm<sup>3</sup> syringe samples were taken in 10 cm intervals from the working half into pre-weighed glass vials. All samples were stored at 4° C until further shore-based processing. The SO264 samples were shipped back and arrived at the AWI in November 2018. The prioritized cores were then XRF-scanned immediately on the archive half. On the working half, samples were taken or split into slices, weighted and freeze-dried before further analysis. The one core from SO202 also went through the same process. In the following, the principal methods that I conducted and measured in this thesis will be described.

As a side note, the alkenone method in chapter 4 and the machine learning method in chapter 6, will not be described in this chapter.

### 2.2.1. X-ray Fluorescence Scanning

X-ray fluorescence (XRF) core scanning provides a rapid and nondestructive analytical approach for obtaining semi-quantitative, high-resolution downcore variations of major and

minor elements. XRF-scanning measurements were carried out on the split archive halves with an Avaatech XRF core scanner at the AWI in Bremerhaven with 1 cm resolution. Prior to scanning, cores were rested for half hour to bring the surface sediment back to room temperature. The topmost surface sediment was scratched away to keep a fresh and smooth surface for scanning. A 4  $\mu\text{m}$  SPEXCerti Prep Ultralene® foil was applied on the sediment in order to achieve a higher transmission of weak fluorescence signals from light elements, such as Al, Si. If the foil is applied while the surface sediment is still cold, moisture and air bubbles can easily form underneath the foil reducing the scanning performance. The X-ray excitation scanning settings of the cores were 10 kV at 150  $\mu\text{A}$  with no filter for a count time of 10 s, 30 kV at 175  $\mu\text{A}$  with thick-Pb filter for 15 s, and 50 kV at 1000  $\mu\text{A}$  with Cu filter for 20 s. Sample distance was 10 mm, with a 10x12 mm slit size.

### **2.2.2. Sediment Preparation and Properties**

All the 10  $\text{cm}^3$  syringe samples were weighed before and after freeze-drying, and homogenized for bulk measurements, such as density, total carbon, total organic carbon and opal content.

For density, a pinch of sediment (ca. 1  $\text{cm}^3$ ) was measured on a four units Gas Pycnometer (AccuPyc II 1340) in the AWI Marine Geology Laboratory in Bremerhaven. Dry bulk density (DBD) for the calculation of mass accumulation rates (MAR) was carried out according to Dadey et al. (1992).

$$(1) \quad \rho_d = M_s/V$$

In which  $\rho_d = \text{DBD}$ ,  $M_s$  = the weight of the dry sample and  $V$  = the total volume of the wet sample. Mass accumulation rates were calculated as follows:

$$(2) \quad \text{MAR} = \text{DBD} \times \text{sedimentation rate}$$

### **2.2.3. CaCO<sub>3</sub> and TOC Measurements**

The weight percentage of carbonate ( $\text{CaCO}_3$  wt%) was also obtained from the homogenized samples. For SO264 cores, at least 40 samples from each core were selected based on the initial XRF scanning calcium (Ca) counts data and measured, otherwise samples were measured in 10 cm samples spacing like core SO202-37-2 (in total ca. 240 samples).

For determining TC, grinded samples were wrapped in specific tin capsules and measured with a CNS-analyzer (Elementar vario EL III). For TOC, the samples need to be prepared the day before for decalcification. Pinch of sediments were placed in a ceramic crucible and few drops of ethanol and hydrochloric acid were added to dissolve the carbonate. The samples were then dried on a heating plate with medium heat for one night and then went on measurement with a carbon/sulfur analyzer (Eltra CS-800). All analysis above were done at the AWI in Bremerhaven. The  $\text{CaCO}_3$  wt% was then calculated from the difference between TC and TOC as follows:

$$(3) \quad \text{CaCO}_3 \text{ wt\%} = (\text{TC} - \text{TOC}) \times 8.333 \times 100\%$$

Mass accumulation rates of carbonate (CAR) were calculated as the product of dry bulk density (DBD), sedimentation rate and carbonate percentage:

$$(4) \quad \text{CAR} = \text{DBD} \times \text{sedimentation rate} \times \text{CaCO}_3 \text{ wt\%}$$

#### 2.2.4. Stable Isotope Measurements

For stable isotope measurements, 1 cm thick continuously sampled slices from the working half of the core were used. Samples were freeze-dried and washed through a 63- $\mu\text{m}$  sieve. The coarse fractions were then dried in an oven at 50°C and fractionated into four size fractions of 63-125  $\mu\text{m}$ , 125-250  $\mu\text{m}$ , 250-500  $\mu\text{m}$  and >500  $\mu\text{m}$ . While processing those samples, sediments were weighed both before wet sieving and after drying to obtain the sediment sand (>63- $\mu\text{m}$ ) weight fraction as a carbonate dissolution.

In principle, every second or third 1 cm slice was processed for isotope measurement. The lower half of core SO264-55-1 was unfortunately in low resolution (every 10 cm slice was processed) due to the lack of time. All data, including data which was not used in this thesis, is listed in Appendix 2.

Two specimens of the epibenthic foraminifera (*Cibicidoides wuellerstorfi* and *Cibicidoides mundulus*) and the planktonic foraminifera (*Uvigerina peregrina*, *Uvigerina senticosa* and *Globgerina bulliodes*) were picked from the 250-500  $\mu\text{m}$  size fraction for measurement. All isotope measurements were done at the AWI in Bremerhaven, using a Thermo Finnigan MAT 253 isotope ratio mass-spectrometer coupled to an automated KIEL IV CARBO preparation device. Stable oxygen isotope ratios ( $\delta^{18}\text{O}$ ) and stable carbon isotope ratios ( $\delta^{13}\text{C}$ ) are expressed in the  $\delta$ -notation with reference to Vienna Peedee belemnite (VPDB). Long-time

reproducibility based on NIST-19 and an in-house carbonate standard is  $\pm 0.06$  ‰ for  $\delta^{18}\text{O}$  and  $\pm 0.04$  ‰ for  $\delta^{13}\text{C}$ .

### 2.2.5. AMS $^{14}\text{C}$ Measurements

Accelerator mass spectrometry (AMS)  $^{14}\text{C}$  radiocarbon dates were measured on calcareous tests of planktonic foraminifera *Globigerina bulloides*, *Neogloboquadrina dutertrei* and *Neogloboquadrina pachyderma (dex)*, and benthic foraminifera *Uvigerina senticosa*. In order to fulfill sufficient carbonate weight for measurement, around 50 to 80 specimens were picked from the 250-500  $\mu\text{m}$  size fraction. The radiocarbon dating was acquired on the Mini Carbon Dating System (MICADAS) in the  $^{14}\text{C}$  dating laboratory at the AWI in Bremerhaven. All AMS  $^{14}\text{C}$  ages were converted into calibrated 1-sigma calendar age ranges using the online software CALIB 8.2 (Stuiver and Reimer, 1993) with the atmospheric calibration curve INTCAL20 (Reimer et al., 2020). The ventilation ages of deep water masses were calculated as the difference between the benthic and planktonic (B-P)  $^{14}\text{C}$  ages, in years (yrs) as unit.

## 2.3. Reference

- Dadey, K. A., Janecek, T., & Klaus, A. (1992). *Dry-bulk density: its use and determination*. Paper presented at the Proceedings of the Ocean Drilling Program, Scientific Results.
- Nürnberg, D. (2018). *RV SONNE Fahrtbericht / Cruise Report SO264 - SONNE-EMPEROR: The Plio/Pleistocene to Holocene development of the pelagic North Pacific from surface to depth – assessing its role for the global carbon budget and Earth's climate, Suva (Fiji) – Yokohama (Japan), 30.6. – 24.8.2018*. Retrieved from Kiel, Germany
- Reimer, P. J., Austin, W. E., Bard, E., Bayliss, A., Blackwell, P. G., Ramsey, C. B., Butzin, M., Cheng, H., Edwards, R. L., Friedrich, M. (2020). The IntCal20 Northern Hemisphere radiocarbon age calibration curve (0–55 cal kBP). *Radiocarbon*, 62(4), 725-757.
- Stuiver, M., & Reimer, P. J. (1993). Extended  $^{14}\text{C}$  data base and revised CALIB 3.0  $^{14}\text{C}$  age calibration program. *Radiocarbon*, 35(1), 215-230.

### 3. Age Model Approach for the Emperor Seamount Chain Region

Based on the preliminary shipboard results from inspection of tephra layers and the magnetic susceptibility, we had an initial correlation between cores from different seamount regions (Nürnberg, 2018b). Further detailed analyses of the geochemical composition and ages of multiple tephra layers were carried out post-cruise by project partners from the Shirshov Institute of Oceanology and the Institute of Volcanology and Seismology in Russia. The most promising and recognizable tephra layer is the Pauzhetka tephra with a dated age of 421 ka, occurring within Termination V, i.e., at the transition between MIS 12 and 11 (Ponomareva et al., 2018). We were also able to identify and correlate this tephra layer in most of the cores by XRF-derived K/Ti ratios, since the tephra yields a distinct potassium maximum in sediments (Nürnberg, 2018b; Ponomareva et al., 2018).

In a next step, we correlated XRF-derived Ba/Ti (proxy for paleo-productivity) and Ca/Ti (carbonate production) ratios to a proximal regional reference record, Ocean Drilling Program (ODP) Site 882 (50°21'N, 167°35'E, 3244 m water depth). The well-established stratigraphy of Site 882 is based on a combination of paleomagnetic evidence, and orbital tuning of both shipboard logging and post-cruise XRF-scanning data to global reference records and provided the information of the resemblance between biogenic Barium with transient CaCO<sub>3</sub> maxima during peak interglacials in the otherwise carbonate-free sediments (Jaccard et al., 2005; Tiedemann and Haug, 1992).

To fine-tune the initial XRF correlation, further iterations were carried out by comparing the correlated ln-Ba/Ti and ln-Ca/Ti records to the detrital input signal by using either potassium (K) or iron (Fe) counts to adjust and check if phase shifts or irregularities occur or the achieved correlation patterns hold throughout different time series, i.e., matching to relatively higher detrital input, and vice versa. A schematic example of the XRF-scanning-based correlation illustrates the approach across different cores from the northern Emperor Seamount Chain to the reference core Site 882 (Figure 3, for core locations, please *cf.* Appendix 1).

With regard to the XRF-ratio normalization, both Al and Ti are exclusively of detrital origin and normally can be used for normalization. I chose to normalize against Ti in this thesis, not only because its variations are more clearly expressed, but primarily because elemental intensities of light elements like Al can be strongly influenced by changes in water content, which is trapped between the sediment and the scanning foil (Tjallingii et al., 2007). Moreover,



previous calibration studies (e.g., Weltje and Tjallingii, 2008) indicated that in order to provide the most reliable signals in relative changes of down-core elements, the natural logarithmic ratios of XRF core scanner raw data should be adopted. Therefore, hereafter, I present the XRF elemental variations in the ln-element/Ti format.

In order to verify the individual XRF-based age models leading to the proposed regional stratigraphic framework (cf. chapter 4), I measured the stable isotopic composition of the endobenthic *Uvigerina spp.* and the epibenthic *C. wuellerstorfi*, and used the acquired  $\delta^{18}\text{O}$  time series from selected to correlate to the benthic  $\delta^{18}\text{O}$  stack of Lisiecki and Raymo (Lisiecki and Raymo, 2005). For the core tops, I used AMS  $^{14}\text{C}$  ages from planktic foraminifera *G. bulloides* to define the upper end of the sedimentary sequences.

This latter step was especially useful since the XRF-based age model approach becomes less reliable southward along the Emperor Seamount Chain, as the ln-Ba/Ti amplitudes gradually decrease towards the south, and ln-Ca/Ti ratios appeared resemble only parts of the ln-Ba/Ti ratio variations, instead of providing clearly defined short interglacial peaks. Overall, the results provided significant agreement between the acquired isotope stratigraphy and the XRF-based age models of the studied cores, proving the potential to establish age models in the NW Pacific region using an XRF correlation approach.

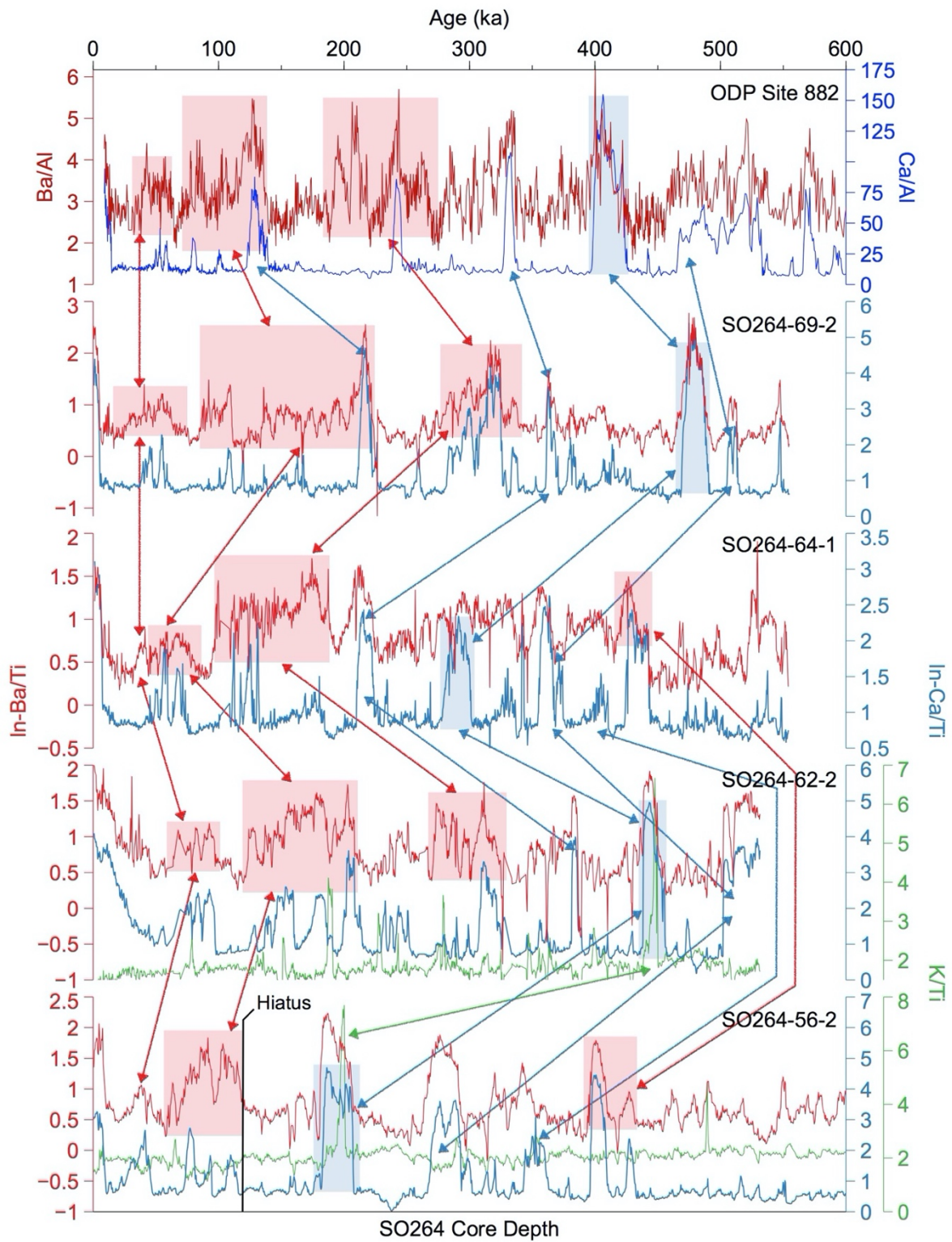


Figure 3. Schematic illustration of XRF core correlation patterns following the XRF-based age model approach. The top panel shows productivity-related Ba/Al and Ca/Al records from Site 882 against age (Jaccard et al., 2010). The four lower panels show XRF In-Ba/Ti (red lines), In-Ca/Ti (blue lines) and K/Ti (green lines) data from four SO264 cores, from north to south, located at northern Emperor Seamount Chain against corresponding core depth (for illustrative purposes, hence exact depths not shown here). The relevant color arrows and shaded areas are the correlation pattern or peak(s) between each core.

### 3.1. Reference

- Jaccard, S. L., Haug, G. H., Sigman, D. M., Pedersen, T. F., Thierstein, H. R., & Röhl, U. (2005). Glacial/interglacial changes in subarctic North Pacific stratification. *Science*, 308(5724), 1003-1006.
- Jaccard, S., Galbraith, E., Sigman, D.M. and Haug, G., 2010. A pervasive link between Antarctic ice core and subarctic Pacific sediment records over the past 800 kyrs. *Quaternary Science Reviews*, 29(1-2): 206-212.
- Lisiecki, L. E., & Raymo, M. E. (2005). A Pliocene-Pleistocene stack of 57 globally distributed benthic  $\delta^{18}\text{O}$  records. *Paleoceanography*, 20(1).
- Nürnberg, D. (2018). *RV SONNE Fahrtbericht / Cruise Report SO264 - SONNE-EMPEROR: The Plio/Pleistocene to Holocene development of the pelagic North Pacific from surface to depth – assessing its role for the global carbon budget and Earth's climate, Suva (Fiji) – Yokohama (Japan), 30.6. – 24.8.2018*. Retrieved from Kiel, Germany
- Ponomareva, V., Bubenshchikova, N., Portnyagin, M., Zelenin, E., Derkachev, A., Gorbarenko, S., Garbe-Schönberg, D., Bindeman, I. (2018). Large-magnitude Pauzhetka caldera-forming eruption in Kamchatka: Astrochronologic age, composition and tephra dispersal. *Journal of Volcanology and Geothermal Research*, 366, 1-12.
- Tjallingii, R., Röhl, U., Kölling, M., & Bickert, T. (2007). Influence of the water content on X-ray fluorescence core-scanning measurements in soft marine sediments. *Geochemistry, Geophysics, Geosystems*, 8(2).
- Tiedemann, R. and Haug, G.H., 1992. Astronomical calibration of Site 882 cycle stratigraphy in the northwest. In: Rea, D.K., Basov, I.A., Scholl, D.W., and Allan, J.F. (Eds.). *Proceedings of the Ocean Drilling Program, Scientific Results (CD-ROM)*, 145: 283-292.
- Weltje, G. J., & Tjallingii, R. (2008). Calibration of XRF core scanners for quantitative geochemical logging of sediment cores: Theory and application. *Earth and Planetary Science Letters*, 274(3-4), 423-438. doi:10.1016/j.epsl.2008.07.054

## 4. Glacial-interglacial variations of productivity and carbonate deposition in the Northwest Pacific during the last 500,000 years

Chao, Weng-Si<sup>1\*</sup>, Jacobi, Lara<sup>2</sup>, Niederbockstruck, Bryan<sup>1,3</sup>, Langemann, Linda<sup>1</sup>, Kuhn, Gerhard<sup>1</sup>, Zou, Jian-Jun<sup>4</sup>, Shi, Xue-Fa<sup>4</sup>, Nürnberg, Dirk<sup>2</sup>, Tiedemann, Ralf<sup>1</sup>, Lembke-Jene, Lester<sup>1</sup>

<sup>1</sup> Alfred-Wegener-Institut Helmholtz-Zentrum für Polar- und Meeresforschung, Bremerhaven, Germany

<sup>2</sup> GEOMAR Helmholtz-Zentrum für Ozeanforschung, Kiel, Germany

<sup>3</sup> Now at MARUM, Bremen, Germany

<sup>4</sup> First Institute of Oceanography, Ministry for Natural Resources, Qingdao, China

\*Corresponding author: weng-si.chao@awi.de

Keywords: North Pacific, subarctic Pacific, carbonate cycles, carbonate dissolution, productivity

Submitting journal: *Frontiers in Earth Science*

Last updated: 02.01.2023

### Abstract

The modern North Pacific constitutes one of the main marine natural carbon sinks and thus helps regulate atmospheric CO<sub>2</sub> concentrations. However, the relationship between biological export production (biological carbon pump), deep sea carbonate deposition, and meridional overturning circulation in shaping this marine carbon reservoir remains poorly understood on geological timescales. In particular, the combination of these processes beyond the last glacial cycle and across the dynamic subarctic and subtropical gyre regions with their dominant Western Boundary Current systems (Kuroshio/Oyashio) has been proven to be dynamic and highly regionalized. We here present a suite of new sediment records along a meridional transect from the subpolar Northwest (NW) Pacific, retrieved from the Emperor Seamount Chain and Hess Rise, in order to reconstruct changes in the export production and its relation to carbonate deposition and dissolution on suborbital timescales for the last 500,000 years

before present (500 ka BP). We used X-ray fluorescence (XRF)-scanning records to correlate prominent patterns between sediment cores, supported by high-resolution oxygen isotope time series of epibenthic foraminifera *Cibicidoides wuellerstorfi* to develop a coherent stratigraphic framework for the study area. Our sediment records show southward decreasing productivity variations, as evidenced in XRF-ln Ba/Ti ratios, and dust supply, based on XRF-Fe intensities, from 52 to 37° N. Higher export production occurred during peak interglacials, but an out-of-phase pattern exists in carbonate deposition below 40°N. We assume that regional shifts in the subpolar and subtropical gyre circulation and upper ocean stratification exerted a major control on the macro-nutrient supply, rather than solely changing amount of micronutrient input through aeolian transport. On the other hand, the productivity in the subpolar region had a more direct influence and depositional contribution on the carbonate system supported by coherent increases in biogenic barium, carbonate flux, alkenone concentration, sand fraction and opal content during interglacials. The Hess Rise carbonate preservation, however, showed weak correlation to the productivity signals but matched to the deep Pacific carbonate chemistry changes which relate to variations in carbonate dissolution. The inconsistency between these productivity and carbonate records also implied the boundary shifting between the subpolar and subtropical gyre which provide different nutrient regime to the NW Pacific region.

#### **4.1. Introduction**

Today, the North Pacific plays an important role in the oceanic carbon cycle and global climate, due to its vast size, its high biological export production and potential for deep carbon storage in the form of dissolved inorganic carbon (DIC). It also comprises one of the three major high-nutrient low-chlorophyll (HNLC) regions of the global ocean, which are characterized by upwelling of nutrient-rich deep waters into the photic zone and remain partially unutilized due to micronutrient or light limitation (Falkowski et al., 1998). Hence, the biological carbon pump is not working efficiently in fixing carbon into sinking organic matter, in comparison to the co-occurring release of carbon from deep water masses. The macro-nutrient supply is constrained by the strength of the permanent salinity-driven density gradient (halocline) in the North Pacific.

On glacial-interglacial timescales, a number of subarctic Northwest (NW) Pacific reconstructions show lower export production (e.g., biogenic opal, biogenic barium) during glacials, with a remarkable correlation to Antarctic climatic and greenhouse gas changes preserved in ice cores (e.g. Jaccard et al., 2010; Jaccard et al., 2005; Narita et al., 2002;

Nürnberg and Tiedemann, 2004; Shigemitsu et al., 2007). Evidence based nutrient utilization proxies indicates low export production. Hence, nitrate consumption in the North Pacific was more complete during glacials, contributing to lowered surface ocean nutrient content including carbon (e.g. Brunelle et al., 2007; Galbraith et al., 2008; Knudson and Ravelo, 2015a). Causes were most likely decreased vertical exchange through strengthened surface ocean stratification and increased surface isolation during glacials, suggesting less nutrient supply from nutrient-rich deep waters (Brunelle et al., 2007; Galbraith et al., 2008; Gebhardt et al., 2008; Jaccard et al., 2010; Jaccard et al., 2009; Jaccard et al., 2005; Kienast et al., 2004; Narita et al., 2002; Shigemitsu et al., 2007). The decrease of this physical transfer of deeply sequestered DIC to the surface ocean also potentially contributed to lower glacial atmospheric CO<sub>2</sub> concentrations. In combination with enhanced supply of dust-derived, or marine-transported, iron (Fe) as essential micronutrient, these processes set the upper NW Pacific as an efficient driver of glacial atmospheric CO<sub>2</sub> drawdown.

However, differing nutrient preferences for siliceous and carbonate planktic organisms in biological primary production, their relative contributions towards export production (i.e., the biological carbon pump), and the resulting deep-sea carbonate deposition, i.e., the role of carbonate counter-pump remain poorly understood in this region. In particular, whether the calcium carbonate (CaCO<sub>3</sub>) content of deep-sea sediments in the North Pacific is mainly controlled by either surface biological production or changes in carbonate preservation related to the paleo-chemical configuration of deep-water masses, has consequences for the deep oceanic carbon storage capacity and its relationship with climate change.

Deep-sea carbonate deposition has been studied for a long time and the patterns of Atlantic and Pacific CaCO<sub>3</sub> preservation are known for their anti-correlation, at least for the last ca. 500 ka BP (Sexton and Barker, 2012). They are most clearly expressed in significant changes in the carbonate compensation depth (CCD), the upper limit of the zone where less than 5-10 weight % (wt %) of CaCO<sub>3</sub> accumulates on the seafloor. The glacial Atlantic CaCO<sub>3</sub> content is generally lower in comparison to interglacials, the so-called “Atlantic-type” (Bé et al., 1976; Berger, 1973; Crowley, 1985; Curry and Lohmann, 1990; Damuth, 1977; deMenocal et al., 1997; Gardner, 1975; Hodell et al., 2001; Verardo and McIntyre, 1994; Volat et al., 1980). On the contrary, the “Pacific-type” generally exhibits higher CaCO<sub>3</sub> contents during glacials (Anderson et al., 2008; Arrhenius, 1952; Berger, 1973; Farrell and Prell, 1989; Farrell and Prell, 1991; Hays et al., 1969; Karlin et al., 1992; LaMontagne et al., 1996; Le and Shackleton, 1992; Thompson and Saito, 1974; Zahn et al., 1991). The causes of these opposed CaCO<sub>3</sub> cycles have

been discussed controversially, with controlling factors ascribed to various reasons, such as carbonate production from surface waters, dilution by non-carbonate materials (e.g., opal), or dissolution driven by changes in carbonate ion concentration [ $\text{CO}_3^{2-}$ ] of the deep-water masses. In particular the latter process has been in turn linked to the supply of bathyal to abyssal southern-sourced Circumpolar Deep Water for the last ca. 1 Ma BP (Sexton and Barker, 2012). In that case, better ventilated and hence less carbonate-corrosive deep waters, sourced mainly from the South Pacific and Ross Sea sector of the Southern Ocean, would have led to better carbonate preservation in the Pacific during glacials, relative to the Atlantic.

In this study, we present four proxy-based carbonate and biological export production time series from sediment cores along a meridional transect from the NW Pacific covering the last 500 ka BP. The records are mainly based on high-resolution XRF-derived Ba, Ca,  $\text{CaCO}_3$  contents and accumulation rates, supplemented by discrete measurements of alkenone concentrations and coarse fraction percent ( $>63 \mu\text{m}$ , sand %) on select time intervals. We investigate the relation between the carbonate deposition and productivity in the NW Pacific over the last five glacial cycles and assess the potential causes of the subarctic NW Pacific carbonate system.

## **4.2. Study area and oceanographic setting**

The North Pacific constitutes one of the largest ocean basins, crossing several climatic zones from the tropical to the polar domain. Water depths range mostly in the abyssal zone below 4000 m, with only a few shallower locations along seamounts and ridge systems. Due to the extensive geographical range, the North Pacific is influenced by (sub-)tropical climates from the West Pacific Warm Pool, the El Niño – Southern Oscillation (ENSO) as well as East Asian Monsoon dynamics. No deep-water formation occurs in the North Pacific due to the presence of a permanent halocline (Warren, 1983). This halocline stratification is controlled by high precipitation rates and limited meridional flow of salty subtropical water (Emile-Geay et al., 2003). This comparably strong stratification today leads to the area acting as a net sink of atmospheric  $\text{CO}_2$  (Takahashi et al., 2002). The intermediate depths in the NW Pacific are mainly occupied by North Pacific Intermediate Water (NPIW) sourced from the Okhotsk Sea (Shcherbina et al., 2003; Talley, 1993). Below 2000 m depth, the North Pacific Deep Water (NPDW) is the dominant water mass, sourced from Lower Circumpolar Deep Water (LCDW) from the Southern Hemisphere by northward transport (Reid and Lonsdale, 1974).

The upper ocean water masses are characterized by a clockwise subtropical circulation and a counterclockwise subarctic circulation. Warm water masses from the equatorial Pacific are transported along the eastern coast of Japan and flow eastward as the Kuroshio Extension into the NW Pacific (Figure 1A). This relatively warm water flows until it diverges on the American west coast and part of it is transported north and westwards into the Alaskan Stream along the Aleutian Islands. After flowing southward as the East Kamchatka Current, the cold and nutrient-rich Oyashio Current forms East of the Kurile Island Chain. The deflection point of the Oyashio eastwards into the open Pacific defines the North Pacific Subarctic Front. Today, the western North Pacific Subarctic Front is located around 38 to 41°N, and identified by changes of the meridional temperature and salinity gradient (Yuan and Talley, 1992).



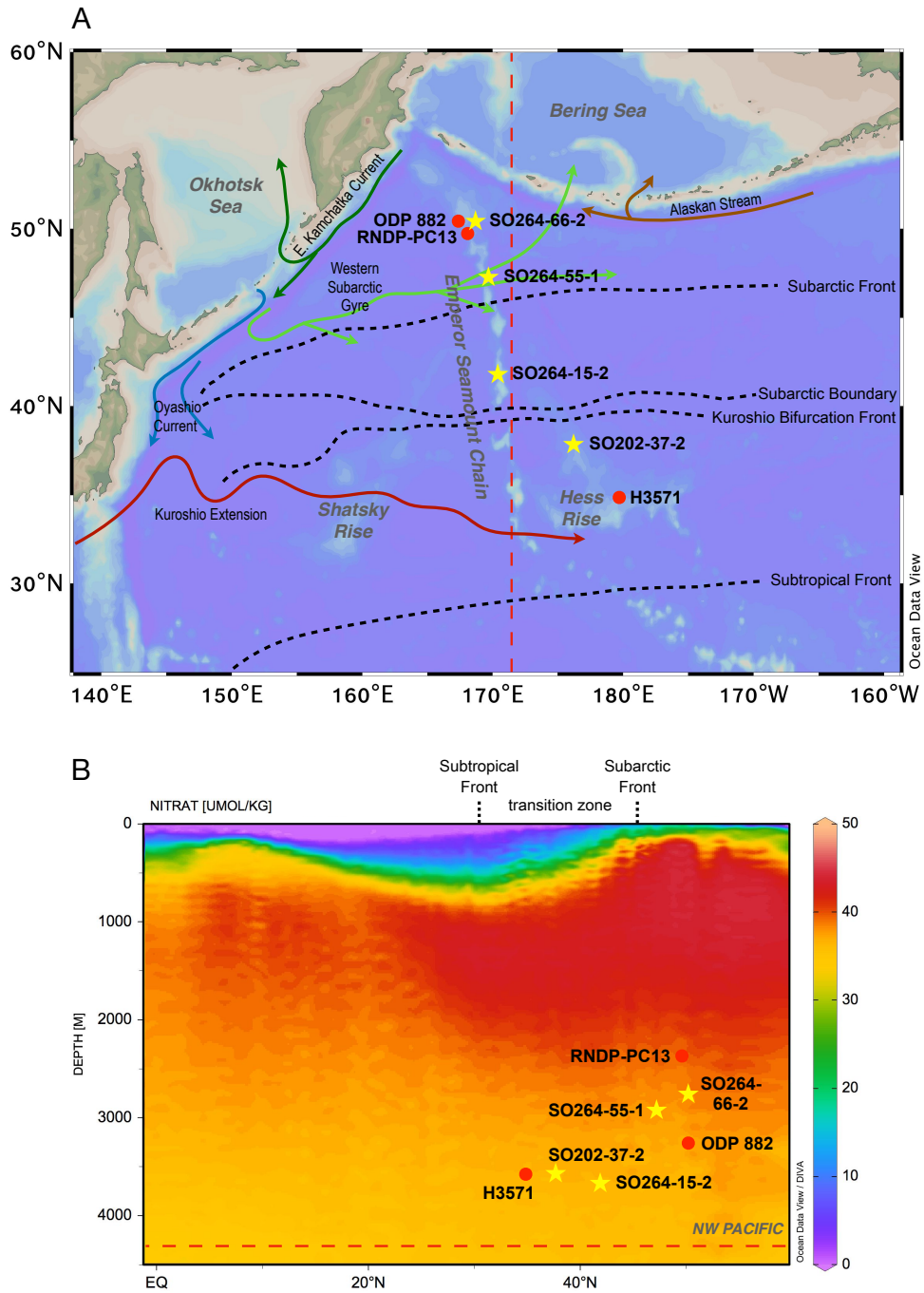


Figure 3. (A) Map of the research region. The study cores are marked by yellow stars and the Northwest Pacific reference cores are marked by red dots. The major surface ocean currents and fronts are marked by arrows and black dashed lines, based on Yasuda (2003). SO264-51-2 is a twin core of SO264-55-1 which both have the same coring location and water depth. (B) Nitrate concentration along a zonal section indicated by the red dashed line in (A), with positions of the study and reference cores in water depth.

Compared to the near-absence of macro-nutrients in the Subtropical Gyre (STG), the Subarctic Gyre (SAG) is highly enriched in nitrate. Overall productivity is higher in the SAG, but less effective due to a lack of micronutrients, in particular iron. For the STG, the water is oligotrophic due to a deep permanent thermocline, preventing the upwelling of nutrients into the photic zone (Figure 1B). The transition zone, or Mixed Water Region is defined as the area

between the Subarctic Front and the Subtropical Front (Figure 1B). The northern end of this transition zone constitutes the Subarctic Front, acting as the boundary to the SAG. The Subarctic Front in the North Pacific is characterized by changes in the physical characteristics. The Mixed Water Region has been shown to change on geological timescales in the past (Gray et al., 2020; Isono et al., 2009; Oba and Murayama, 2004; Yasudomi et al., 2014), and is projected to change under future global warming (Yang et al., 2020; Yang et al., 2016), thereby affecting heat and nutrient transport throughout the entire North Pacific. The Mixed Water Region and both gyre systems are of importance regarding the CO<sub>2</sub> uptake from the atmosphere into the ocean. On an annual basis, the North Pacific acts as a net sink for CO<sub>2</sub>, with the most effective area of CO<sub>2</sub> sequestration in the North Pacific occurring around 30 to 40° (Takahashi et al., 2002; Takahashi et al., 2009).

### 4.3. Material and Methods

The investigated meridional transect ranges from 37 to 49°N latitude along the Emperor Seamount Chain in the subarctic NW Pacific, crossing the Subarctic Front, the Subarctic Boundary and the Kuroshio Bifurcation Front, which is defined by the inflow of the two NW Pacific coastal currents, the cold subarctic Oyashio Current and the warm subtropical Kuroshio Current Extension (Figure 1A). We selected four sediment cores along this transect: three cores were recovered during expedition SO264 of R/V SONNE in 2018, while one was taken from Hess Rise during a previous expedition SO202 INOPEX in 2009 also with R/V SONNE (Figure 1A and Table 1).

The sedimentary facies of the area from the Minnetonka Seamount to the northern Detroit Seamounts features dark olive green silty clays, which are mainly intercalated with brown to yellowish-brown diatom oozes and terrigenous components. In contrast, the southern area from Ninigi Seamount to Hess Rise is dominated by gray to light brown foraminifera-bearing silty calcareous oozes, interbedded with light gray to greenish-gray clayey calcareous oozes (Nürnberg, 2018b). Several tephra layers were found in most of the cores.

Table 2. Core locations of the study and reference cores in the Northwest Pacific.

	Core ID	Area/Seamount	Latitude	Longitude	Water depth (m)	Notes
Cores in this study	SO264-66-2	south of Detroit	50°15.064'N	168°17.818'E	2751	
	SO264-55-1	Minnetonka	47°10.553'N	169°25.291'E	2936	
	SO264-51-2	Minnetonka	47°10.548'N	169°25.282'E	2933	

	SO264-15-2	east of Ninigi	41°36.917'N	170°25.340'E	3662	
	SO202-37-2	north of Hess Rise	37°46.07'N	176°16.13'E	3568	
Reference cores	ODP 882	Detroit	50°21.798'N	167°35.9879'E	3255	<i>Jaccard et al., 2010</i>
	RNDP-PC13	open western subarctic Pacific	49°43.0859'N	168°18.1139'E	2393	<i>Brunelle et al., 2010</i>
	H3571	Hess Rise	34°54.25'N	179°42.18'E	3571	<i>Kawahata et al., 2000</i>

### 4.3.1. X-ray fluorescence (XRF) core scanning

XRF core scanning provides a rapid and nondestructive analytical approach for obtaining semi-quantitative, high-resolution downcore variations of major and minor elements. XRF-scanning measurements were carried out on the split archive halves of all cores with an Avaatech XRF core scanner at the Alfred-Wegener-Institut Helmholtz-Zentrum für Polar- und Meeresforschung (AWI) in Bremerhaven, Germany. The X-ray excitation scanning settings of the cores were 10 kV at 150  $\mu$ A with no filter for a count time of 10 s, 30 kV at 175  $\mu$ A with thick-Pb filter for 15 s, and 50 kV at 1000  $\mu$ A with Cu filter for 20 s. Sample distance was 10 mm, with a 10x12 mm slit size.

### 4.3.2. Bulk sample processing and physical properties

For the determination of bulk sediment parameters and physical properties, immediately after opening the sediment cores on board, we took syringe samples of 10 cubic centimeters in 10 cm intervals from the working halves into pre-weighed glass vials. All samples were stored at 4°C until further shore-based processing. Samples were weighed before and after freeze-drying, homogenized and measured for density calculations on four AccuPyc II 1340 Gas Pycnometer units in the AWI Marine Geology Laboratory in Bremerhaven.

Dry bulk density (DBD) for the calculation of mass accumulation rates (MAR) was carried out according to Dadey et al. (1992).

$$(1) \quad \rho_d = M_s/V$$

In which  $\rho_d$  = DBD,  $M_s$  = the weight of the dry sample and  $V$  = the total volume of the wet sample.

The carbonate content, expressed as weight percent (wt. %), was obtained from freeze-dried and homogenized samples. For SO264 cores, around 40 samples per core were selected based on the initial XRF scanning Ca data and measured, while ca. 240 samples were measured

from core SO202-37-2 with 10 cm sample spacing. Total carbon (TC) content was measured with an Elementar Vario EL III CNS-analyzer and total organic carbon (TOC) content was determined from decalcified samples with an Eltra CS-800 carbon/sulfur analyzer at the AWI in Bremerhaven. The carbonate content was then calculated from the difference between TC and TOC as follows:

$$(2) \quad CaCO_3 \text{ wt\%} = (TC - TOC) \times 8.333 \times 100\%$$

Mass accumulation rates were calculated as follows:

$$(3) \quad MAR = DBD \times \text{sedi. rate}$$

Mass accumulation rates of carbonate (CAR) were calculated as the product of dry bulk density, sedimentation rate and carbonate percentage:

$$(4) \quad CAR = DBD \times \text{sedi. rate} \times CaCO_3 \text{ wt\%}$$

### 4.3.3. Coarse fraction processing and stable isotopes measurements

For stable isotope measurements and foraminifera counts, we continuously sampled all cores in 1 cm-thick sediment slices from the working half rounds. Samples were freeze-dried and washed through a 63- $\mu\text{m}$  sieve. The coarse fractions were dried in an oven at 50°C and dry sieved into four size fractions of 63-125  $\mu\text{m}$ , 125-250  $\mu\text{m}$ , 250-500  $\mu\text{m}$  and >500  $\mu\text{m}$ .

While processing those samples, sediments were weighed both before and after wet sieving to obtain the sediment sand (>63- $\mu\text{m}$ ) weight fraction as a carbonate dissolution parameter. Every second 1 cm slice was processed for isotope measurements and foraminifera counting. Most of the stable oxygen isotope ratios ( $\delta^{18}\text{O}$ ) of core SO264-55-1 have been presented in a MSc. thesis and were largely measured on the endobenthic foraminifera *Uvigerina peregrina* and *Uvigerina senticosa* from the 250-500  $\mu\text{m}$  size fraction. For core SO202-37-2, two specimens of the epibenthic foraminifera *Cibicidoides wuellerstorfi* were picked from the same size fraction for  $\delta^{18}\text{O}$  and were measured at the AWI in Bremerhaven, using a Thermo Finnigan MAT 253 isotope ratio mass-spectrometer coupled to an automated KIEL IV CARBO preparation device. Long-time reproducibility based on NIST-19 and an in-house carbonate standard is 0.06 ‰ for  $\delta^{18}\text{O}$ .

#### 4.3.4. AMS <sup>14</sup>C ages

AMS <sup>14</sup>C ages of core SO202-37-2 were measured on the planktonic foraminifera *Globigerina bulloides* (*G. bulloides*) from the 250-500 µm size fraction and were obtained from the accelerator mass spectrometer Mini Carbon Dating System (MICADAS) at AWI. All radiocarbon ages were converted into calibrated 2-sigma calendar age ranges using the radiocarbon calibration tool CALIB Execute Version 8.20 (<http://calib.org/calib/>) with the MARINE20 calibration curve (Table S1).

#### 4.3.5. Alkenone content

We used 1 cm-thick freeze-dried sediment slices and applied selective accelerated solvent extraction (ASE; Auderset et al., 2020) for the extraction of n-alkanes, alkenones and GDGTs used a Dionex ASE350 system. This system is equipped with 10 mL stainless steel extraction cells, filled with 3-5 g of dry silica gel (60 Å, 70-230 mesh), previously deactivated by 5% milli-Q water, soaked with 3-5 g of hexane. Muffled glass fiber filters were added between the silica gel and the sediment (0.5-1.5 g) and on the top of the sample Internal standards for alkanes, alkenones and GDGT's (squalene, C<sub>36</sub> n-alkane, nC<sub>46</sub>-GDGT) were added prior to extraction to quantify the sample recovery and the concentration of the biomarker within the sediment. During the extraction and separation, the cell was preheated to 100 °C, filled with 10 ml of hexane, heated for 5 min and held in a static cycle for 2 min. Hexane was flushed through the cells into the first collecting vial. After the hexane flush, 10 ml of DCM was injected three times heated for 5 min and held in a static cycle for 2 min before the first flush and without static cycle in the 2nd and 3rd flushes.

#### 4.4. Age model

The non-destructive high-resolution XRF core scanner has been often used in reconstructions of paleoenvironmental and paleoceanographic changes via various elemental ratios. In NW Pacific sediment records, e.g. XRF-derived Barium (Ba) and Calcium (Ca) counts normalized against terrigenous background elements like Aluminum (Al), Potassium (K) or Titanium (Ti) have served as proxies for paleo-productivity (biogenic barium), while Ca (calcium carbonate content) has been used for assessing carbonate production vs. bottom water corrosivity and hence of alkalinity (Gebhardt et al., 2008; Jaccard et al., 2010; Jaccard et al., 2005). Jaccard et al. (2005) amended the existing stratigraphy by an XRF-based high-resolution

record on Ocean Drilling Program (ODP) Site 882 (50°21'N, 167°35'E, 3244 m water depth). The biogenic Barium (indicated by Ba/Al) showed a strong resemblance with the EDC CO<sub>2</sub>, in conjunction with transient CaCO<sub>3</sub> (indicated by Ca/Al) maxima during peak interglacials in the otherwise carbonate-free sediments. In our study, Site 882 serves as the regional reference record for comparisons of the productivity records from our Emperor Seamount Chain and Hess Rise sediment cores.

Although Al and Ti are both exclusively of detrital origin and normally can be used for XRF-ratio normalization, we preferred to normalize against Ti in this study, because its variations are more clearly expressed, and also elemental intensities of light elements like Al can be strongly influenced by the increase of water content, which is trapped between the sediment and the scanning foil (Tjallingii et al., 2007). In addition, previous calibration studies (e.g. Weltje and Tjallingii, 2008), indicated that in order to provide the most reliable signals in relative changes of down-core elements, the natural logarithmic ratios of XRF core scanner raw data should be adopted. Therefore, we present our XRF elemental variations in the ln-element/Ti format.

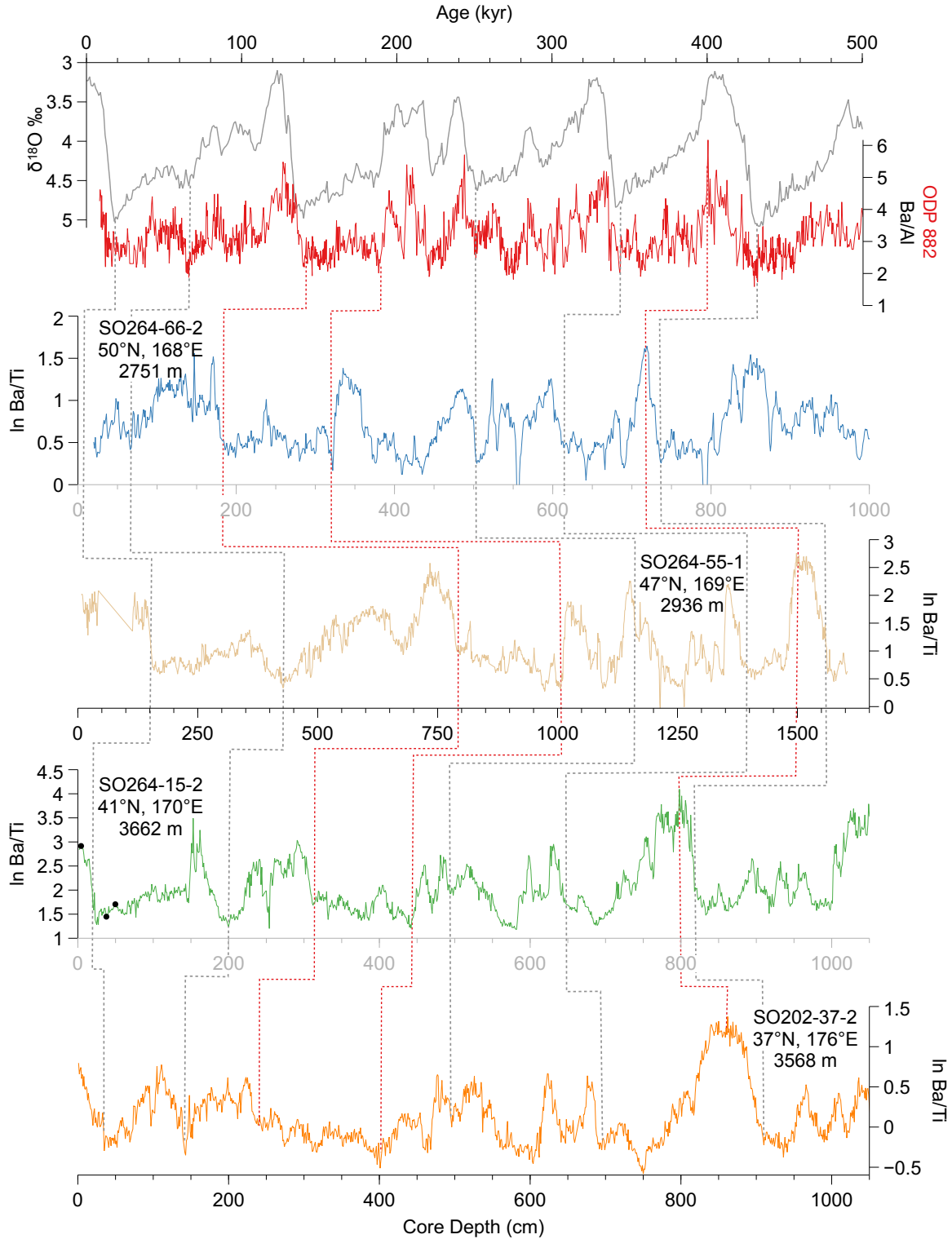


Figure 4. Stratigraphic framework of sediment cores from the Northwest Pacific and correlation with high-resolution XRF data to the benthic  $\delta^{18}\text{O}$  stack of Lisiecki and Raymo (2005) and the stratigraphic established record site 882. The stratigraphy is based on the comparison between the benthic  $\delta^{18}\text{O}$  stack and XRF Ba-normalized ratio. Gray stippled lines indicate correlation points to the benthic  $\delta^{18}\text{O}$  stack and the sediment cores. Red stippled lines indicate correlation points to the site 882 record and the sediment cores. Blank spots mark the AMS  $^{14}\text{C}$  dating control points for core SO202-37-2.

To establish a coherent chronostratigraphic framework for all cores along our meridional transect, we used an iterative approach combining various XRF-based chemostratigraphic

correlation patterns indicative of orbital-scale primary production and dust transport changes, anchored by oxygen isotope stratigraphy, AMS  $^{14}\text{C}$  ages, tephra identification and supported by information from paleomagnetic measurements on neighboring abyssal cores (Wang et al., 2021b).

Our In-Ba/Ti records show a pronounced characteristic following glacial-interglacial changes, as known from ODP Site 882, piston core MD01-2416 and other regional records (Gebhardt et al., 2008; Nürnberg and Tiedemann, 2004; Wang et al., 2021b). We correlated our In-Ba/Ti records to both the global benthic  $\delta^{18}\text{O}$  stack of Lisiecki and Raymo (2005) and ODP site 882 Ba/Al (Jaccard et al., 2010) to establish an initial age model for the studied cores, with the assumption that higher values represent interglacials and lower values glacials (Figure 2). While this correlation pattern is less clear towards the south, especially during MIS 5, we refined the age model by correlating well-defined interglacial Ca peaks to Site 882 (Figure S1).

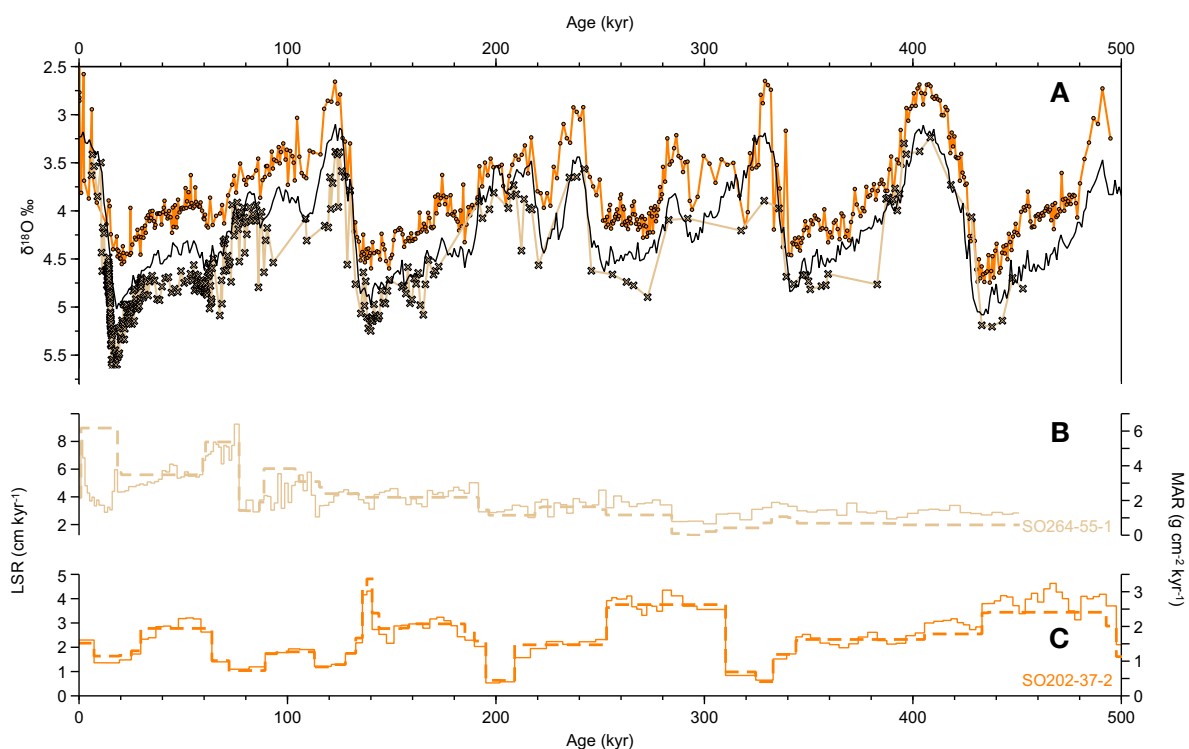


Figure 5. (A) Benthic  $\delta^{18}\text{O}$  records from the Northwest Pacific cores SO264-55-1 (light brown line) and SO202-37-2 (orange line, measured on *C. wuellerstorfi*) compared to the global benthic  $\delta^{18}\text{O}$  stack (Lisiecki and Raymo, 2005) in black line. (B) Linear sedimentation rates (LSR, dashed lines) and mass accumulation rates (MAR, solid lines) of core SO264-55-1 and SO202-37-2 plotted against age.

To develop independence from this initial XRF-based age model, we correlated the benthic *C. wuellerstorfi*  $\delta^{18}\text{O}$  of SO202-37-2 and composite benthic  $\delta^{18}\text{O}$  of SO264-55-1 to the benthic  $\delta^{18}\text{O}$  stack (Figure 3A). The results provide an excellent agreement between the isotope



stratigraphy and the initial XRF-based age models of these two cores (Figure S1), with maximum offsets never exceeding  $\sim 2$  ka between our isotope stratigraphy and the XRF-based age model.

All age-depth tie points were primarily selected at climatic transitions (Table S2), the resulting calculated linear sedimentation rates (LSR) and MAR (Figure 3B and C) show variations starting from Termination II, in particular in core SO264-55-2, while core SO202-37-2 shows relatively high values during glacials. Overall, LSRs and MARs are higher above the Subarctic Front (SO264-55-2) than below (SO202-37-2).

## **4.5. Results and discussion**

In the following, we examine biological export production ( $\ln$ -Ba/Ti), carbonate content and accumulation rates, and dust-related (XRF-Fe) variations of four sediment cores from the western subarctic Pacific during the last 500 ka BP, with the aim of better understanding productivity variations in the Pacific and its relation to the marine carbonate and carbon cycle.

### **4.5.1. NW Pacific glacial-interglacial productivity variations and their forcing factors over the last 500 ka**

As corroborated from the adjacent ODP Site 882, XRF-based Ba-normalized ratios have an excellent correlation with biogenic barite (Jaccard et al., 2009) and therefore, we took  $\ln$ -Ba/Ti as an indicator for past changes in biological export production. The  $\ln$ -Ba/Ti ratios from all four sediment cores show strong orbital-scale variations, with generally higher productivity during interglacials and lower during glacials, though some maxima occur also during glacial MIS 8 and 12 (Figure 4C to F), notably as well in ODP Site 882. The amplitude of variations between glacials and interglacials decreases towards the south, and according values differ from ca. 4 down to less than 1 in  $\ln$  (Ba/Ti) (Figure 4C to F). Notably, MIS 11 as the longest interglacial interval of the last 500 ka is well characterized in all records by a broad-scale productivity peak (also in  $\ln$ -Ca/Ti, see Figure S1). However, the similarly warmer-than-present interglacial MIS 5 does not yield a similarly distinct peak feature. Fe counts, considered mostly as an indicator of dust input (e.g. Martínez-García et al., 2011), generally show an anti-correlation with the other proxies, with higher values during glacials and lower during interglacials (Figure 4G). The amplitude also decreases towards the south from ca.  $3 \times 10^5$  to  $0.9 \times 10^5$  counts per second (cps) in respective maxima.

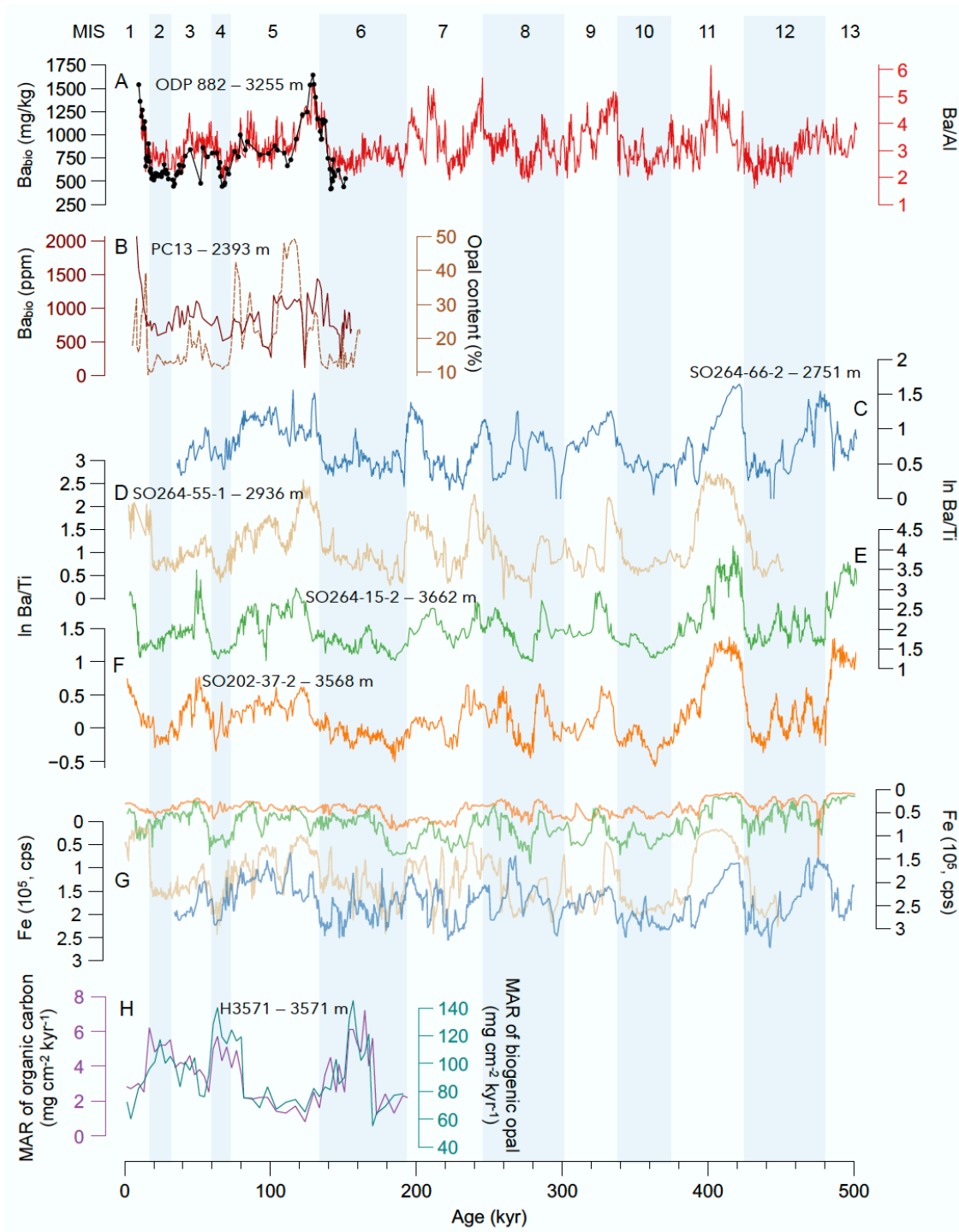


Figure 4. Multiproxy productivity records from the Northwest Pacific in order from north to south. (A) Biogenic barium ( $Ba_{Bio}$ ) (black) and XRF  $Ba/Al$  (red) from ODP site 882 (Jaccard et al., 2010; Jaccard et al., 2009). (B)  $Ba_{Bio}$  (reddish brown) and opal content (brown) from PC13 (Brunelle et al., 2010). (C)-(F) XRF  $ln-Ba/Ti$  of the study cores (this study). (G) XRF  $Fe$  counts of the study cores plotted with inverted y-axis (this study). (H) fluxes of organic carbon (purple) and biogenic opal (dark-cyan) from H3571 (Kawahata et al., 2000).

The productivity pattern observed in our  $ln-Ba/Ti$  results aligns with previous studies in the subarctic NW Pacific (Costa et al., 2018; Galbraith et al., 2008; Iwasaki et al., 2012; Jaccard et al., 2010; Kohfeld and Chase, 2011; Shigemitsu et al., 2007). However, our records extend the southern boundary of this glacial-interglacial pattern first identified in the subarctic domain

(Galbraith et al., 2008; Jaccard et al., 2010) further south, across the Subarctic Boundary and the Kuroshio Bifurcation Front into the Mixed Water Region. In the following, we evaluate potential control mechanisms that lead to the observed distribution of export production patterns in the NW Pacific and their underlying forcing.

#### **4.5.1.1. Iron micronutrient supply by aeolian or marine lateral transport**

Today, iron supply – as a key micronutrient for phytoplankton growth – limits primary production in the modern subarctic Pacific, parts of the equatorial Pacific, and the Southern Ocean (Boyd et al., 2007). A higher iron-containing dust flux can thus promote nitrogen fixation and therefore increase the nitrate pool, thereby increasing biological export production. Numerous records have shown a higher aeolian flux, sourced from East Asian desert regions, into the North Pacific during glacials (Hovan et al., 1991; Jacobel et al., 2017; Kawahata et al., 2000; Serno et al., 2017; Shigemitsu et al., 2007). An additional possible micronutrient source would be dust-borne iron accumulating on sea ice and icebergs, which would have been subsequently transported along the main current trajectories, ultimately delivered to the surface ocean while melting. Enhanced flux of Ice-rafted debris (IRD) occurred near the onset of terminations in the NW Pacific (Gebhardt et al., 2008) and IRD were found from further south at the Shatsky Rise (McCarron et al., 2021) and also in our N-S transect records. However, this type of supply would be likely more episodic, and quickly removed from surface waters instead of being maintained over several thousand years.

However, recent studies from the Equatorial Pacific have demonstrated that there is no significant relationship between the efficiency of the biological pump and dust input (Costa et al., 2016; Jacobel et al., 2019; Kienast et al., 2004; Shigemitsu et al., 2007; Winckler et al., 2016). Although the subtropical to subpolar NW Pacific exhibits a different nutrient regime, the observed higher interglacial productivity signal throughout our NW Pacific N-S transect shows an anti-correlation to higher dust supply during glacials (Figure 4C to G). Thus, increased aeolian iron delivery during glacials alone does not seem to constitute the major influence on controlling North Pacific productivity.

#### **4.5.1.2. Influence of ocean gyre circulation – high vs. low-latitude forcing**

In comparison with records above the Subarctic Front including ODP Site 882, the amplitudes of In-Ba/Ti variations in our southern studied cores are apparently much lower and look less similar to global climate change patterns, as e.g., expressed in the benthic  $\delta^{18}\text{O}$  stack

(Figure 4C to F and Figure S1). One possibility to explain the increasingly subdued glacial-interglacial productivity pattern towards the south could realistically be a regionally pronounced, meridional shift between the subarctic and subtropical gyres. This would also relocate both the Mixed Water Region and its boundary between the Subarctic and the Subtropical Front, driven by the respective current energy and strength of the Kuroshio Extension and the Oyashio Current. At present, the primary productivity in the transition zone is strongly influenced by the relative positions of these two currents (Kawahata and Ohshima, 2002). Pollen and benthic foraminiferal fauna studies have shown that a small southward shift of the Kuroshio Extension and/or the Subarctic Front during glacials (Kawahata and Ohshima, 2002; Ohkushi et al., 2018), supported by the decreasing amplitude of iron dust-related records from north to south in our records (Figure 4G).

However, the neighboring core H3571 from Hess Rise suggests higher productivity during glacial periods (Figure 4H), indicated by higher biogenic opal and organic carbon burial in the sediments (Kawahata et al., 2000). Also, foraminiferal abundance records from Shatsky Rise reflect high productivity during glacial periods, correlating to biogenic opal and organic carbon (Ohkushi et al., 2018). These opposite productivity signals might also simply be showing that preservation is not necessarily equivalent to initial component fluxes, as e.g., organic carbon is sensitive to oxygenation of bottom and pore waters. Its preservation also decreases along with increasing oxygen exposure time (Hartnett et al., 1998). Compiled data from the North Pacific showed that organic carbon flux was generally lower during the Last Glacial Maximum in comparison to the Holocene (Kohfeld and Chase, 2011). Additionally, an inverse glacial-interglacial productivity condition occurred in latitudes below 40°N (Rae et al., 2020). These observed opposite productivity signals at Hess Rise might also support that gyre shifts of the cold nutrient-rich Oyashio Current and the warm nutrient-poor Kuroshio Current, as a transition zone, provided different nutrient regimes to the transitional region in our study area. Although it has been discussed and proposed previously that export production peaked during or towards glacial terminations in the subarctic Pacific (Crusius et al., 2004; Gebhardt et al., 2008; Kawahata et al., 2000; Ohkushi et al., 2018), we suggest the maximum export production persisted during the peak interglacial periods reflected by maximum in biogenic Ba records from the Emperor Seamount Chain and the Hess Rise. Based on our result, this condition extended further south to the Hess Rise at 37°N as the end member of the northern-dominated nutrient regime in the NW Pacific.

#### 4.5.1.3. Macronutrient supply and limitation through upper ocean stratification changes

Export production is generally higher during interglacials and lower in glacials (Figure 4). However, sedimentary, foraminifera- and diatom-bound nitrogen isotopes ( $\delta^{15}\text{N}$ ) as proxy for the nutrient utilization efficiency revealed that the nutrient utilization enhanced during glacial periods in the subarctic Pacific (Brunelle et al., 2007; Galbraith et al., 2008; Knudson and Ravelo, 2015a; Ren et al., 2015). A common physical mechanism has been proposed to modulate the nutrient supply: by increasing stratification during glacials, the nutrient-rich deep water was then more isolated from surface waters, thereby leading to nearly complete nutrient utilization (Brunelle et al., 2007; Brunelle et al., 2010; Costa et al., 2018; Gebhardt et al., 2008; Jaccard et al., 2010; Jaccard et al., 2005; Kienast et al., 2004; Knudson and Ravelo, 2015a; Sigman et al., 2004). IRD has been found in the NW Pacific sediments and recently published studies extended the lateral coverage further south to the northern Shatsky Rise at 38°N (Kotilainen and Shackleton, 1995; McCarron et al., 2021). We have also qualitatively observed IRD grains in the coarse fractions in all four sites during glacial intervals. Evidence for increased glacial sea ice formation in the subpolar NW Pacific (e.g. Max et al., 2012b; Méheust et al., 2018; Méheust et al., 2016), which is mechanistically connected to the closure of the Bering Sea acting as positive feedback mechanism (Knudson and Ravelo, 2015b), further supports this scenario by freshening surface waters and decreasing salinity. As a result, upper ocean stratification during glacials was likely enhanced (Costa et al., 2018). Therefore, when vertical water mass mixing increased during interglacials, nutrients would be more vigorously upwelled into the surface ocean and result in enhanced productivity.

This pattern would be in line with previous suggestions that invoked a differential nutrient signature in mid-depth waters both on instrumental time scales (Nishioka et al., 2014; Nishioka et al., 2020; Wong et al., 2022), and on glacial-interglacial changes and glacial terminations (Lembke-Jene et al., 2017; Max et al., 2014b; Ovsepyan et al., 2017). Under these assumptions, a more extensive glacial NPIW is better ventilated and occupies an increased depth domain down to ca. 1500-2000 m water depth (Gong et al., 2019; Herguera et al., 2010; Jaccard and Galbraith, 2013). These mid-depth waters were nutrient poorer than their modern equivalents, while a more isolated glacial NPDW was enriched in nutrients, thus leading to a lower preformed nutrient pool that is subjected to winter upwelling and thermocline replenishment (Gong et al., 2019; Lembke-Jene et al., 2017). These macro-nutrient supply changes via surface

ocean stratification combined with different configurations of the deep preformed nutrient pool could hence constitute one of the primary controls on export production changes in the NW Pacific.

## **4.5.2. NW Pacific variations in carbonate production and preservation**

### **4.5.2.1. Quantification of XRF-derived Calcium data for high-resolution carbonate time-series**

In order to obtain records of sufficiently high temporal resolution, we used XRF-scanning-derived Ca data which has been proposed to reflect the CaCO<sub>3</sub> variations in marine sediments. Many studies have used and provided evidences that XRF-based Ca-normalized ratios can be used as indicator of the carbonate saturation state of the deep ocean (e.g., Gottschalk et al., 2018; Jaccard et al., 2010). We compared the XRF-Ca counts and the CaCO<sub>3</sub> content and it presented high correlation coefficients in all four studied cores (SO264-66-2:  $Y = 7358.3X + 40105$ ,  $r^2 = 0.8742$ , SO264-55-1:  $Y = 8312.7X + 28955$ ,  $r^2 = 0.8171$ , SO264-15-2:  $Y = 15154X - 138732$ ,  $r^2 = 0.8293$ , SO202-37-2:  $Y = 11080X - 137077$ ,  $r^2 = 0.8986$ ; Figure 5), indicating that our XRF-Ca ratio data faithfully represents CaCO<sub>3</sub> content variations in the study area.

On the basis of CaCO<sub>3</sub> content being potentially affected by dilution with biogenic material such as opal, and terrigenous components such as tephra, ice-rafted detritus and dust, we then calculated carbonate accumulation rates (CAR, g/cm<sup>2</sup>ka<sup>-1</sup>) to mitigate these effects to some extent. The converted CAR records thus provide a more comprehensive picture of the carbonate sedimentation regime than solely CaCO<sub>3</sub> content.

For the northern Emperor Seamount Chain cores SO264-66-2 and SO264-55-2, the CARs track the patterns of CaCO<sub>3</sub> content very closely, indicating better carbonate preservation during interglacials and higher dissolution in glacials (Figure 6B and C). As recorded in the regional reference core ODP site 882 (Jaccard et al., 2010), one prominent feature are interglacial carbonate peaks followed by carbonate-free sediments in the northern sites (Figure 6A). The cores SO264-66-2 and SO264-55-2 clearly repeat this feature; the CaCO<sub>3</sub> content maxima appeared during interglacial MIS 1, 3, 5, 7, 9 and 11 up to 95-40 % and then dropped to 10-0 % during most of the glacials and even in some of the late interglacials, such as MIS 9 and 11 (Figure 6B and C).

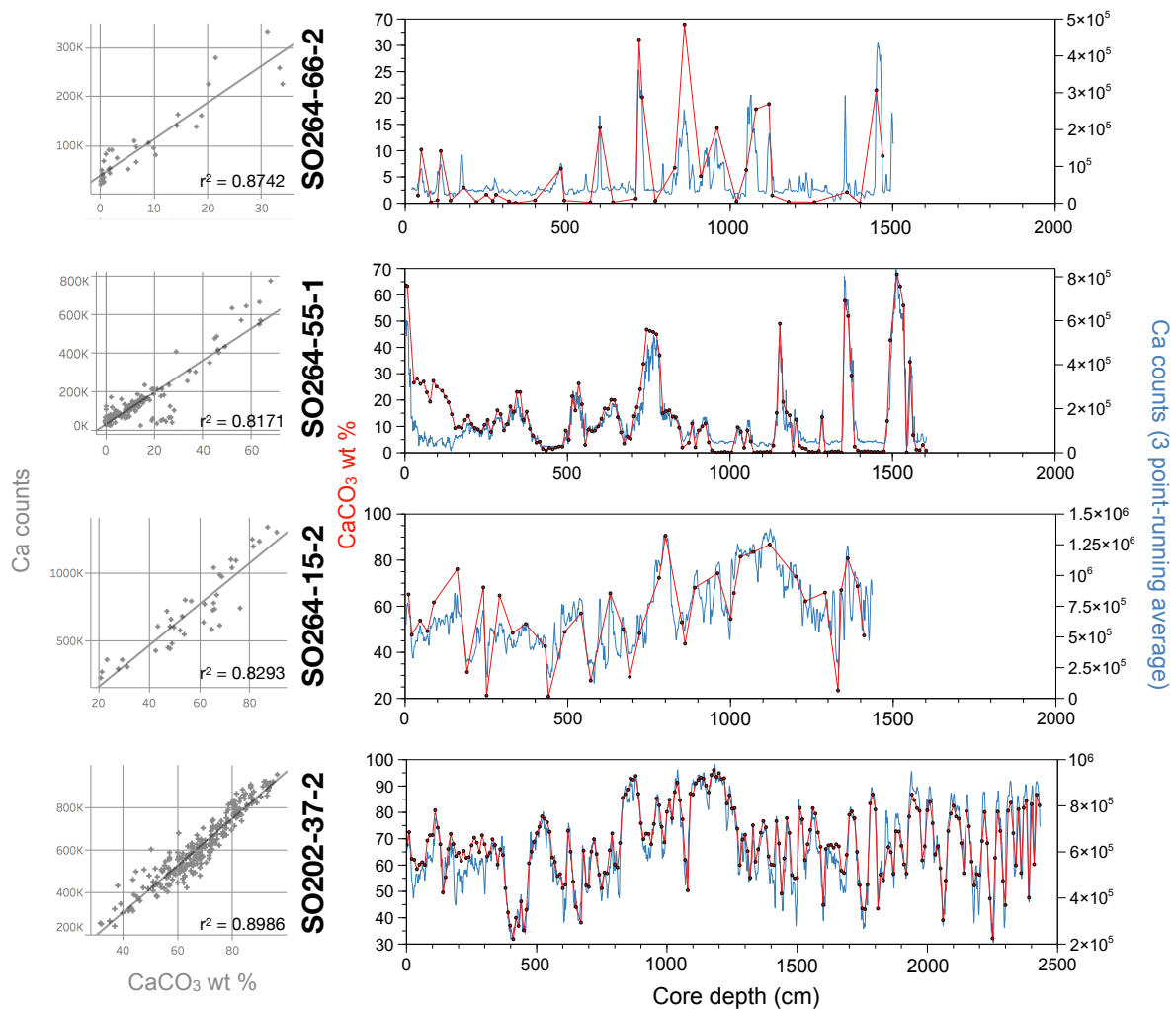


Figure 5. Comparison of downcore variations of carbonate content in weight percent (red lines) and smoothed (3 point-running average) XRF-Ca counts (blue lines) of four cores from the Northwest Pacific (right panels), shown against individual core depths (noted scale change in the lower most right panel). The four left panels show correlation between  $\text{CaCO}_3$  content and XRF-Ca counts and the corresponding linear regression lines with the resulting correlation coefficient  $r^2$ .

The southern Emperor Seamount Chain cores SO264-15-2 and SO202-37-2, however, do not record similar carbonate peak structures. The  $\text{CaCO}_3$  contents of these two cores are nearly identical and show significant variations (Figure 6D and E).  $\text{CaCO}_3$  contents rise in glacial periods, except the sustained preservation during MIS 5 and the early MIS 11 and 9. In addition, a continued period of carbonate dissolution began roughly 500 ka BP and lasted around 200 ka. While the two southern sites SO264-15-2 and SO202-37-2 show some comparable trends between CAR and  $\text{CaCO}_3$  content, they yield differences, most notably during MIS 5, early MIS 7 and MIS 9 (Figure 6D and E). CAR variations reveal a clearer pattern than  $\text{CaCO}_3$  content does, e.g., throughout the CAR profile of SO202-37-2, a  $\sim 100$  ka cyclic pattern, indicative of orbital forcing-induced changes in carbonate production or preservation, emerges

with higher values during glacial, and relatively lower values in interglacial periods, except the last 60 ka BP, where this relationship switches.

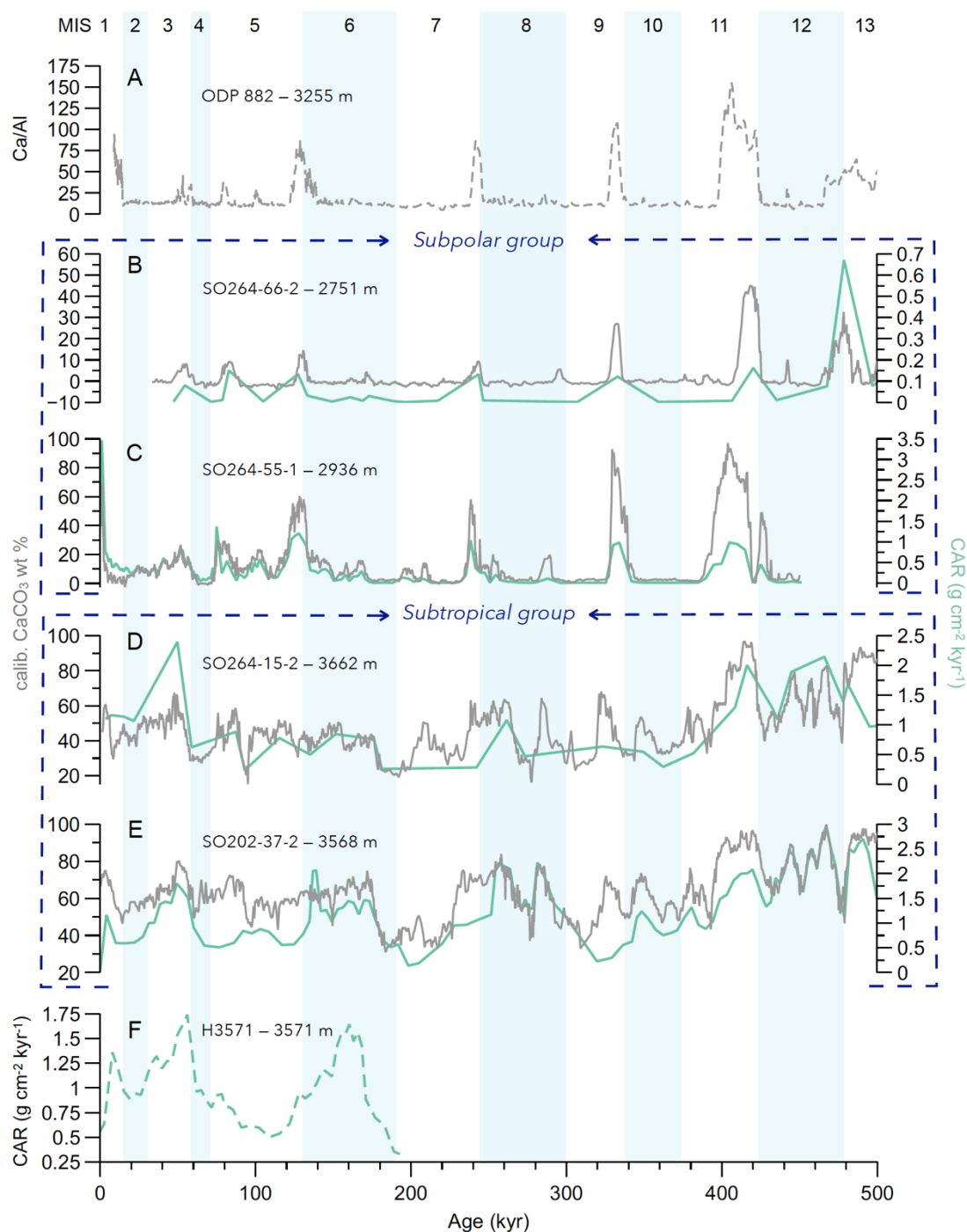


Figure 6. Comparison of carbonate variations along the NW Pacific transect, based on XRF-derived Ca/Al, calibrated carbonate content (gray, in wt. %) and carbonate accumulation rate (light green, in  $\text{g}/\text{cm}^2\text{kyr}^{-1}$ ) from (A) ODP site 882 (Jaccard et al., 2010), (B) SO264-66-2 (this study), (C) SO264-55-1 (this study), (D) SO264-15-2 (this study), (E) SO202-37-2 (this study) and (F) H3571 (Kawahata et al., 2000). Due to the differences of the carbonate patterns, the studied cores (B) and (C) are grouped as “Subpolar group”, while (D) and (E) as “Subtropical group”.

Due to the observed  $\text{CaCO}_3$  content and CAR differences, we grouped and named the NW Pacific cores from the northern Emperor Seamount Chain SO264-64-1 and SO264-55-1 as



“Subpolar group”, and the southern cores SO264-15-2 and SO202-37-2 as “Subtropical group” (Figure 6). We determined SO264-55-1 as representative core for the Subpolar group and SO202-37-2 for the Subtropical group due to their higher resolutions.

#### **4.5.2.2. Latitudinal dynamics between export production and carbonate depositional patterns**

In our Subtropical Group, the relation between paleo-export production, as represented in In-Ba/Ti ratios, and CaCO<sub>3</sub> content and/or accumulation rates is not straightforward. Maxima between the two proxies are most significant between late MIS 13 to MIS 9, but their respective amplitude expressions are different (Figure 7-Subtropical group). This period of broad CAR decline roughly fits into the period of the so-called Mid-Brunhes Dissolution Interval (MBDI), which has been identified throughout individual sites in different regions of the world ocean (Sexton and Barker, 2012). The MBDI was hypothesized to be due to a global proliferation of the *Gephyrocapsa* coccolithophore, causing the increase of ocean surface carbonate production and driving enhanced deep-sea carbonate dissolution (Barker et al., 2006). From MIS 8 onward, CAR patterns changed to a more pronounced glacial-interglacial timing, less consistent with CaCO<sub>3</sub> content variations (Figure 7-Subtropical Group). An earlier study of calcareous nanofossils on Shatsky Rise also showed a significant shift between MIS 8 and 7, and the bulk CaCO<sub>3</sub> content switching from coccolith calcite to foraminifera with co-occurring biogenic opal, which could have been favored by iron fertilization via aeolian dust increase (Bordiga et al., 2014). This might explain the mismatch between the CaCO<sub>3</sub> content and CAR being due to dilution by biogenic opal.

Overall, the carbonate records in the Subtropical Group are evidently recording a pattern reminiscent of the “Pacific-type” with enhanced CaCO<sub>3</sub> preservation during glacials, similar to NE and equatorial Pacific records (Figure 5D to F; e.g., Farrell and Prell, 1989; Karlin et al., 1992; Wu et al., 1991). Earlier studies based on data of Equatorial Pacific sediment cores suggested that Pacific glacial-interglacial carbonate preservation cycles are mainly controlled by dissolution through calcite lysocline fluctuations (Farrell and Prell, 1989; Wu et al., 1991). It is mostly assumed that the underlying forcing of these lysocline and CCD adjustments reflect a buffering of the deep-sea [CO<sub>3</sub><sup>2-</sup>], which controls the Pacific carbonate accumulation patterns (Anderson et al., 2008; Farrell and Prell, 1989; Hodell et al., 2001; Zhang et al., 2007). Sexton and Barker (2012) attributed the cause of the glacial Pacific CaCO<sub>3</sub> dissolution minimum to a consistently strengthened ventilation within the Pacific sector of the Southern Ocean, referred

to as “glacial Pacific ventilation hypothesis”. In addition, in the primary productivity-related “rain ratio hypothesis” (Archer and Maier-Reimer, 1994), changes in the relative ratio of organic carbon vs.  $\text{CaCO}_3$  are thought to indicate change in ocean pH [ $\text{CO}_3^{2-}$ ] due to the degradation of organic carbon, which promotes carbonate dissolution in the sediments.

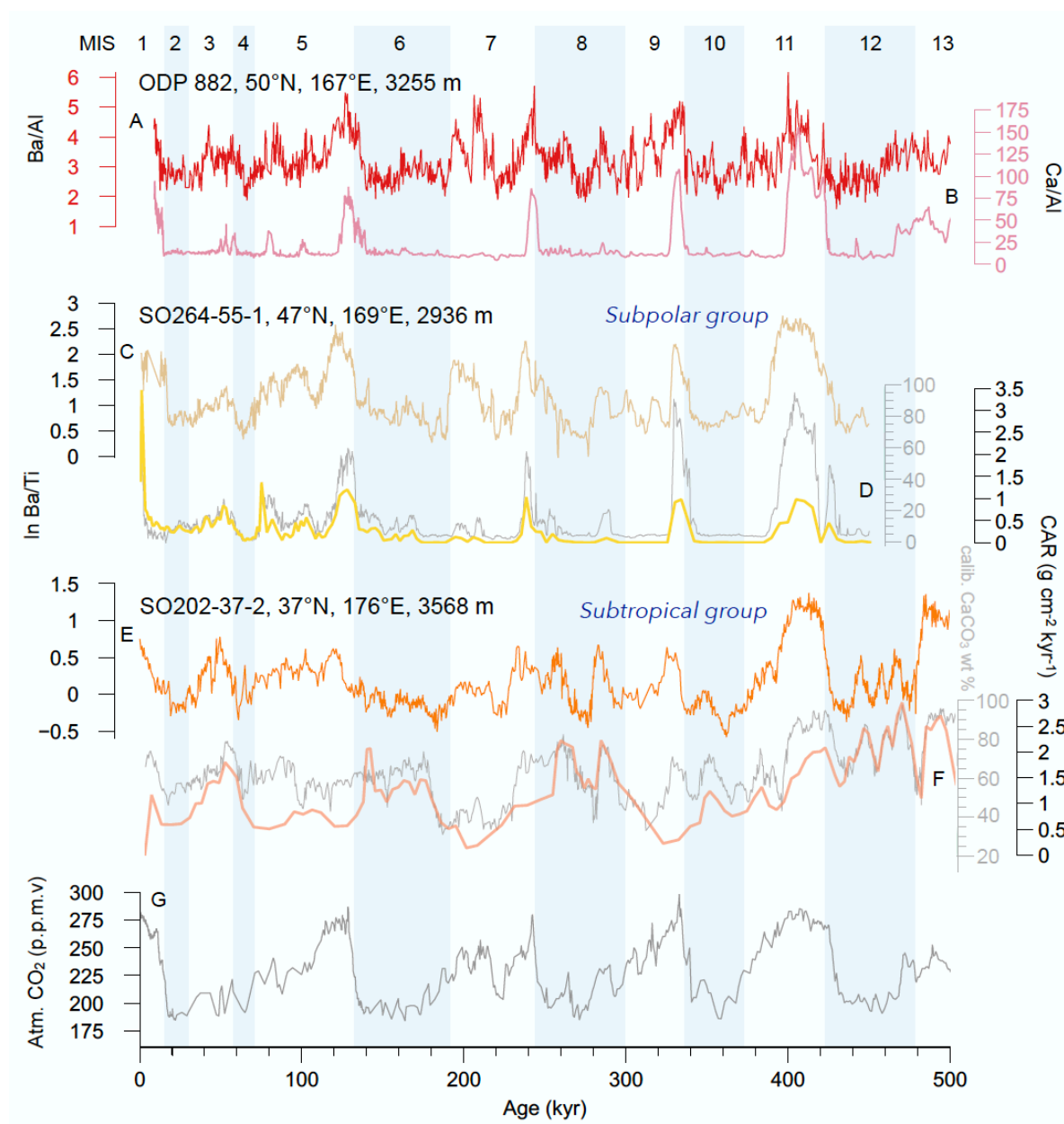


Figure 7. Comparison of productivity and carbonate records from the study region along the latitudinal transect for the last 500,000 years. (A)-(B) XRF Ba/Al and Ca/Al ratios from ODP Site 882. (C)-(D) XRF ln-Ba/Ti, CAR and ln-Ca/Ti (in gray) from SO264-55-1 as a representative core from the “Subpolar group”. (E)-(F) XRF ln-Ba/Ti, CAR and ln-Ca/Ti (in gray) from SO202-37-2 as a representative core from the “Subtropical group”. (G) Atmospheric  $\text{CO}_2$  concentration from Antarctic ice core EPICA Dome C (EDC Lüthi et al., 2008; Monnin et al., 2001; Siegenthaler et al., 2005).

In contrast, in the Subpolar group, severe carbonate dissolution dominates throughout all glacials during the last 500 ka BP. Nearly no carbonate was preserved, even extending into to some mid- and late-interglacials. However, the interglacial productivity and carbonate signals

are relatively straightforward (Figure 7-Subpolar group). In almost all interglacials, i.e., MIS 11, 9, 7e, 5e, 5c and 5a, corresponding CaCO<sub>3</sub> content and CAR peaks correlate with productivity maxima. Thus, in the Subpolar group, no “Pacific-type” CaCO<sub>3</sub> can be observed, instead an overall carbonate-corrosive, but distinct “Atlantic-type”, featuring severe CaCO<sub>3</sub> dissolution during glacials seems to prevail throughout the investigated 500 ka BP. The “Atlantic-type” CaCO<sub>3</sub> preservation originally mainly results from changes in the strength of the Atlantic Meridional Overturning Circulation (AMOC), and the extent and distribution of well-ventilated North Atlantic Deep Water (NADW; Broecker and Clark, 2001; Hodell et al., 2001). However, the higher [CO<sub>3</sub><sup>2-</sup>] in NADW causes the CCD to be located relatively deeper (~5000 m) in the Atlantic basin relative to the Pacific (~3500 - 4500 m).

Transient carbonate peaks as seen in the Subpolar group have also been observed in the biogenic carbonate (indicated by Ca/Al ratios) of neighboring site ODP Site 882 (Jaccard et al., 2010). Notably, even relatively shallow mesopelagic records from the marginal seas also show similar CaCO<sub>3</sub> pattern with rapid interglacial peaks and nearly absent CaCO<sub>3</sub> content during glacial periods (Brunelle et al., 2010; Iwasaki et al., 2012). The CaCO<sub>3</sub> content disparity between the glacial and the interglacial sediments from the Subarctic group is substantial (Figure 6B and C). The peak-interglacial carbonate peaks, followed by near absence of carbonate in the glacial sediments suggest that the Subpolar group sites were always bathed in waters below the CCD during most of the glacials and even part of the late interglacial periods, with intermittent rapid shallowing. The rapid decline of CaCO<sub>3</sub> content in the Subpolar group indicates a fast shallowing of the lysocline which leads to an increased alkalinity and therefore reduced *p*CO<sub>2</sub> in the surface ocean.

In the “carbonate compensation hypothesis”, the deep ocean carbonate chemistry called for changes in increasing [CO<sub>3</sub><sup>2-</sup>] and following increasing alkalinity, when CO<sub>2</sub> was released back to the surface ocean (and the atmosphere) at the end of glacials. Such ventilation changes and CO<sub>2</sub> outgassing cause a transient carbonate compensation in order to buffer and balance the saturation state, leading to preservation of CaCO<sub>3</sub> in response to the deep ocean carbon storage changes (Boyle, 1988; Broecker and Peng, 1989; Marchitto et al., 2005). Other studies also suggested these interglacial carbonate peaks could imply high loading of regenerated dissolved inorganic carbon and therefore a short-term of major CO<sub>2</sub> release from the deep subarctic North Pacific, due to ventilation from the south and/or local bottom water ventilation (Gebhardt et al., 2008; Jaccard et al., 2010).

We finally added to our datasets a further examination of the relation between productivity and carbonate preservation on a shorter time scale, covering the last 200 ka BP. By adding alkenone concentrations and coarse fraction percent (>63 $\mu\text{m}$ , sand %) data to our data set (Figure 8), we attempted to qualitatively assess whether carbonate preservation changes in both or either the Subpolar and Subtropical groups are mostly associated with carbonate (coccolithophore) production or carbonate dissolution.

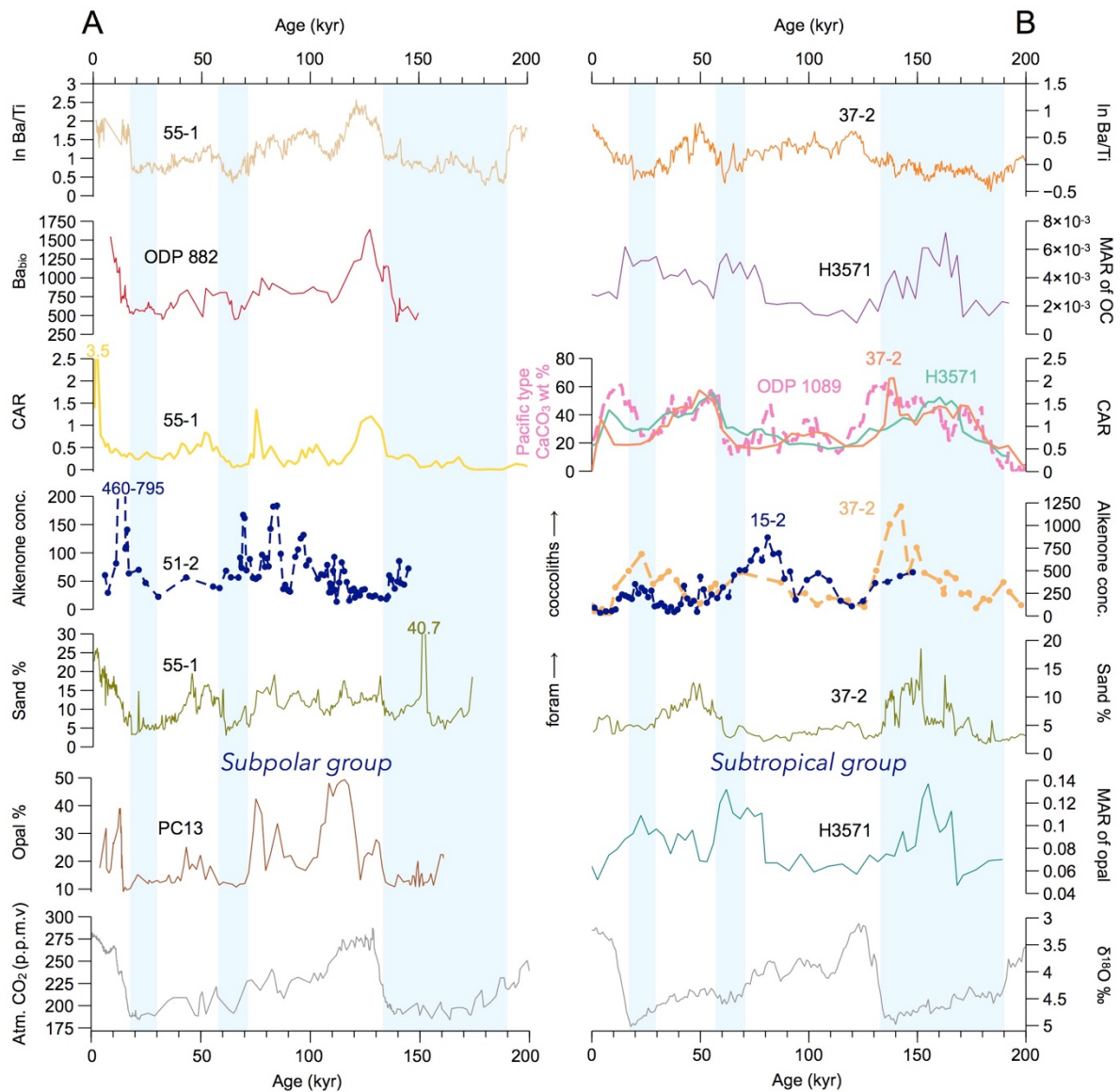


Figure 8. Comparison of multiproxy records from Subpolar group (column A) and Subtropical group (column B) for the last 200,000 years. The lowest panels show the EDC  $\text{CO}_2$  concentration (EDC Lüthi et al., 2008; Monnin et al., 2001; Siegenthaler et al., 2005) and the benthic  $\delta^{18}\text{O}$  stack (Lisiecki and Raymo, 2005).

In the Subpolar group, the coherent increase in biogenic Ba and other biogenic proxies across the region suggests enhances organic carbon export, which led to an increase in carbonate production and according carbonate flux maxima during interglacials (Jaccard et al.,

2009; Kohfeld and Chase, 2011). Alkenone concentration of SO264-51-2 (Figure 8A 51-2) shows a likewise increase in MIS 5, indicating higher coccolithophore production contributed to maximum carbonate accumulation. In addition, the high coarse fraction content shows a dominance of foraminifera and hence low dissolution intensity of coarse carbonate particles. The relative high values of the sand fraction (sand %) in interglacials further support a productivity-related rather than dissolution-dominated carbonate regime (Figure 8A). Unfortunately, our results cannot provide direct information about whether this interglacial inorganic carbon pattern was related to prior CO<sub>2</sub> release from the deep subarctic NW Pacific, which might be attributed to re-invigorated ventilation from the south and/or of local bottom water (Gebhardt et al., 2008; Jaccard et al., 2010). Clearly, further studies on benthic foraminiferal carbon isotopes and [CO<sub>3</sub><sup>2-</sup>] from this region would be necessary to resolve this question.

Notably, in the Subtropical group the export production signal and carbonate flux, e.g., in SO202-37-2, pace largely out of phase for the last 300 ka BP, except for a few local maxima in MIS 3 and 8, where both productivity and carbonate flux increased (Figure 7-Subtropical group). Otherwise, the carbonate patterns are expressed as glacial-interglacial cycles, with higher preservation during glacials and dissolution during interglacials, while ln-Ba/Ti variations were relatively higher during interglacials. The poor correlation between productivity and CaCO<sub>3</sub> has also been known from some other sites from the equatorial Pacific (Anderson et al., 2008; Qin et al., 2017; Zhang et al., 2007). On the other hand, considering that the ODP site 1089 (40.94°S, 9.89°E; 4624 cm water depth) is bathed in the LCDW and reflects high-resolution [CO<sub>3</sub><sup>2-</sup>] changes in deep Pacific, the good correlation to the carbonate records from the Hess Rise suggested that the typical “Pacific-type” CaCO<sub>3</sub> pattern prevails in particular for this period of the last 200-300 ka BP. Moreover, the sand% in the Subtropical group shows a clear indication for a dissolution signal during MIS 5 (Figure 8B, 37-2 olive green line), and while the alkenone concentration remained high (Figure 8B, 15-2), this can be explained by coccoliths being more resistant to dissolution than foraminifera (Chiu and Broecker, 2008). The mismatch between export production and carbonate records from the Hess Rise not only could be explained by the possibility of CaCO<sub>3</sub> production varying independently of organic carbon export, but also reveal the boundary shifts between the subarctic and subtropical gyre, which provide different nutrient regimes to the region. These large reorganizations of the carbonate depositional regime and underlying ecological changes or boundary conditions around 280-300 ka BP were ultimately possibly linked to changes in

low-latitude climate forcing and long-term ENSO activity and Asian Monsoon changes (Beaufort et al., 2022; Bordiga et al., 2013).

#### **4.6. Conclusions**

Our sediment sites from the Emperor Seamount Chain and the Hess Rise showed a decreasing gradient in paleo-export production based on XRF-derived In-Ba/Ti ratios and dust supply (XRF-Fe), reconstructed from records from the subarctic north at 52°N to the transitional-subtropical south at around 37°N. Maxima in biogenic Ba records suggested the maximum export production took place during the peak interglacial periods in the NW Pacific during the last 500 ka. We conclude that the local subarctic and subtropical gyre circulation shift and the upper ocean stratification had the major control on the nutrient regime, rather than dust supply. Additionally, a reverse pattern in carbonate content and preserved flux occurred along the Emperor Seamount Chain. In our Subpolar group, the productivity had a more direct influence on the carbonate system in the western Subarctic Pacific. The coherent increases in biogenic Ba, CAR, alkenone concentration, sand% and opal% during interglacials indicating a regional surface biological production promoted these interglacial carbonate peaks in this carbonate-corrosive region. On the other hand, the Subtropical group carbonate deposition attributed to the dissolution which supported by the comparable patterns between sand% and CAR. The CAR semblance to the LCDW carbonate signal suggested this carbonate pattern is related to the deep Pacific  $[\text{CO}_3^{2-}]$  changes responding to the global ocean carbonate budget balance. The mismatch between export production and carbonate records from the Hess Rise also revealed the boundary of the shifting between the cold nutrient-rich Oyashio Current and the warm nutrient-poor Kuroshio Current which provide different nutrient regime to the region.

#### **4.7. Authors' contributions**

WSC, LLJ and RT designed study, WSC, LJ and GK carried out XRF-scanning. WSC, LL, and LLJ measured stable isotopes, BN provided alkenone data, WSC, LLJ, RT, LL and BN developed age model, WSC, LLJ and LJ analyzed data. WSC and LLJ wrote the manuscript, with input from all co-authors. All authors discussed the data and contributed to the final manuscript version.

## 4.8. Acknowledgements

We thank the master, crew and the SO264 science party for their contributions to a successful expedition. We thank Valea Schumacher, Susanne Wiebe for technical support, and Lisa Schoenborn, and Dorothee Wilhelms-Dick for analytical support with the IRMS. We thank Tunde Gabriel for support in sample processing. We acknowledge financial support from the AWI institutional budget under the “PACES-II” (2018-20) and “Changing Earth – Sustaining our Future” (2020-2022), the German Federal Ministry for Education and Research (BMBF) through grants no. 03G0264B “SO264-EMPEROR” and 3F0785A “NOPAWAC”.

## 4.9. Data Availability

The datasets used and analyzed during this study are available on Pangaea and/or from the corresponding author or project PI on reasonable request.

## 4.10. References

- Anderson, R., Fleisher, M., Lao, Y. and Winckler, G., 2008. Modern CaCO<sub>3</sub> preservation in equatorial Pacific sediments in the context of late-Pleistocene glacial cycles. *Marine Chemistry*, 111(1-2): 30-46.
- Archer, D. and Maier-Reimer, E., 1994. Effect of deep-sea sedimentary calcite preservation on atmospheric CO<sub>2</sub> concentration. *Nature*, 367(6460): 260-263.
- Arrhenius, G., 1952. Sediment cores from the East Pacific. *Reports of the Swedish deep-sea expedition, 1947-1948*, 5: 201.
- Auderset, A., Schmitt, M. and Martínez-García, A., 2020. Simultaneous extraction and chromatographic separation of n-alkanes and alkenones from glycerol dialkyl glycerol tetraethers via selective Accelerated Solvent Extraction. *Organic Geochemistry*, 143: 103979.
- Barker, S., Archer, D., Booth, L., Elderfield, H., Henderiks, J. and Rickaby, R.E., 2006. Globally increased pelagic carbonate production during the Mid-Brunhes dissolution interval and the CO<sub>2</sub> paradox of MIS 11. *Quaternary Science Reviews*, 25(23-24): 3278-3293.
- Bé, A.W.H., Damuth, J.E., Lott, L. and Free, R., 1976. Late Quaternary climatic record in western equatorial Atlantic sediment. *Investigation of Late Quaternary Paleooceanography and Paleoclimatology*, 145: 165.
- Beaufort, L., Bolton, C.T., Sarr, A.-C., Suchéras-Marx, B., Rosenthal, Y., Donnadieu, Y., Barbarin, N., Bova, S., Cornuault, P. and Gally, Y., 2022. Cyclic evolution of phytoplankton forced by changes in tropical seasonality. *Nature*, 601(7891): 79-84.
- Berger, W.H., 1973. Deep-sea carbonates; Pleistocene dissolution cycles. *The Journal of Foraminiferal Research*, 3(4): 187-195.
- Bordiga, M., Beaufort, L., Cobianchi, M., Lupi, C., Mancin, N., Luciani, V., Pelosi, N. and Sprovieri, M., 2013. Calcareous plankton and geochemistry from the ODP site 1209B in the NW Pacific Ocean (Shatsky Rise): New data to interpret calcite dissolution and

- paleoproductivity changes of the last 450 ka. *Palaeogeography, Palaeoclimatology, Palaeoecology*, 371: 93-108.
- Bordiga, M., Cobianchi, M., Lupi, C., Pelosi, N., Venti, N.L. and Ziveri, P., 2014. Coccolithophore carbonate during the last 450 ka in the NW Pacific Ocean (ODP site 1209B, Shatsky Rise). *Journal of Quaternary Science*, 29(1): 57-69.
- Boyd, P.W., Jickells, T., Law, C., Blain, S., Boyle, E., Buesseler, K., Coale, K., Cullen, J., De Baar, H.J. and Follows, M., 2007. Mesoscale iron enrichment experiments 1993-2005: synthesis and future directions. *science*, 315(5812): 612-617.
- Boyle, E.A., 1988. The role of vertical chemical fractionation in controlling late Quaternary atmospheric carbon dioxide. *Journal of Geophysical Research: Oceans*, 93(C12): 15701-15714.
- Broecker, W.S. and Clark, E., 2001. Glacial-to-Holocene redistribution of carbonate ion in the deep sea. *Science*, 294(5549): 2152-2155.
- Broecker, W.S. and Peng, T.H., 1989. The cause of the glacial to interglacial atmospheric CO<sub>2</sub> change: A polar alkalinity hypothesis. *Global Biogeochemical Cycles*, 3(3): 215-239.
- Brunelle, B.G., Sigman, D.M., Cook, M.S., Keigwin, L.D., Haug, G.H., Plessen, B., Schettler, G. and Jaccard, S.L., 2007. Evidence from diatom-bound nitrogen isotopes for subarctic Pacific stratification during the last ice age and a link to North Pacific denitrification changes. *Paleoceanography*, 22(1).
- Brunelle, B.G., Sigman, D.M., Jaccard, S.L., Keigwin, L.D., Plessen, B., Schettler, G., Cook, M.S. and Haug, G.H., 2010. Glacial/interglacial changes in nutrient supply and stratification in the western subarctic North Pacific since the penultimate glacial maximum. *Quaternary Science Reviews*, 29(19-20): 2579-2590.
- Chiu, T.C. and Broecker, W.S., 2008. Toward better paleocarbonate ion reconstructions: New insights regarding the CaCO<sub>3</sub> size index. *Paleoceanography*, 23(2).
- Costa, K.M., McManus, J.F. and Anderson, R.F., 2018. Paleoproductivity and Stratification Across the Subarctic Pacific Over Glacial-Interglacial Cycles. *Paleoceanography and Paleoclimatology*, 33(9): 914-933.
- Costa, K.M., McManus, J.F., Anderson, R.F., Ren, H., Sigman, D.M., Winckler, G., Fleisher, M.Q., Marcantonio, F. and Ravelo, A.C., 2016. No iron fertilization in the equatorial Pacific Ocean during the last ice age. *Nature*, 529(7587): 519-522.
- Crowley, T.J., 1985. Late Quaternary carbonate changes in the North Atlantic and Atlantic/Pacific comparisons. The carbon cycle and atmospheric CO<sub>2</sub>: Natural variations Archean to present, 32: 271-284.
- Crusius, J., Pedersen, T.F., Kienast, S., Keigwin, L. and Labeyrie, L., 2004. Influence of northwest Pacific productivity on North Pacific Intermediate Water oxygen concentrations during the Bølling-Allerød interval (14.7–12.9 ka). *Geology*, 32(7): 633-636.
- Curry, W. and Lohmann, G., 1990. Reconstructing past particle fluxes in the tropical Atlantic Ocean. *Paleoceanography*, 5(4): 487-505.
- Dadey, K.A., Janecek, T. and Klaus, A., 1992. Dry-bulk density: its use and determination, *Proceedings of the Ocean Drilling Program, Scientific Results*. College Station, TX, pp. 551-554.
- Damuth, J.E., 1977. Late Quaternary sedimentation in the western equatorial Atlantic. *Geological Society of America Bulletin*, 88(5): 695-710.
- deMenocal, P., Archer, D. and Leth, P., 1997. Pleistocene variations in deep Atlantic circulation and calcite burial between 1.2 and 0.6 Ma: a combined data-model approach, *Proc. ODP, Sci. Results*, pp. 285-298.



- Emile-Geay, J., Cane, M.A., Naik, N., Seager, R., Clement, A.C. and van Geen, A., 2003. Warren revisited: Atmospheric freshwater fluxes and “Why is no deep water formed in the North Pacific”. *Journal of Geophysical Research: Oceans*, 108(C6).
- Falkowski, P.G., Barber, R.T. and Smetacek, V., 1998. Biogeochemical controls and feedbacks on ocean primary production. *science*, 281(5374): 200-206.
- Farrell, J.W. and Prell, W.L., 1989. Climatic change and CaCO<sub>3</sub> preservation: An 800,000 year bathymetric reconstruction from the central equatorial Pacific Ocean. *Paleoceanography*, 4(4): 447-466.
- Farrell, J.W. and Prell, W.L., 1991. Pacific CaCO<sub>3</sub> preservation and  $\delta^{18}\text{O}$  since 4 Ma: paleoceanic and paleoclimatic implications. *Paleoceanography*, 6(4): 485-498.
- Galbraith, E.D., Kienast, M., Jaccard, S.L., Pedersen, T.F., Brunelle, B.G., Sigman, D.M. and Kiefer, T., 2008. Consistent relationship between global climate and surface nitrate utilization in the western subarctic Pacific throughout the last 500 ka. *Paleoceanography*, 23(2).
- Gardner, J., 1975. Late Pleistocene carbonate dissolution cycles in the eastern equatorial Atlantic.
- Gebhardt, H., Sarnthein, M., Grootes, P.M., Kiefer, T., Kuehn, H., Schmieder, F. and Röhl, U., 2008. Paleonutrient and productivity records from the subarctic North Pacific for Pleistocene glacial terminations I to V. *Paleoceanography*, 23(4).
- Gong, X., Lembke-Jene, L., Lohmann, G., Knorr, G., Tiedemann, R., Zou, J. and Shi, X., 2019. Enhanced North Pacific deep-ocean stratification by stronger intermediate water formation during Heinrich Stadial 1. *Nature communications*, 10(1): 1-8.
- Gottschalk, J., Hodell, D.A., Skinner, L.C., Crowhurst, S.J., Jaccard, S.L. and Charles, C., 2018. Past carbonate preservation events in the deep Southeast Atlantic Ocean (Cape Basin) and their implications for Atlantic overturning dynamics and marine carbon cycling. *Paleoceanography and paleoclimatology*, 33(6): 643-663.
- Gray, W.R., Wills, R.C., Rae, J.W., Burke, A., Ivanovic, R.F., Roberts, W.H., Ferreira, D. and Valdes, P.J., 2020. Wind-driven evolution of the North Pacific subpolar gyre over the last deglaciation. *Geophysical Research Letters*, 47(6): e2019GL086328.
- Hartnett, H.E., Keil, R.G., Hedges, J.I. and Devol, A.H., 1998. Influence of oxygen exposure time on organic carbon preservation in continental margin sediments. *Nature*, 391(6667): 572-575.
- Hays, J.D., Saito, T., Opdyke, N.D. and Burckle, L.H., 1969. Pliocene-Pleistocene sediments of the equatorial Pacific: their paleomagnetic, biostratigraphic, and climatic record. *Geological Society of America Bulletin*, 80(8): 1481-1514.
- Herguera, J., Herbert, T., Kashgarian, M. and Charles, C., 2010. Intermediate and deep water mass distribution in the Pacific during the Last Glacial Maximum inferred from oxygen and carbon stable isotopes. *Quaternary Science Reviews*, 29(9-10): 1228-1245.
- Hodell, D., Charles, C. and Sierro, F., 2001. Late Pleistocene evolution of the ocean's carbonate system. *Earth and Planetary Science Letters*, 192(2): 109-124.
- Hovan, S.A., Rea, D.K. and Pisias, N.G., 1991. Late Pleistocene continental climate and oceanic variability recorded in northwest Pacific sediments. *Paleoceanography*, 6(3): 349-370.
- Isono, D., Yamamoto, M., Irino, T., Oba, T., Murayama, M., Nakamura, T. and Kawahata, H., 2009. The 1500-year climate oscillation in the midlatitude North Pacific during the Holocene. *Geology*, 37(7): 591-594.
- Iwasaki, S., Takahashi, K., Maesawa, T., Sakamoto, T., Sakai, S. and Iijima, K., 2012. Paleoceanography of the last 500 kyrs in the central Okhotsk Sea based on geochemistry. *Deep Sea Research Part II: Topical Studies in Oceanography*, 61: 50-62.

- Jaccard, S., Galbraith, E., Sigman, D.M. and Haug, G., 2010. A pervasive link between Antarctic ice core and subarctic Pacific sediment records over the past 800 kyrs. *Quaternary Science Reviews*, 29(1-2): 206-212.
- Jaccard, S.L. and Galbraith, E.D., 2013. Direct ventilation of the North Pacific did not reach the deep ocean during the last deglaciation. *Geophysical Research Letters*, 40(1): 199-203.
- Jaccard, S.L., Galbraith, E.D., Sigman, D.M., Haug, G.H., Francois, R., Pedersen, T.F., Dulski, P. and Thierstein, H.R., 2009. Subarctic Pacific evidence for a glacial deepening of the oceanic respired carbon pool. *Earth and Planetary Science Letters*, 277(1-2): 156-165.
- Jaccard, S.L., Haug, G.H., Sigman, D.M., Pedersen, T.F., Thierstein, H.R. and Röhl, U., 2005. Glacial/interglacial changes in subarctic North Pacific stratification. *Science*, 308(5724): 1003-1006.
- Jacobel, A., Anderson, R., Winckler, G., Costa, K., Gottschalk, J., Middleton, J., Pavia, F., Shoenfelt, E. and Zhou, Y., 2019. No evidence for equatorial Pacific dust fertilization. *Nature Geoscience*, 12(3): 154-155.
- Jacobel, A., McManus, J., Anderson, R. and Winckler, G., 2017. Climate-related response of dust flux to the central equatorial Pacific over the past 150 kyr. *Earth and Planetary Science Letters*, 457: 160-172.
- Karlin, R., Lyle, M. and Zahn, R., 1992. Carbonate variations in the Northeast Pacific during the late Quaternary. *Paleoceanography*, 7(1): 43-61.
- Kawahata, H. and Ohshima, H., 2002. Small latitudinal shift in the Kuroshio Extension (Central Pacific) during glacial times: evidence from pollen transport. *Quaternary Science Reviews*, 21(14-15): 1705-1717.
- Kawahata, H., Okamoto, T., Matsumoto, E. and Ujiie, H., 2000. Fluctuations of eolian flux and ocean productivity in the mid-latitude North Pacific during the last 200 kyr. *Quaternary Science Reviews*, 19(13): 1279-1291.
- Kienast, S.S., Hendy, I.L., Crusius, J., Pedersen, T.F. and Calvert, S.E., 2004. Export production in the subarctic North Pacific over the last 800 kyrs: No evidence for iron fertilization? *Journal of Oceanography*, 60(1): 189-203.
- Knudson, K.P. and Ravelo, A.C., 2015a. Enhanced subarctic Pacific stratification and nutrient utilization during glacials over the last 1.2 Myr. *Geophysical Research Letters*, 42(22): 9870-9879.
- Knudson, K.P. and Ravelo, A.C., 2015b. North Pacific Intermediate Water circulation enhanced by the closure of the Bering Strait. *Paleoceanography*, 30(10): 1287-1304.
- Kohfeld, K.E. and Chase, Z., 2011. Controls on deglacial changes in biogenic fluxes in the North Pacific Ocean. *Quaternary Science Reviews*, 30(23-24): 3350-3363.
- Kotilainen, A. and Shackleton, N., 1995. Rapid climate variability in the North Pacific Ocean during the past 95,000 years. *Nature*, 377(6547): 323-326.
- LaMontagne, R., Murray, R., Wei, K.Y., Leinen, M. and Wang, C.H., 1996. Decoupling of carbonate preservation, carbonate concentration, and biogenic accumulation: A 400-kyr record from the central equatorial Pacific Ocean. *Paleoceanography*, 11(5): 553-562.
- Le, J. and Shackleton, N.J., 1992. Carbonate dissolution fluctuations in the western Equatorial Pacific during the late Quaternary. *Paleoceanography*, 7(1): 21-42.
- Lembke-Jene, L., Tiedemann, R., Nürnberg, D., Kokfelt, U., Kozdon, R., Max, L., Röhl, U. and Gorbarenko, S.A., 2017. Deglacial variability in Okhotsk Sea Intermediate Water ventilation and biogeochemistry: Implications for North Pacific nutrient supply and productivity. *Quaternary Science Reviews*, 160: 116-137.
- Lisiecki, L.E. and Raymo, M.E., 2005. A Pliocene-Pleistocene stack of 57 globally distributed benthic  $\delta^{18}\text{O}$  records. *Paleoceanography*, 20(1).

- Lüthi, D., Le Floch, M., Bereiter, B., Blunier, T., Barnola, J.-M., Siegenthaler, U., Raynaud, D., Jouzel, J., Fischer, H. and Kawamura, K., 2008. High-resolution carbon dioxide concentration record 650,000–800,000 years before present. *Nature*, 453(7193): 379-382.
- Marchitto, T.M., Lynch-Stieglitz, J. and Hemming, S.R., 2005. Deep Pacific CaCO<sub>3</sub> compensation and glacial–interglacial atmospheric CO<sub>2</sub>. *Earth and Planetary Science Letters*, 231(3-4): 317-336.
- Martínez-García, A., Rosell-Melé, A., Jaccard, S.L., Geibert, W., Sigman, D.M. and Haug, G.H., 2011. Southern Ocean dust–climate coupling over the past four million years. *Nature*, 476(7360): 312-315.
- Max, L., Lembke-Jene, L., Riethdorf, J.-R., Tiedemann, R., Nürnberg, D., Kühn, H. and Mackensen, A., 2014. Pulses of enhanced North Pacific Intermediate Water ventilation from the Okhotsk Sea and Bering Sea during the last deglaciation. *Climate of the Past*, 10(2): 591-605.
- Max, L., Riethdorf, J.-R., Tiedemann, R., Smirnova, M., Lembke-Jene, L., Fahl, K., Nürnberg, D., Matul, A. and Mollenhauer, G., 2012. Sea surface temperature variability and sea-ice extent in the subarctic northwest Pacific during the past 15,000 years. *Paleoceanography*, 27(3).
- McCarron, A., Bigg, G., Brooks, H., Leng, M., Marshall, J., Ponomareva, V., Portnyagin, M., Reimer, P. and Rogerson, M., 2021. Northwest Pacific ice-rafted debris at 38° N reveals episodic ice-sheet change in late Quaternary Northeast Siberia. *Earth and Planetary Science Letters*, 553: 116650.
- Méheust, M., Stein, R., Fahl, K. and Gersonde, R., 2018. Sea-ice variability in the subarctic North Pacific and adjacent Bering Sea during the past 25 ka: new insights from IP 25 and U k<sup>-1</sup> 37 proxy records. *arktos*, 4(1): 8.
- Méheust, M., Stein, R., Fahl, K., Max, L. and Riethdorf, J.-R., 2016. High-resolution IP25-based reconstruction of sea-ice variability in the western North Pacific and Bering Sea during the past 18,000 years. *Geo-Marine Letters*, 36(2): 101-111.
- Monnin, E., Indermühle, A., Dällenbach, A., Flückiger, J., Stauffer, B., Stocker, T.F., Raynaud, D. and Barnola, J.-M., 2001. Atmospheric CO<sub>2</sub> concentrations over the last glacial termination. *Science*, 291(5501): 112-114.
- Narita, H., Sato, M., Tsunogai, S., Murayama, M., Ikehara, M., Nakatsuka, T., Wakatsuchi, M., Harada, N. and Ujiié, Y., 2002. Biogenic opal indicating less productive northwestern North Pacific during the glacial ages. *Geophysical Research Letters*, 29(15): 22-1-22-4.
- Nishioka, J., Nakatsuka, T., Ono, K., Volkov, Y.N., Scherbinin, A. and Shiraiwa, T., 2014. Quantitative evaluation of iron transport processes in the Sea of Okhotsk. *Progress in Oceanography*, 126: 180-193.
- Nishioka, J., Obata, H., Ogawa, H., Ono, K., Yamashita, Y., Lee, K., Takeda, S. and Yasuda, I., 2020. Subpolar marginal seas fuel the North Pacific through the intermediate water at the termination of the global ocean circulation. *Proceedings of the National Academy of Sciences*, 117(23): 12665-12673.
- Nürnberg, D., 2018. RV SONNE Fahrtbericht / Cruise Report SO264 - SONNE-EMPEROR: The Plio/Pleistocene to Holocene development of the pelagic North Pacific from surface to depth – assessing its role for the global carbon budget and Earth's climate, Suva (Fiji) – Yokohama (Japan), 30.6. – 24.8.2018, GEOMAR Helmholtz-Zentrum für Ozeanforschung, Kiel, Germany.
- Nürnberg, D. and Tiedemann, R., 2004. Environmental change in the Sea of Okhotsk during the last 1.1 million years. *Paleoceanography*, 19(4).

- Oba, T. and Murayama, M., 2004. Sea-surface temperature and salinity changes in the northwest Pacific since the Last Glacial Maximum. *Journal of Quaternary Science*, 19(4): 335-346.
- Ohkushi, K.I., Hata, M. and Nemoto, N., 2018. Response of Deep-Sea Benthic Foraminifera to Paleoproductivity Changes on the Shatsky Rise in the Northwestern Pacific Ocean Over the Last 187 Kyr. *Paleontological Research*, 22(4): 326-351.
- Ovsepyan, E.A., Ivanova, E.V., Lembke-Jene, L., Max, L., Tiedemann, R. and Nürnberg, D., 2017. Penultimate and last glacial oceanographic variations in the Bering Sea on millennial timescales: Links to North Atlantic climate. *Quaternary Science Reviews*, 163: 135-151.
- Qin, B., Li, T., Xiong, Z., Algeo, T.J. and Chang, F., 2017. Deepwater carbonate ion concentrations in the western tropical Pacific since 250 ka: Evidence for oceanic carbon storage and global climate influence. *Paleoceanography*, 32(4): 351-370.
- Rae, J.W.B., Gray, W.R., Wills, R.C.J., Eisenman, I., Fitzhugh, B., Fotheringham, M., Littley, E.F.M., Rafter, P.A., Rees-Owen, R., Ridgwell, A., Taylor, B. and Burke, A., 2020. Overturning circulation, nutrient limitation, and warming in the Glacial North Pacific. *Science Advances*, 6(50): eabd1654.
- Reid, J.L. and Lonsdale, P.F., 1974. On the flow of water through the Samoan Passage. *Journal of Physical Oceanography*, 4(1): 58-73.
- Ren, H., Studer, A.S., Serno, S., Sigman, D.M., Winckler, G., Anderson, R.F., Oleynik, S., Gersonde, R. and Haug, G.H., 2015. Glacial-to-interglacial changes in nitrate supply and consumption in the subarctic North Pacific from microfossil-bound N isotopes at two trophic levels. *Paleoceanography*, 30(9): 1217-1232.
- Serno, S., Winckler, G., Anderson, R.F., Jaccard, S.L., Kienast, S.S. and Haug, G.H., 2017. Change in dust seasonality as the primary driver for orbital-scale dust storm variability in East Asia. *Geophysical Research Letters*, 44(8): 3796-3805.
- Sexton, P.F. and Barker, S., 2012. Onset of 'Pacific-style' deep-sea sedimentary carbonate cycles at the mid-Pleistocene transition. *Earth and Planetary Science Letters*, 321: 81-94.
- Shcherbina, A.Y., Talley, L.D. and Rudnick, D.L., 2003. Direct observations of North Pacific ventilation: Brine rejection in the Okhotsk Sea. *Science*, 302(5652): 1952-1955.
- Shigemitsu, M., Narita, H., Watanabe, Y.W., Harada, N. and Tsunogai, S., 2007. Ba, Si, U, Al, Sc, La, Th, C and  $^{13}\text{C}/^{12}\text{C}$  in a sediment core in the western subarctic Pacific as proxies of past biological production. *Marine Chemistry*, 106(3-4): 442-455.
- Siegenthaler, U., Stocker, T.F., Monnin, E., Lüthi, D., Schwander, J., Stauffer, B., Raynaud, D., Barnola, J.-M., Fischer, H. and Masson-Delmotte, V., 2005. Stable carbon cycle-climate relationship during the late Pleistocene. *Science*, 310(5752): 1313-1317.
- Sigman, D.M., Jaccard, S.L. and Haug, G.H., 2004. Polar ocean stratification in a cold climate. *Nature*, 428(6978): 59-63.
- Takahashi, T., Sutherland, S.C., Sweeney, C., Poisson, A., Metzl, N., Tilbrook, B., Bates, N., Wanninkhof, R., Feely, R.A. and Sabine, C., 2002. Global sea-air CO<sub>2</sub> flux based on climatological surface ocean pCO<sub>2</sub>, and seasonal biological and temperature effects. *Deep Sea Research Part II: Topical Studies in Oceanography*, 49(9-10): 1601-1622.
- Takahashi, T., Sutherland, S.C., Wanninkhof, R., Sweeney, C., Feely, R.A., Chipman, D.W., Hales, B., Friederich, G., Chavez, F., Sabine, C., Watson, A., Bakker, D.C.E., Schuster, U., Metzl, N., Yoshikawa-Inoue, H., Ishii, M., Midorikawa, T., Nojiri, Y., Körtzinger, A., Steinhoff, T., Hoppema, M., Olafsson, J., Arnarson, T.S., Tilbrook, B., Johannessen, T., Olsen, A., Bellerby, R., Wong, C.S., Delille, B., Bates, N.R. and de Baar, H.J.W., 2009. Climatological mean and decadal change in surface ocean pCO<sub>2</sub>, and net sea-air

- CO<sub>2</sub> flux over the global oceans. *Deep Sea Research Part II: Topical Studies in Oceanography*, 56(8-10): 554-577.
- Talley, L.D., 1993. Distribution and formation of North Pacific intermediate water. *Journal of Physical Oceanography*, 23(3): 517-537.
- Thompson, P.R. and Saito, T., 1974. Pacific Pleistocene sediments: Planktonic foraminifera dissolution cycles and geochronology. *Geology*, 2(7): 333-335.
- Tjallingii, R., Röhl, U., Kölling, M. and Bickert, T., 2007. Influence of the water content on X-ray fluorescence core-scanning measurements in soft marine sediments. *Geochemistry, Geophysics, Geosystems*, 8(2).
- Verardo, D.J. and McIntyre, A., 1994. Production and destruction: Control of biogenous sedimentation in the tropical Atlantic 0–300,000 years BP. *Paleoceanography*, 9(1): 63-86.
- Volat, J.-L., Pastouret, L. and Vergnaud-Grazzini, C., 1980. Dissolution and carbonate fluctuations in Pleistocene deep-sea cores: a review. *Marine Geology*, 34(1-2): 1-28.
- Wang, W., von Dobeneck, T., Frederichs, T., Zhang, Y., Lembke-Jene, L., Tiedemann, R., Winklhofer, M. and Nürnberg, D., 2021. Dating North Pacific Abyssal Sediments by Geomagnetic Paleointensity: Implications of Magnetization Carriers, Plio-Pleistocene Climate Change, and Benthic Redox Conditions. *Frontiers in Earth Science*: 577.
- Warren, B.A., 1983. Why is no deep water formed in the North Pacific? *Journal of Marine Research*, 41(2): 327-347.
- Weltje, G.J. and Tjallingii, R., 2008. Calibration of XRF core scanners for quantitative geochemical logging of sediment cores: Theory and application. *Earth and Planetary Science Letters*, 274(3-4): 423-438.
- Winckler, G., Anderson, R.F., Jaccard, S.L. and Marcantonio, F., 2016. Ocean dynamics, not dust, have controlled equatorial Pacific productivity over the past 500,000 years. *Proceedings of the National Academy of Sciences*, 113(22): 6119-6124.
- Wong, K.H., Obata, H., Nishioka, J., Yamashita, Y., Kondo, Y., Kim, T., Mashio, A. and Hasegawa, H., 2022. Subarctic Pacific Intermediate Water: An Oceanic Highway for the Transport of Trace Metals in the North Pacific. *Limnology and Oceanography Bulletin*, 31(2): 31-36.
- Wu, G., Yasuda, M. and Berger, W., 1991. Late Pleistocene carbonate stratigraphy on Ontong-Java Plateau in the western equatorial Pacific. *Marine Geology*, 99(1-2): 135-150.
- Yang, H., Lohmann, G., Krebs-Kanzow, U., Ionita, M., Shi, X., Sidorenko, D., Gong, X., Chen, X. and Gowan, E.J., 2020. Poleward shift of the major ocean gyres detected in a warming climate. *Geophysical Research Letters*, 47(5): e2019GL085868.
- Yang, H., Lohmann, G., Wei, W., Dima, M., Ionita, M. and Liu, J., 2016. Intensification and poleward shift of subtropical western boundary currents in a warming climate. *Journal of Geophysical Research: Oceans*, 121(7): 4928-4945.
- Yasudomi, Y., Motoyama, I., Oba, T. and Anma, R., 2014. Environmental fluctuations in the northwestern Pacific Ocean during the last interglacial period: evidence from radiolarian assemblages. *Marine Micropaleontology*, 108: 1-12.
- Yuan, X. and Talley, L.D., 1992. Shallow salinity minima in the North Pacific. *Journal of physical oceanography*, 22(11): 1302-1316.
- Zahn, R., Rushdi, A., Pisias, N.G., Bornhold, B.D., Blaise, B. and Karlin, R., 1991. Carbonate deposition and benthic  $\delta^{13}\text{C}$  in the subarctic Pacific: implications for changes of the oceanic carbonate system during the past 750,000 years. *Earth and planetary science letters*, 103(1-4): 116-132.
- Zhang, J., Wang, P., Li, Q., Cheng, X., Jin, H. and Zhang, S., 2007. Western equatorial Pacific productivity and carbonate dissolution over the last 550 kyr: Foraminiferal and

nannofossil evidence from ODP Hole 807A. *Marine Micropaleontology*, 64(3-4): 121-140.

#### 4.11. Supplementary

Table S1. AMS  $^{14}\text{C}$  ages of the SO202-37-2 with calibrated calendar ages.

AWI no.	Depth (cm)	Species	Radiocarbon age (yr)	Median calendar age (yr)	Calendar age $\pm 2\sigma$ (yr)
3943.1.1	2.5	<i>G. bulloides</i>	3427 $\pm$ 84	3121	2865 - 3361
3954.1.1	38.5	<i>G. bulloides</i>	18195 $\pm$ 175	21071	20569 - 21622
3957.1.1	50.5	<i>G. bulloides</i>	24356 $\pm$ 304	27678	27118 - 28381

Table S2. Age model of cores SO202-37-2 and SO264-55-1. C14: base on radiocarbon dating on planktonic foraminifera.  $\delta^{18}\text{O}$ : benthic  $\delta^{18}\text{O}$  correlation of cores to the benthic  $\delta^{18}\text{O}$  stack of Lisiecki and Raymo (2005). Tiepoint-XRF: XRF correlation of elemental ratio records of cores to Ba/Al of ODP site 882 (Jaccard et al., 2010) and benthic  $\delta^{18}\text{O}$  stack (Lisiecki and Raymo, 2005). Tephra: tephra identification during cruise (Nürnberg, 2018b).

SO202-37-2			SO264-55-1		
Depth (cm)	Age (ka)	Comment	Depth (cm)	Age (ka)	Comment
2.5	0.3121	C14	5.5	6.8	C14
38.5	21.071	C14	17.5	10.5	C14
50.5	27.678	C14	29.5	13.2	C14
144.51088	61.9050371	Tiepoint-XRF, $\delta^{18}\text{O}$	195.5	15.7	C14
170.62219	87.0033952	Tiepoint-XRF, $\delta^{18}\text{O}$	215.5	18.5	C14
210.931395	109.245372	Tiepoint-XRF, $\delta^{18}\text{O}$	295.5	29.1	C14
226.604758	122.881445	Tiepoint-XRF, $\delta^{18}\text{O}$	315.5	30	C14
238.493455	130.002998	Tiepoint-XRF, $\delta^{18}\text{O}$	325.5	33.9	C14
250.612875	135.096335	Tiepoint-XRF, $\delta^{18}\text{O}$	335.5	39.8	C14
274.386716	140.034508	Tiepoint-XRF	387.126418	59.1342889	Tiepoint-XRF
318.816284	156.070793	Tiepoint-XRF	431.4	64.6	Tiepoint-XRF
404.51441	184.991101	Tiepoint-XRF, $\delta^{18}\text{O}$	455.4	68.1	Tiepoint-XRF, $\delta^{18}\text{O}$
420.578499	192.109947	Tiepoint-XRF, $\delta^{18}\text{O}$	473.6	70.2	Tiepoint-XRF
439.660376	204.918033	Tiepoint-XRF, $\delta^{18}\text{O}$	483	72.8	Tiepoint-XRF
463.729797	223.137533	Tiepoint-XRF, $\delta^{18}\text{O}$	500	77	Tiepoint-XRF
500.428148	252.079519	Tiepoint-XRF, $\delta^{18}\text{O}$	503.9	78.6	Tiepoint-XRF
617.740744	280.191426	Tiepoint-XRF, $\delta^{18}\text{O}$	550.9	86.3	Tiepoint-XRF
643.680263	294.135513	Tiepoint-XRF, $\delta^{18}\text{O}$	574.3	90.8	Tiepoint-XRF
661.725258	319.918485	Tiepoint-XRF	614.4	103.8	Tiepoint-XRF
679.559759	329.07643	Tiepoint-XRF, $\delta^{18}\text{O}$	649.6	108.5	Tiepoint-XRF
696.927318	341.463415	Tiepoint-XRF, $\delta^{18}\text{O}$	707.2	111.4	Tiepoint-XRF
718.936637	348.095582	Tiepoint-XRF, $\delta^{18}\text{O}$	761.8	123	$\delta^{18}\text{O}$
824.507168	396.441423	Tiepoint-XRF, $\delta^{18}\text{O}$	769.8	124.9	Tiepoint-XRF
870.618071	417.033187	Tiepoint-XRF, $\delta^{18}\text{O}$	777.5	130	$\delta^{18}\text{O}$
987.212309	455.06943	Tiepoint-XRF, $\delta^{18}\text{O}$	781.5	135.2	Tiepoint-XRF
1063.9383	478.968488	Tiepoint-XRF	797.8	140	$\delta^{18}\text{O}$
1119.62574	490.965974	Tiepoint-XRF, $\delta^{18}\text{O}$	823.6	144	$\delta^{18}\text{O}$
1205.69704	524.192979	Tiepoint-XRF	1011.8037	190.346895	Tiepoint-XRF, $\delta^{18}\text{O}$
			1029.19061	197.569288	Tiepoint-XRF, $\delta^{18}\text{O}$
			1038.75376	203.256599	Tiepoint-XRF, $\delta^{18}\text{O}$
			1084.27235	217.455661	Tiepoint-XRF, $\delta^{18}\text{O}$

1103.92256	222.650992	Tiepoint-XRF, $\delta^{18}\text{O}$
1164.77231	244.154304	Tiepoint-XRF, $\delta^{18}\text{O}$
1279.60968	282.915134	Tiepoint-XRF, $\delta^{18}\text{O}$
1297.63259	299.502294	Tiepoint-XRF, $\delta^{18}\text{O}$
1348.14672	328.190038	Tiepoint-XRF, $\delta^{18}\text{O}$
1410.83943	350.400735	Tiepoint-XRF, $\delta^{18}\text{O}$
1514.26789	405.780247	Tiepoint-XRF
1545.5	421.2	Tephra

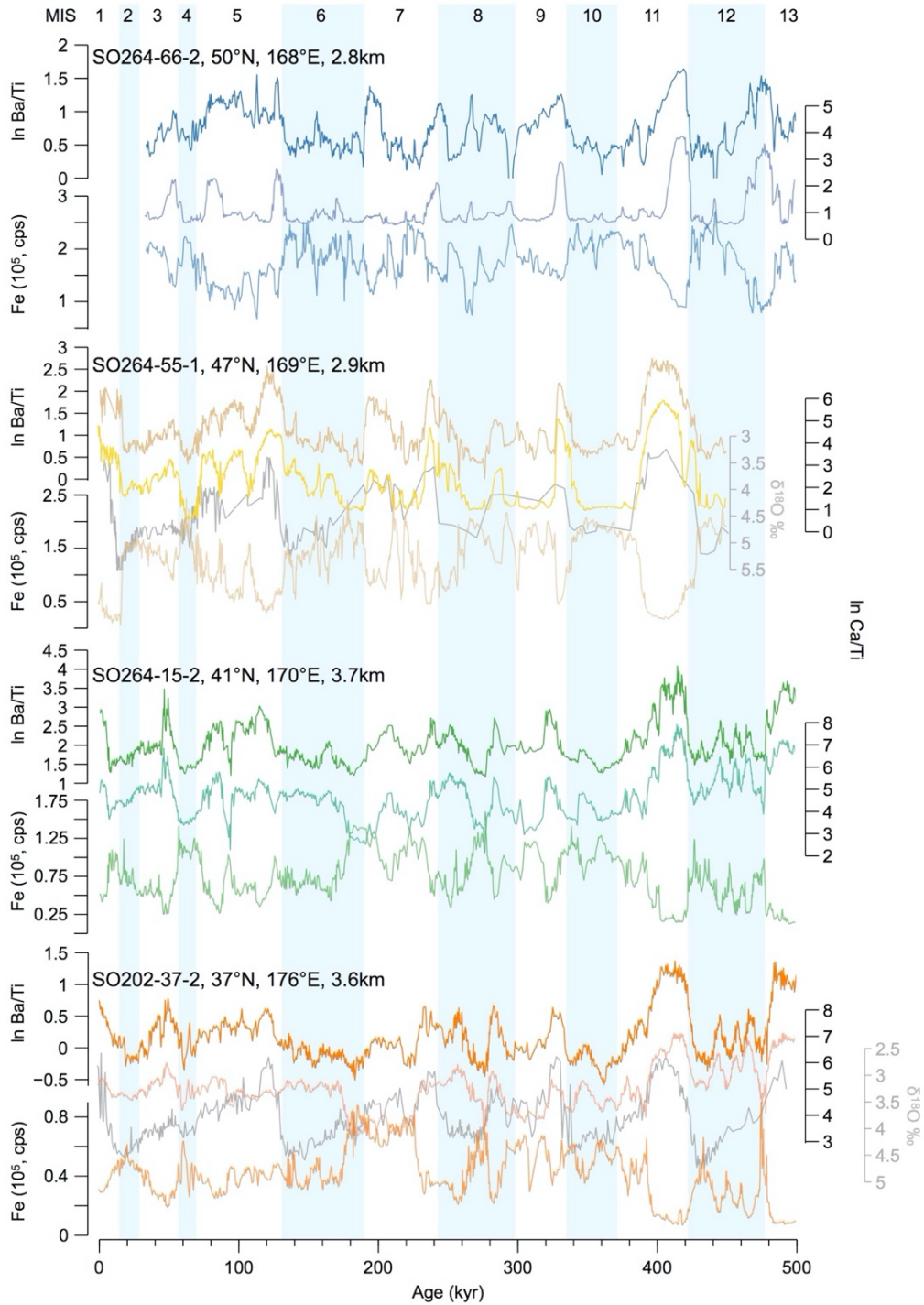


Figure S1. XRF  $\ln\text{-Ba/Ti}$  (upper curve) and  $\ln\text{-Ca/Ti}$  (lower curve) ratios of the Northwest Pacific cores plotted against age and the two benthic  $\delta^{18}\text{O}$  records (SO264-55-1 and SO202-37-2) in gray line at the back as comparison. Marine Isotope Stages: MIS 1 to 13. Light blue shadings indicate glacial stages.

## Reference

- Jaccard, S., Galbraith, E., Sigman, D.M. and Haug, G., 2010. A pervasive link between Antarctic ice core and subarctic Pacific sediment records over the past 800 kyrs. *Quaternary Science Reviews*, 29(1-2): 206-212.
- Lisiecki, L.E. and Raymo, M.E., 2005. A Pliocene-Pleistocene stack of 57 globally distributed benthic  $\delta^{18}\text{O}$  records. *Paleoceanography*, 20(1).
- Nürnberg, D., 2018. RV SONNE Fahrtbericht / Cruise Report SO264 - SONNE-EMPEROR: The Plio/Pleistocene to Holocene development of the pelagic North Pacific from surface to depth – assessing its role for the global carbon budget and Earth's climate, Suva (Fiji) – Yokohama (Japan), 30.6. – 24.8.2018, GEOMAR Helmholtz-Zentrum für Ozeanforschung, Kiel, Germany.



## 5. Variations in North Pacific Deep Water characteristics and ventilation patterns over the past 540,000 years

Weng-Si Chao <sup>\* 1</sup>, Lester Lembke-Jene <sup>1</sup>, Ralf Tiedemann <sup>1</sup>

<sup>1</sup> Alfred-Wegener-Institut Helmholtz-Zentrum für Polar- und Meeresforschung, Bremerhaven, Germany

\*Corresponding author: weng-si.chao@awi.de

Submitting journal: *Climate of the Past*

Last updated: 15.01.2023

### Abstract

The ventilation and circulation history in the North Pacific remains underexplored, despite its important role in the global meridional overturning circulation and marine carbon cycle. Ocean chemistry and bathymetric constraints increase the difficulty in obtaining carbonate-based proxy records compared to the North Atlantic, in particular monospecific benthic stable isotope time series. In this study, we present a new benthic foraminiferal record from a sediment core recovered from the deep bathyal Northwest (NW) Pacific that extends back to about 540,000 years before present, comprising Marine Isotope Stage (MIS) 13. We used the epibenthic species *Cibicidoides wuellerstorfi*, widely regarded as faithfully reflecting the deep water isotopic composition of dissolved inorganic carbon. Comparisons between North Pacific Deep Water (NPDW) and its end-member water masses Circumpolar Deep Water (CDW) and North Pacific Intermediate Water (NPIW) suggest a long-term change in CDW influence onto North Pacific bathyal water masses. Differences of stable isotopes results also indicated a general stagnant NPDW during the last four glacial-interglacial cycles, however, an absence of stratification in the NW Pacific was observed during terminations II to V. A switch from strong ventilation in NPDW (warm intervals) to better ventilated NPIW (cold intervals) during MIS 10 to 13 was clearly recorded in the benthic carbon isotopes differences signal. Our observations show that the NW Pacific acts not only as a carbon reservoir but also as a source of

atmospheric CO<sub>2</sub> via deep water upwelling and mid-depth to deep homogenization during terminations and warm intervals. The rapid ocean ventilation changes and the collapse of halocline during terminations further suggests the release of preserved CO<sub>2</sub> to the atmosphere from the NW Pacific.

## **5.1. Introduction**

The global Meridional Overturning Circulation (MOC) convects heat, salt (salinity), carbon and nutrients throughout the global ocean and is closely connected with our climate system. It is mainly sustained by deep water convection in the North Atlantic and Southern Ocean, and is transported throughout most oceanic basins toward the North Pacific (Talley, 2013). Whereas the Atlantic Meridional Overturning Circulation (AMOC) has been intensively investigated, relatively little is known about the Pacific limb of the MOC.

Today, the North Pacific plays a relatively passive role in the MOC compared to the North Atlantic where the deep water is formed. North Atlantic Deep Water exports to the Southern Ocean and mixes with Circumpolar Deep Water (CDW). This large water mass in the Southern Ocean includes the Upper Circumpolar Deep Water, the Lower Circumpolar Deep Water (LCDW), the Antarctic Intermediate Water (AAIW) and the Antarctic Bottom Water (Talley, 2013). The flow of CDW and/or LCDW continue northward along the southwest Pacific basin into the North Pacific as Pacific Deep Water (PDW). The upwelling of the PDW is limited in the Northwest (NW) Pacific due to the overlaying North Pacific Intermediate Water (NPIW) which originates in the marginal seas. So that part of the PDW upwells to the shallow depths in the equatorial Pacific and, together with the AAIW, feed the equatorial waters (Figure 1B). These pathways cause the deep NW Pacific one of the oldest and important end members in the global overturning circulation.

The modern deep North Pacific is largely isolated from the atmosphere and has little interaction with surface waters, due to low surface salinities and the resulting strong stratification (Warren, 1983). Being the terminus of the global MOC, the vast area of the deep North Pacific harbors the world's oldest and most nutrient-rich deep waters, thereby acting as an enormous storage capacitor for carbon in the form of dissolved inorganic carbon (DIC) due to the accumulation along the circulation path. Since the amount of oceanic carbon is about 50 times as large as the atmospheric carbon (Broecker et al., 1980), the vast, deep Pacific and its

meridional overturning Circulation (PMOC) dynamic play an important role in the marine carbon cycle and has potentially large impacts on climate.

Stable oxygen and carbon isotopes are widely used in paleoceanography to reconstruct physical changes of water masses as well as variations in ice sheet dynamics, and provide information about changes in circulation and ventilation, and nutrient contents in the ocean. Generally, the  $\delta^{13}\text{C}$  of benthic foraminifera reflects the  $\delta^{13}\text{C}$  of the DIC signal in seawater at the corresponding location. Given that the older and longer the water mass is transported, the more organic matter from the overlaying surface water rains down and is remineralized with associated nutrient enrichment, which reduces the water masses'  $\delta^{13}\text{C}$  values. The deep Pacific was found to be more  $\delta^{13}\text{C}$  depleted and nutrient-enriched during the last glacial, suggesting an increase of respiratory  $\text{CO}_2$  from the surface ocean in the bathyal to abyssal waters below ca. 2000 m (e.g., Herguera et al., 1992; Keigwin, 1998; Matsumoto et al., 2002).

Previous works have indicated that changes in circulation and both surface ocean and mid-depth to deep stratification in this region likely led to both glacial enhanced carbon storage and subsequent deglacial  $\text{CO}_2$  outgassing, contributing to atmospheric  $\text{CO}_2$  rises (Galbraith et al., 2007; Gong et al., 2019; Gray et al., 2018; Gray et al., 2020; Max et al., 2014; Rae et al., 2020; Riethdorf et al., 2013). However, the role of the mid-depth to deep North Pacific water mass configuration and its source waters' influence on chemical signatures remain poorly understood. Due to the broad abyssal Pacific plains combined with a shallow lysocline and thus carbonate-corrosive waters, only few carbonate-bearing sediment locations exist for proxy-based reconstructions. However, these available data usually do not go back much further than the last glacial cycle (e.g., Gray et al., 2018; Keigwin, 1998; Lund and Mix, 1998; Matsumoto et al., 2002; Rae et al., 2014). Only few long-term records exist, which allowed to reconstruct circulation changes, NPDW and NPIW water mass signatures and their nutrient budgets by measuring stable isotopes on benthic foraminifera (e.g., Ford and Raymo, 2020; Gebhardt et al., 2008; Mix et al., 1991; Zahn and Mix, 1991; Zahn et al., 1991).

Here, we aim to provide new information on ventilation changes in NPDW since Marine Isotope Stage (MIS) 13 and present a monospecific benthic foraminiferal record from the deep NW Pacific (Figure 1), measured on *Cibicidoides wuellerstorfi*, reflecting bottom water carbon isotope compositional changes (Duplessy et al., 1984; Lutze and Thiel, 1989). Furthermore, we compared the acquired  $\delta^{13}\text{C}$  data from NPDW with  $\delta^{13}\text{C}$  signatures of its potential source

water masses from the Bering Sea and Southern Ocean, in order to investigate potential changes in source water contributions on NPDW and its characteristics on orbital timescales.

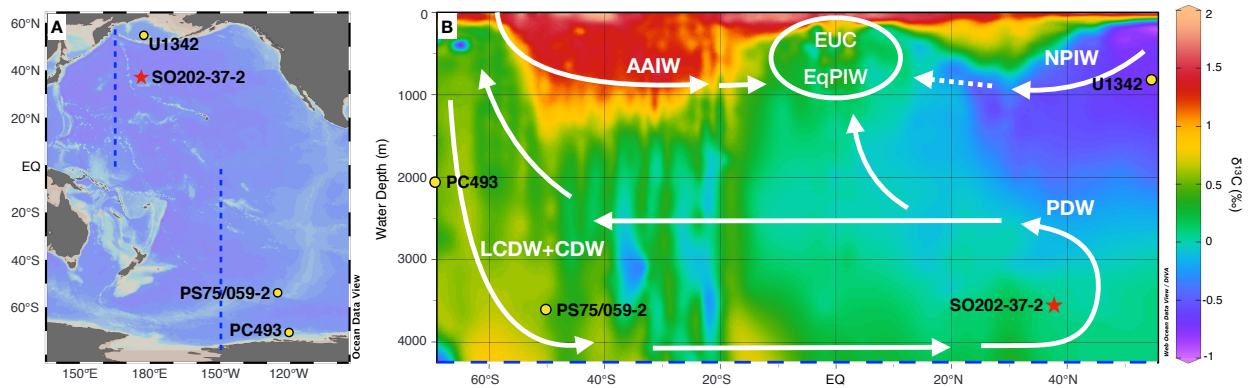


Figure 6. (A) Map of the study region and core locations used in this study: piston core SO202-37-2, marked by red star, from the Northwest Pacific, other cores for comparison (yellow circles). Blue dashed lines show meridional sections shown in panel (B). (B) Meridional section of present-day carbon isotope concentration and major modern mid-depth to deep-water masses (white arrows): AAIW = Antarctic Intermediate Water; CDW = Circumpolar Deep Water; EUC = Equatorial Undercurrent; EqPIW = Equatorial Pacific Intermediate Water; NPIW = North Pacific Intermediate water; PDW = Pacific Deep Water). Map was generated using Ocean Data View (ODV, Schlitzer, 2015). Section plot was made by webODV, using data from Schmittner et al. (2017).

## 5.2. Material and Methods

### 5.2.1. Sample material and stable isotopes

Piston core SO202-37-2 (37°46.07'N 176°16.13'E; 3568m water depth) was retrieved from the northern flank of Hess Rise in the northwest Pacific during expedition SO202 INOPEX of R/V SONNE in 2009 (Figure 1). The sediment core was sampled in 1 cm-thick slices and every third sample was processed for stable isotope measurements. Samples were freeze-dried, washed over a 63- $\mu$ m sieve and dried in an oven at 50°C. Benthic foraminifera of the epibenthic species *C. wuellerstorfi* were picked from the 250-500  $\mu$ m size fraction. All measurements were carried out at the Stable Isotope Facility of the Alfred-Wegener-Institute in Bremerhaven, using a Thermo Finnigan MAT 253 isotope ratio mass-spectrometer coupled to an automated KIEL IV CARBO preparation device. Stable oxygen isotope ratios ( $\delta^{18}O$ ) and stable carbon isotope ratios ( $\delta^{13}C$ ) are expressed in the  $\delta$ -notation with reference to Vienna Pee Dee belemnite (VPDB) standard. The measurements were calibrated to VPDB using the international NIST 19 standard. Long-time reproducibility based on NIST-19 and an in-house carbonate standard is  $\pm 0.06$  ‰ for  $\delta^{18}O$  and  $\pm 0.04$  ‰ for  $\delta^{13}C$ . Most of the benthic  $\delta^{18}O$  data of core SO202-37-2 has been presented previously (Chapter 4 of this thesis).

### 5.2.2. Age model

The relatively high abundance and good preservation of foraminifera provided high-resolution stable isotope records from the pelagic water region of the NW Pacific. The SO202-37-2 age model was based on the correlation of the  $\delta^{18}\text{O}$  record to the LR04 benthic  $\delta^{18}\text{O}$  stack (Lisiecki and Raymo, 2005), using the software *AnalySeries* 2.0.8 (Paillard et al., 1996). For the last 500 ka BP, the age model was based on Chao et al. (in prep.; Chapter 4 of this thesis). This study increased the resolution before 450 ka BP and extended the record until 540 ka BP.

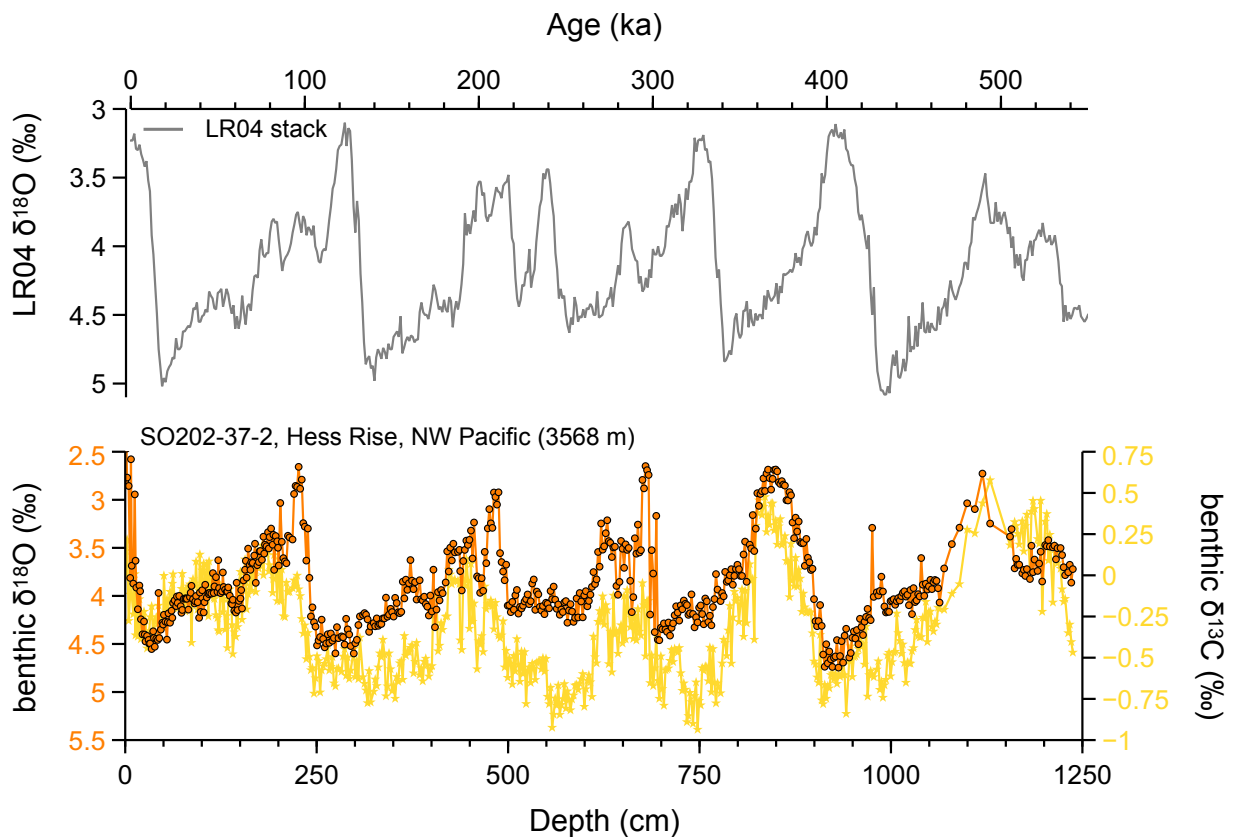


Figure 2. Benthic foraminiferal  $\delta^{18}\text{O}$  (orange line and dots) and  $\delta^{13}\text{C}$  (yellow line and stars) measured on *C. wuellerstorfi* from core SO202-37-2 located in the deep bathyal NW Pacific, against the core depth, comparing with LR04 benthic  $\delta^{18}\text{O}$  stack (gray line) from the upper panel.

### 5.3. Results and Discussion

Here, we present a new benthic isotope record from the deep bathyal NW Pacific covering the last 540,000 years before present (ka BP). Stable isotopes from core SO202-37-2 (Hess Rise, 3568 m water depth) were measured solely on the benthic foraminifera species *C. wuellerstorfi*, which reflects the bottom water carbon isotope compositional changes due to its elevated epibenthic habitat (Duplessy et al., 1984; Lutze and Thiel, 1989). Comparing to the often-used deep reference core from the Eastern Equatorial Pacific which has partially

measured on *Uvigerina peregrina*, ODP Site 849 (3851 m water depth; Mix et al., 1995) widely thought to represent whole ocean changes, this high-resolution isotope record also clearly displays all Marine Isotope Stages since 540 ka BP, but ideally reflects the evolution of North Pacific Deep Water (NPDW, cf. supplemental figure S1). Therefore, we use monospecific SO202-37-2 benthic record to investigate past NPDW characteristics and ventilation changes in the NW Pacific.

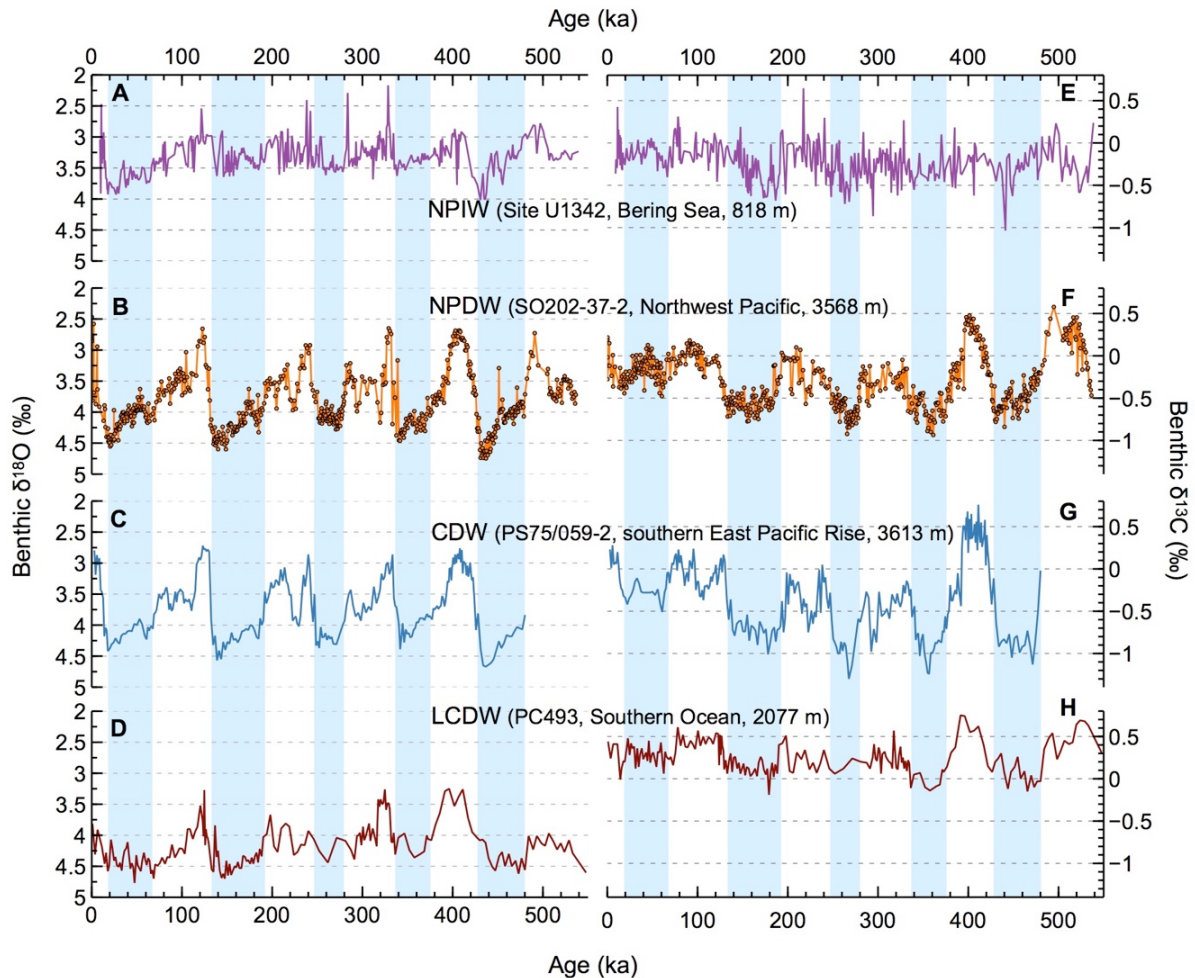


Figure 3. Stable isotopes changes in NPDW and its related source water masses. (A - D) Benthic foraminiferal  $\delta^{18}\text{O}$  records from Site U1342 (purple line), SO202-37-2 (this study, orange line and dots), PS75/059-2 (blue line) and PC493 (brown line). (E - H) Benthic foraminiferal  $\delta^{13}\text{C}$  records from the same sites (matching color). Light blue bars mark glacial intervals MIS 2-4, 6, 8, 10 and 12.

The  $\delta^{18}\text{O}$  values of SO202-37-2 range between 2.468‰ and 4.746‰, with two largest amplitudes from MIS 12 to 11 and MIS 2 to 1 of about 2.0‰ (Figure 3B). The  $\delta^{13}\text{C}$  shows values in the range of -0.936‰ to 0.578‰, with a slow and long-term stepwise increase occurs from MIS 8 towards the early Holocene (Figure 3F). The largest  $\delta^{13}\text{C}$  amplitude arises again from MIS 12 to 11 of about 1.2‰.

Based on our NPDW  $\delta^{13}\text{C}$  record (Figure 3F), values in MIS 3 and 5 are relatively similar to modern values of  $\sim 0\text{‰}$  to  $0.2\text{‰}$  and became more negative during MIS 7 and 9. This indicates a deep water mass comparable to the modern, isolated deep water setting, or an even more nutrient-enriched less-ventilated NPDW during MIS 7 and 9. This appears to contradict the assumption that the subarctic Pacific itself was better ventilated than today, except MIS 11 and 13 of which they had relatively positive values up to  $0.5\text{‰}$  to  $0.6\text{‰}$  (Figure 3F). Additionally, the  $\delta^{13}\text{C}$  variation in NPDW was weak since MIS 5 with a less pronounced Eemian peak, comparing to Circumpolar Deep Water (CDW) the southern source water mass of NPDW (Figure 3F and G). This low amplitude variation signal, with no strong G-IG cyclicity was rather toward the northern end-member North Pacific Intermediate Water (NPIW) with comparable values (Figure 3E and F). All these manifestations indicate the deep water circulation or the carbon chemistry in the North Pacific behaved differently during the last five G-IG cycles.

### **5.3.1. CDW characteristics in NW Pacific**

We first compare our results to Southern Ocean core PS75/059-2 (East Pacific Rise, 3613 m water depth; Ullermann et al., 2016), which today is bathed in the core of Pacific CDW on the western flank of the East Pacific Rise. We also compare our record with Southern Ocean-sourced Lower Circumpolar Deep Water (LCDW) to Antarctic Bottom Water (AABW) bathing the site PC493 (2077 m water depth; Williams et al., 2019), in order to evaluate the potential influence of end-member water masses deeper than CDW from the Southern Ocean.

Today, CDW modified by Antarctic Bottom Water (AABW) originates from the Southern Ocean and is transported along pathway of the Southwest Pacific Basin and through the Samoan Passage into the North Pacific. On orbital time scales, parallel patterns and amplitudes between the benthic stable isotope records of SO202-37-2 and PS75/059-2 indicate the coupling between CDW and NPDW (Figure 3B and C, F and G). The corresponding  $\delta^{18}\text{O}$  signals of both cores imply a similar temperature and/or salinity development of these two water masses for the last five glacial-interglacial cycles. We observe generally higher benthic  $\delta^{13}\text{C}$  values in NPDW than in CDW (Figure 3F and G, 4A), the maximum benthic  $\delta^{13}\text{C}$  offset between SO202-37-2 and PS75/059-2 occurring during MIS 12.

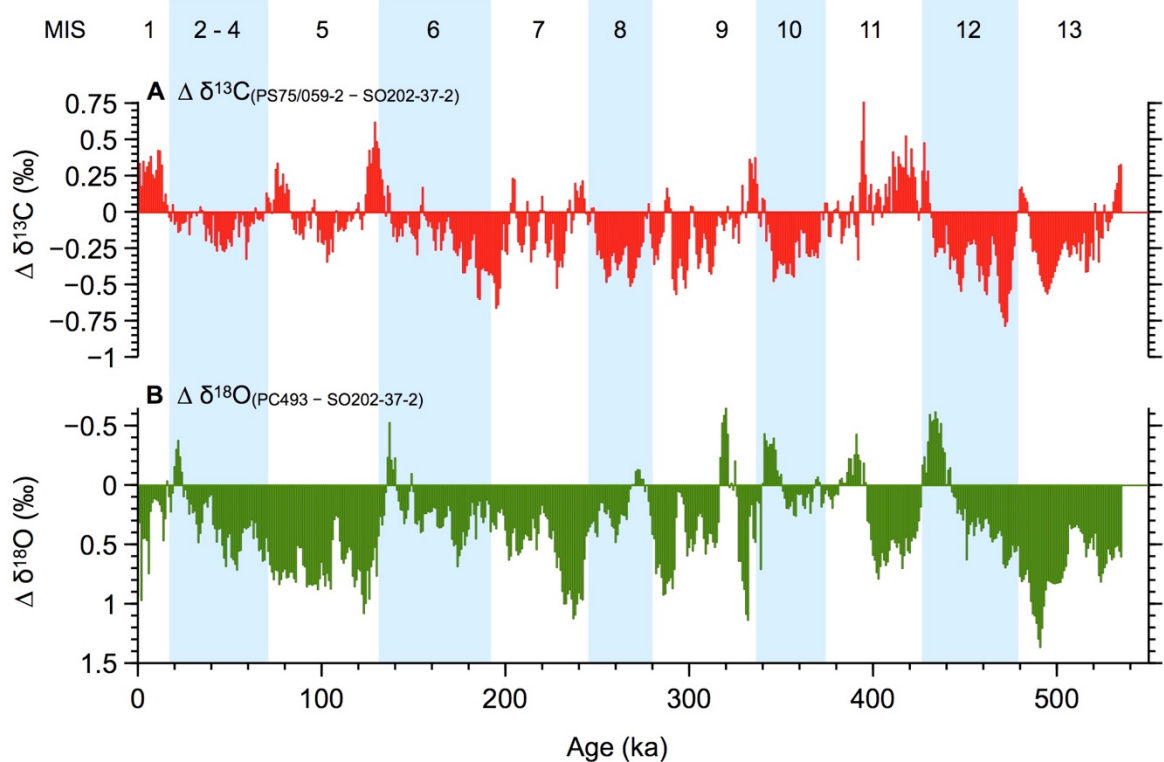


Figure 4. Comparison between Northwest Pacific and Southern Ocean. (A) Difference between benthic  $\delta^{13}\text{C}$  records of PS75/059-2 and SO202-37-2. (B) Difference between benthic  $\delta^{18}\text{O}$  records of PC493 and SO202-37-2. All records were resampled in 1 ka spacing with linear interpolation between data points before subtraction. For resampling the AnalySeries program was used (Paillard et al., 1996). Light blue bars mark glacial intervals.

Assuming past PMOC configurations had a similar routing to today, with equal or longer residence time between the Southern Ocean to the North Pacific, higher organic material remineralization and nutrient concentrations should result in lower  $\delta^{13}\text{C}$  signals in the deep North Pacific. The opposite occurs to appear, though, leading us to assume either a different circulation configuration of NPDW or other relative contributions by source water masses in the past.

One could explain the generally higher  $\delta^{13}\text{C}$  signal by a better ventilation in NPDW. An increase of deep-water ventilation could be promoted by invasion of a young, better ventilated water mass, or by localized deep convection that brings near-surface waters to greater depths. As deep waters travel from the North Atlantic via the Southern Ocean into the deep Pacific, they progressively accumulate nutrients and become depleted in  $^{13}\text{C}$ , decreasing their  $\delta^{13}\text{C}$  signatures by remineralization of sinking organic matter. The path of these aging water masses can therefore be traced from evolving  $\delta^{13}\text{C}$  gradients if no other processes set back the  $\delta^{13}\text{C}$  signatures. We investigated the temporal and spatial differences of the water mass that occupies our site in relation to its presumed source water mass by calculating the  $\delta^{13}\text{C}$  difference between



NPDW and CDW ( $\Delta\delta^{13}\text{C}$ , Figure 4A). The resulting values not only display generally lower values of  $\delta^{13}\text{C}$  in CDW, but also point to a 400-ka-like variation, potentially of a cyclic nature between late MIS 6 to late MIS 11, though the length of our record precludes a full assessment of this assumption. This smooth bowl shape gradient between the two water masses might indicate the strength or the flow speed change of the water mass itself being subject to a long-term variation. The  $\delta^{13}\text{C}$  gradient suggests an enhanced NPDW ventilation inferred from decreasing  $\Delta\delta^{13}\text{C}$  values since MIS 11, and might be associated with a generally increased northward flow speed in CDW starting around MIS 12-11. This assumption would be supported by evidence from the North Chatham Drift off New Zealand, where inflow to the deep SW Pacific increased via the Deep Western Boundary Current in conjunction with better ventilated southern-sourced waters (Hall et al., 2001).

At our site, likewise a long-term trend towards more positive in  $\delta^{13}\text{C}$  starting from MIS 8 or earlier is observed in CDW than NPDW (Figure 3F and G). In addition, the positive  $\Delta\delta^{13}\text{C}$  indicated a more ventilated water mass in CDW compared to NPDW, mostly evident during (peak) interglacials (Figure 4A). Whether this indicates a stronger ventilation in the Southern Ocean during interglacials, or an alteration of the productivity regime remains to be investigated. On shorter time-scales, the amplitudes of the (peak) interglacial periods are less pronounced in NPDW, such as MIS 5e, 7e, 9 and 11e (Figure 3F). These deviations might infer differentially evolving water mass characteristics between the West and East Pacific basins, which would then be reflected in the locations of the two core sites. Regarding the core locations, the CDW signal could be influenced by the outflow of NPDW towards the Southeast Pacific, in which it contributes more depleted  $\delta^{13}\text{C}$  values. On the other hand, given that CDW is a voluminous water mass in the Southern Ocean and it comprises multiple source water masses (AABW, NADW, U/LCDW), the distribution of CDW  $\delta^{13}\text{C}$  could be subject various alteration processes through mixing. As a comparison, the core bathed at LCDW yields much higher  $\delta^{13}\text{C}$  values throughout (Figure 3H) indicating the complexity of the  $\delta^{13}\text{C}$  composition in relation to deep- and bottom-water formation in the Southern Ocean (Williams et al., 2019).

Overall, interglacial NPDW was not better ventilated than today since MIS 9. However, exceptions occurred during MIS 11 and 13, as inferred from more positive  $\delta^{13}\text{C}$  values. The peak interglacial MIS 11 is prominently expressed in our NPDW record, with  $\delta^{13}\text{C}$  maxima of up to 0.5‰ surpassing modern values (Figure 3F). Such high  $\delta^{13}\text{C}$  values also appeared in CDW and LCDW, indicating a more active PMOC and NPDW ventilation compared to modern conditions, while the marginal seas likely remained relatively static in their water mass

signatures, or may have faced decreased ventilation. Sedimentary records and modeling results demonstrated the potential for convection-driven formation of NPDW and the onset of an active PMOC during the warm Pliocene due to increased sea surface temperature and higher surface salinities. Notably, these changes occurred as a response to atmospheric changes in the evaporation–precipitation balance, resulting in a weakened or even absent halocline in the western subarctic Pacific (Burls et al., 2017). Since MIS 11 represents the warmest interglacial of the last 500 ka BP, one could infer that a transient weakening of the permanent stratification in the NW Pacific may have occurred and led to an enhanced NPDW ventilation and stronger circulation. In addition,  $\delta^{13}\text{C}$  in NPDW during MIS 13 showed similar or even higher values than MIS 11, in conjunction with LCDW patterns in the Southern Ocean, even though MIS 13 was not a globally pronounced warm stage (Figure 3F and H). Unfortunately, we cannot compare our results with CDW due to the insufficient length of the latter record. These well-mixed water masses during MIS 11 and to some extent MIS 13 suggest that this may not be a norm for common interglacial periods during the Late Quaternary. The positive  $\delta^{13}\text{C}$  signature during MIS 11 and 13 might merely reflect global carbon reservoir changes during the Mid-Brunhes Transition, before entering into the increasing amplitude of 100 ka climate cycles (Barth et al., 2018; Raymo et al., 1997).

### **5.3.2. NPIW influence on NW Pacific**

The second principal end-member water mass in the NW Pacific is NPIW, formed in the subarctic Pacific, where fresh and cold intermediate water from the Okhotsk Sea merges with warm and high-nutrient Kuroshio Current from the south, leading the formation of NPIW along the Mixed Water Region between 30 and 45° N, mainly by diapycnal mixing (Talley, 1988; Talley, 1991; Talley, 1993; Talley, 1997; Talley et al., 1995; Talley and Yun, 2001; Yuan and Talley, 1992). Evidence is still controversial as to whether NPIW was better ventilated and/or more extensive in its geographical and depth domain during glacials and therefore may have suppressed the extent of NPDW. Studies based on benthic  $\delta^{13}\text{C}$  indicated a better-ventilated intermediate water mass during the LGM than the Holocene in the North Pacific, which also extended to greater water depths of around 2000 m, compared to the more restricted lower limit of around 1200 m under modern conditions (e.g., Duplessy et al., 1988; Keigwin, 1987; Keigwin et al., 1992). Knudson and Ravelo (2015) inferred from a 1.2 Ma-long record from the Bering Sea that NPIW ventilation was closely related to the closure history of the Bering Strait, with the caveat that the acquired record is based mostly on endobenthic species (*U.*

*peregrina*) data to bottom water  $\delta^{13}\text{C}$ . To better characterize the NPDW ventilation history beyond the last termination and its interaction with the mid-depth water column, we compare our record to Site U1342 (Bering Sea, 818 m water depth; Knudson and Ravelo, 2015) bathed in NPIW during at least most glacial episodes.

Overall, the  $\delta^{18}\text{O}$  and  $\delta^{13}\text{C}$  signals show a clear disjunction of the two water masses in both records, indicating a consistent relatively strong separation between NPDW and NPIW over the last 540 ka (Figure 3 A, B, E and F). However,  $\delta^{13}\text{C}$  signals during MIS1 to 5 in NPDW show a comparable pattern to NPIW, with a non-apparent glacial-interglacial cycle pattern (Figure 3E and F). The two  $\delta^{13}\text{C}$  records also cover a similar values range between  $\sim -0.5\text{‰}$  to  $\sim 0.2\text{‰}$  during this period. Although CDW can be assumed to be the major contributor to NPDW from the southern source, NPDW might have become more influenced from enhanced NPIW admixing since the Eemian.

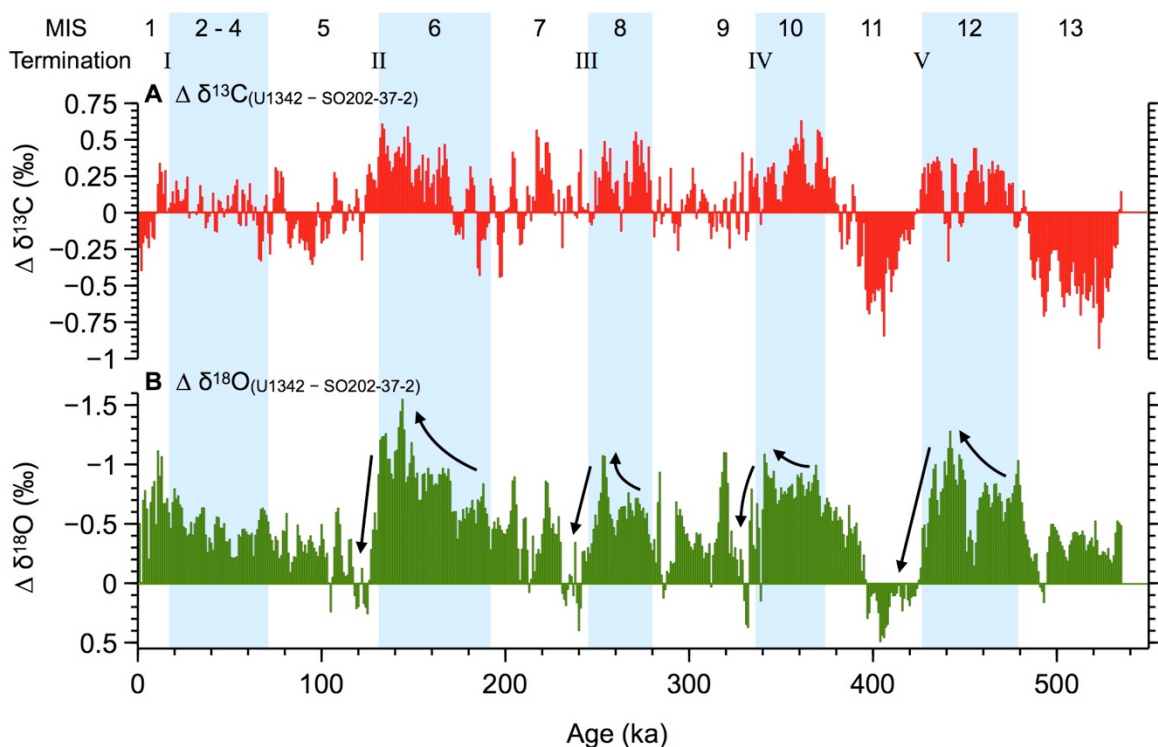


Figure 5. Comparison between Northwest Pacific Deep Water and Bering Sea-sourced Intermediate Water records. (A) Difference between benthic  $\delta^{13}\text{C}$  records of U1342 and SO202-37-2. (B) Difference between benthic  $\delta^{18}\text{O}$  records of U1342 and SO202-37-2. All records were resampled in 1 ka spacing with linear interpolation between data points before subtraction. For resampling the AnalySeries program was used (Paillard et al., 1996). Light blue bars mark glacial intervals.

Although the two water masses NPDW and NPIW reflect slightly inconsistent signals in  $\delta^{18}\text{O}$ , their differences show distinct, rapid shifts from glacial to interglacial transition (Figure 5B, reverse axis), while the respective buildup of higher values indicating stronger separation

is more gradual, in line with slower glacial inceptions over the past 540 ka BP. Higher  $\Delta\delta^{18}\text{O}$  ( $\delta^{18}\text{O}$  at Site U1342 minus  $\delta^{18}\text{O}$  at SO202-37-2) would indicate stronger stratification, and vice versa. The general, relatively persistent curve pattern reveals a mostly pronounced stratification between NPIW and NPDW over the last 540 kyr. A gradually increasing stratification through all glacial towards full glacial conditions is also observed. During terminations II, III, IV and V, however, repeated rapid  $\Delta\delta^{18}\text{O}$  decline to nearly homogenous values occur, with the exception of Termination I (Figure 5B). Such sudden convergence between the two water masses as indicated by minimal offsets in  $\Delta\delta^{18}\text{O}$  might infer a short-term breakdown of the mid-depth to deep water mass stratification during terminations, and a subsequent but brief higher homogenization during peak interglacial intervals (Figure 5B).

Furthermore, deep, aged NPDW would yield lower  $\delta^{13}\text{C}$  signals and thus, lower/higher  $\Delta\delta^{13}\text{C}$  could indicate stronger/weaker ventilation. However, the rapid stratification breakdown that is observed in  $\Delta\delta^{18}\text{O}$  is not as strongly reflected in  $\Delta\delta^{13}\text{C}_{(\text{U1342} - \text{SO202-37-2})}$  (Figure 5A). Principal ventilation remained weak and the changes in general were not as clear during the last four terminations. However, during MIS 10 to 13, a distinct curve pattern is clearly observed in  $\Delta\delta^{13}\text{C}$  with negative values during interglacial and positive values in glacial phases, indicating potentially more active overturning and ventilation during interglacials and a more stagnant deep-water mass during glacials in NPDW. Today, the subarctic Pacific is isolated from the mixed layer downward by a distinct salinity gradient (halocline) resulting from an excess precipitation to low evaporation rate at the surface (Warren, 1983). Different processes may control salinity changes related to the intensity of the subarctic Pacific halocline. Surface salinity would mainly be influenced by the moisture flux from the East Asian monsoon and the latitudinal shifts of more salty-subtropical water, directly related to the atmospheric hydrological cycle. Models observation also show the importance of the moisture transport associated with monsoon to the North Pacific (Emile-Geay et al., 2003; Kiefer, 2010). In a weakening East Asian monsoon, moisture transport reduces, leading to an increase in NW Pacific surface salinity, and thus, surface waters are dense enough to sink. This scenario may explain the rapid breakdown of the halocline during the last four terminations. However, based on record from the Chinese Loess Plateau, MIS 11 and 13 had undergone a strong East Asian summer monsoon (e.g., Guo et al., 1998). This means the monsoon-related fresh water supply was not the main trigger of the increased salinity during termination V. Other monsoon records and model simulations suggested that the Pacific during MIS 13 was in a La Niña-like condition and this favored the strong East Asian summer monsoon (Karami et al., 2015; Lu et al., 2020).

This observation would be in line with own studies from the NW Pacific based on Mg/Ca-reconstructed sea surface temperatures, which also suggested that La Niña-like condition enhanced the Kuroshio Current strength and were transported further north (Jacobi et al., in prep.). Under such a condition of more laterally expanded subtropical water masses, higher salinity water could reach further north and possibly affect the strength of the halocline.

In contrast to the modern situation, several studies and models based proposed a deep water formation or a deep Pacific meridional overturning circulation (PMOC) during the last glacial termination as well as the warmer-than-present period the Pliocene (Burls et al., 2017; Lund et al., 2011; Menviel et al., 2012; Okazaki et al., 2010; Rae et al., 2020; Rae et al., 2014). Based on our  $\Delta\delta^{18}\text{O}$  record, the weakening of the deep stratification happened precisely during the terminations II to V. Moreover, our  $\delta^{13}\text{C}$  gradient data shows a sufficiently ventilated interglacial NPDW, which supports the notion of a sustained, moderate deep PMOC during deglacial and warm intervals.

#### **5.4. Conclusions**

A new reconstruction of variations in NPDW signatures related to ventilation and the overturning circulation since MIS 13 was acquired, based on stable isotopes changes measured on monospecific benthic foraminifera (*Cib. wuellerstorfi*) from the deep NW Pacific. This record provides information on the ventilation history of NPDW in relation to its source water masses. The close correspondence and coupling of  $\delta^{13}\text{C}$  between NPDW and CDW confirms a persistent southern source for PDW, while long-term  $\Delta\delta^{13}\text{C}$  variations suggested changes in CDW circulation strength, entering into the North Pacific. On the other hand, observed  $\delta^{18}\text{O}$  differences between NPDW and NPIW can be taken to assume transient breakdowns of the mid-depth to deep physical stratification during Terminations II to V. Similar evidence for related changes in chemical characteristics related to ventilation were not clearly observed, suggesting NPDW was persistently weakly ventilated in general. However, during MIS 10 and 13, calculated mid-depth to deep carbon isotope gradients expressed as  $\Delta\delta^{13}\text{C}$  suggest a switch from strong ventilation in NPDW during warm intervals to better ventilated NPIW in cold intervals. Our findings further affirm the subarctic Pacific allowed for the persistence of a vast carbon reservoir under the stagnant deep ocean during glacials and for becoming a source for carbon raising atmospheric  $\text{CO}_2$  via deep water upwelling and mid-depth to deep homogenization during glacial terminations and interglacials. Given this oceanic setting, a

collapse of the halocline and rapid ocean ventilation during terminations could release significant quantities of CO<sub>2</sub> to the atmosphere from the NW Pacific.

## 5.5. Data Availability

The data used and analyzed during this study are/will be available on Pangaea and/or from the corresponding author or project PI on reasonable request.

## 5.6. References

- Barth, A.M., Clark, P.U., Bill, N.S., He, F. and Pisias, N.G., 2018. Climate evolution across the Mid-Brunhes Transition. *Clim. Past*, 14(12): 2071-2087.
- Broecker, W.S., Peng, T.-H. and Engh, R., 1980. Modeling the carbon system. *Radiocarbon*, 22(3): 565-598.
- Burls, N.J., Fedorov, A.V., Sigman, D.M., Jaccard, S.L., Tiedemann, R. and Haug, G.H., 2017. Active Pacific meridional overturning circulation (PMOC) during the warm Pliocene. *Science Advances*, 3(9): e1700156.
- Duplessy, J., Shackleton, N., Fairbanks, R., Labeyrie, L., Oppo, D. and Kallel, N., 1988. Deepwater source variations during the last climatic cycle and their impact on the global deepwater circulation. *Paleoceanography*, 3(3): 343-360.
- Duplessy, J.-C., Shackleton, N.J., Matthews, R.K., Prell, W., Ruddiman, W.F., Caralp, M. and Hendy, C.H., 1984. 13C record of benthic foraminifera in the last interglacial ocean: implications for the carbon cycle and the global deep water circulation. *Quaternary Research*, 21(2): 225-243.
- Emile-Geay, J., Cane, M.A., Naik, N., Seager, R., Clement, A.C. and van Geen, A., 2003. Warren revisited: Atmospheric freshwater fluxes and “Why is no deep water formed in the North Pacific”. *Journal of Geophysical Research: Oceans*, 108(C6).
- Ford, H.L. and Raymo, M.E., 2020. Regional and global signals in seawater  $\delta^{18}O$  records across the mid-Pleistocene transition. *Geology*, 48(2): 113-117.
- Galbraith, E.D., Jaccard, S.L., Pedersen, T.F., Sigman, D.M., Haug, G.H., Cook, M., Southon, J.R. and Francois, R., 2007. Carbon dioxide release from the North Pacific abyss during the last deglaciation. *Nature*, 449(7164): 890-893.
- Gebhardt, H., Sarnthein, M., Grootes, P.M., Kiefer, T., Kuehn, H., Schmieder, F. and Röhl, U., 2008. Paleonutrient and productivity records from the subarctic North Pacific for Pleistocene glacial terminations I to V. *Paleoceanography*, 23(4).
- Gong, X., Lembke-Jene, L., Lohmann, G., Knorr, G., Tiedemann, R., Zou, J. and Shi, X., 2019. Enhanced North Pacific deep-ocean stratification by stronger intermediate water formation during Heinrich Stadial 1. *Nature communications*, 10(1): 1-8.
- Gray, W., Rae, J., Wills, R., Shevenell, A., Taylor, B., Burke, A., Foster, G. and Lear, C., 2018. Deglacial upwelling, productivity and CO<sub>2</sub> outgassing in the North Pacific Ocean, *Nat. Geosci.*, 11, 340–344. *Nature Geoscience*.
- Gray, W.R., Wills, R.C., Rae, J.W., Burke, A., Ivanovic, R.F., Roberts, W.H., Ferreira, D. and Valdes, P.J., 2020. Wind-driven evolution of the North Pacific subpolar gyre over the last deglaciation. *Geophysical Research Letters*, 47(6): e2019GL086328.
- Guo, Z., Liu, T., Fedoroff, N., Wei, L., Ding, Z., Wu, N., Lu, H., Jiang, W. and An, Z., 1998. Climate extremes in loess of China coupled with the strength of deep-water formation in the North Atlantic. *Global and Planetary Change*, 18(3-4): 113-128.

- Hall, I.R., McCave, I.N., Shackleton, N.J., Weedon, G.P. and Harris, S.E., 2001. Intensified deep Pacific inflow and ventilation in Pleistocene glacial times. *Nature*, 412(6849): 809-812.
- Herguera, J., Jansen, E. and Berger, W., 1992. Evidence for a bathyal front at 2000-M depth in the glacial Pacific, based on a depth transect on Ontong Java Plateau. *Paleoceanography*, 7(3): 273-288.
- Karami, M., Herold, N., Berger, A., Yin, Q. and Muri, H., 2015. State of the tropical Pacific Ocean and its enhanced impact on precipitation over East Asia during Marine Isotopic Stage 13. *Climate dynamics*, 44(3): 807-825.
- Keigwin, L., 1987. North Pacific deep water formation during the latest glaciation. *Nature*, 330(6146): 362-364.
- Keigwin, L., Jones, G. and Froelich, P., 1992. A 15,000 year paleoenvironmental record from Meiji Seamount, far northwestern Pacific. *Earth and Planetary Science Letters*, 111(2-4): 425-440.
- Keigwin, L.D., 1998. Glacial-age hydrography of the far northwest Pacific Ocean. *Paleoceanography*, 13(4): 323-339.
- Kiefer, T., 2010. When still waters ran deep. *Science*, 329(5989): 290-291.
- Knudson, K.P. and Ravelo, A.C., 2015. Enhanced subarctic Pacific stratification and nutrient utilization during glacials over the last 1.2 Myr. *Geophysical Research Letters*, 42(22): 9870-9879.
- Lisiecki, L.E. and Raymo, M.E., 2005. A Pliocene-Pleistocene stack of 57 globally distributed benthic  $\delta^{18}\text{O}$  records. *Paleoceanography*, 20(1).
- Lu, H., Yin, Q., Jia, J., Xia, D., Gao, F., Lyu, A., Ma, Y. and Yang, F., 2020. Possible link of an exceptionally strong East Asian summer monsoon to a La Niña-like condition during the interglacial MIS-13. *Quaternary Science Reviews*, 227: 106048.
- Lund, D.C. and Mix, A.C., 1998. Millennial-scale deep water oscillations: Reflections of the North Atlantic in the deep Pacific from 10 to 60 ka. *Paleoceanography*, 13(1): 10-19.
- Lund, D.C., Mix, A.C. and Southon, J., 2011. Increased ventilation age of the deep northeast Pacific Ocean during the last deglaciation. *Nature Geoscience*, 4(11): 771-774.
- Lutze, G. and Thiel, H., 1989. Epibenthic foraminifera from elevated microhabitats; *Cibicides wuellerstorfi* and *Planulina ariminensis*. *The Journal of Foraminiferal Research*, 19(2): 153-158.
- Matsumoto, K., Oba, T., Lynch-Stieglitz, J. and Yamamoto, H., 2002. Interior hydrography and circulation of the glacial Pacific Ocean. *Quaternary Science Reviews*, 21(14-15): 1693-1704.
- Max, L., Lembke-Jene, L., Riethdorf, J.-R., Tiedemann, R., Nürnberg, D., Kühn, H. and Mackensen, A., 2014. Pulses of enhanced North Pacific Intermediate Water ventilation from the Okhotsk Sea and Bering Sea during the last deglaciation. *Climate of the Past*, 10(2): 591-605.
- Menviel, L., Timmermann, A., Timm, O.E., Mouchet, A., Abe-Ouchi, A., Chikamoto, M., Harada, N., Ohgaito, R. and Okazaki, Y., 2012. Removing the North Pacific halocline: Effects on global climate, ocean circulation and the carbon cycle. *Deep Sea Research Part II: Topical Studies in Oceanography*, 61: 106-113.
- Mix, A., Pisias, N., Zahn, R., Rugh, W., Lopez, C. and Nelson, K., 1991. Carbon 13 in Pacific Deep and Intermediate Waters, 0-370 ka: Implications for ocean circulation and Pleistocene CO<sub>2</sub>. *Paleoceanography*, 6(2): 205-226.
- Mix, A.C., Pisias, N.G., Rugh, W., Wilson, J., Morey, A. and Hagelberg, T., 1995. Benthic foraminifer stable isotope record from Site 849 (0-5 Ma): Local and global climate changes.

- Okazaki, Y., Timmermann, A., Menviel, L., Harada, N., Abe-Ouchi, A., Chikamoto, M., Mouchet, A. and Asahi, H., 2010. Deepwater formation in the North Pacific during the last glacial termination. *Science*, 329(5988): 200-204.
- Paillard, D., Labeyrie, L. and Yiou, P., 1996. Macintosh program performs time-series analysis. *Eos, Transactions American Geophysical Union*, 77(39): 379-379.
- Rae, J.W.B., Gray, W.R., Wills, R.C.J., Eisenman, I., Fitzhugh, B., Fotheringham, M., Littley, E.F.M., Rafter, P.A., Rees-Owen, R., Ridgwell, A., Taylor, B. and Burke, A., 2020. Overturning circulation, nutrient limitation, and warming in the Glacial North Pacific. *Science Advances*, 6(50): eabd1654.
- Rae, J.W.B., Sarnthein, M., Foster, G.L., Ridgwell, A., Grootes, P.M. and Elliott, T., 2014. Deep water formation in the North Pacific and deglacial CO<sub>2</sub> rise. *Paleoceanography*, 29(6): 645-667.
- Raymo, M., Oppo, D. and Curry, W., 1997. The mid-Pleistocene climate transition: A deep sea carbon isotopic perspective. *Paleoceanography*, 12(4): 546-559.
- Riethdorf, J.R., Max, L., Nürnberg, D., Lembke-Jene, L. and Tiedemann, R., 2013. Deglacial development of (sub) sea surface temperature and salinity in the subarctic northwest Pacific: Implications for upper-ocean stratification. *Paleoceanography*, 28(1): 91-104.
- Schlitzer, R., 2015. Ocean data view. 2018. Available: [odv.awi.de](http://odv.awi.de).
- Schmittner, A., Bostock, H.C., Cartapanis, O., Curry, W.B., Filipsson, H.L., Galbraith, E.D., Gottschalk, J., Herguera, J.C., Hoogakker, B. and Jaccard, S.L., 2017. Calibration of the carbon isotope composition ( $\delta^{13}\text{C}$ ) of benthic foraminifera. *Paleoceanography*, 32(6): 512-530.
- Talley, L.D., 1988. Potential vorticity distribution in the North Pacific. *Journal of Physical Oceanography*, 18(1): 89-106.
- Talley, L.D., 1991. An Okhotsk Sea water anomaly: implications for ventilation in the North Pacific. *Deep Sea Research Part A. Oceanographic Research Papers*, 38: S171-S190.
- Talley, L.D., 1993. Distribution and formation of North Pacific intermediate water. *Journal of Physical Oceanography*, 23(3): 517-537.
- Talley, L.D., 1997. North Pacific Intermediate Water transports in the mixed water region. *Journal of physical oceanography*, 27(8): 1795-1803.
- Talley, L.D., 2013. Closure of the global overturning circulation through the Indian, Pacific, and Southern Oceans: Schematics and transports. *Oceanography*, 26(1): 80-97.
- Talley, L.D., Nagata, Y., Fujimura, M., Iwao, T., Kono, T., Inagake, D., Hirai, M. and Okuda, K., 1995. North Pacific intermediate water in the Kuroshio/Oyashio mixed water region. *Journal of Physical Oceanography*, 25(4): 475-501.
- Talley, L.D. and Yun, J.-Y., 2001. The role of cabbeling and double diffusion in setting the density of the North Pacific Intermediate Water salinity minimum. *Journal of Physical Oceanography*, 31(6): 1538-1549.
- Ullermann, J., Lamy, F., Ninnemann, U., Lembke-Jene, L., Gersonde, R. and Tiedemann, R., 2016. Pacific-Atlantic Circumpolar Deep Water coupling during the last 500 ka. *Paleoceanography*, 31(6): 639-650.
- Warren, B.A., 1983. Why is no deep water formed in the North Pacific? *Journal of Marine Research*, 41(2): 327-347.
- Williams, T.J., Hillenbrand, C.D., Piotrowski, A.M., Allen, C.S., Frederichs, T., Smith, J.A., Ehrmann, W. and Hodell, D.A., 2019. Paleocirculation and ventilation history of Southern Ocean sourced deep water masses during the last 800,000 years. *Paleoceanography and Paleoclimatology*, 34(5): 833-852.
- Yuan, X. and Talley, L.D., 1992. Shallow salinity minima in the North Pacific. *Journal of physical oceanography*, 22(11): 1302-1316.



Zahn, R. and Mix, A.C., 1991. Benthic foraminiferal  $\delta^{18}\text{O}$  in the ocean's temperature-salinity-density field: Constraints on Ice Age thermohaline circulation. *Paleoceanography*, 6(1): 1-20.

Zahn, R., Pedersen, T.F., Bornhold, B.D. and Mix, A.C., 1991. Water mass conversion in the glacial subarctic Pacific ( $54^\circ\text{ N}$ ,  $148^\circ\text{ W}$ ): Physical constraints and the benthic-planktonic stable isotope record. *Paleoceanography*, 6(5): 543-560.

## 5.7. Supplementary

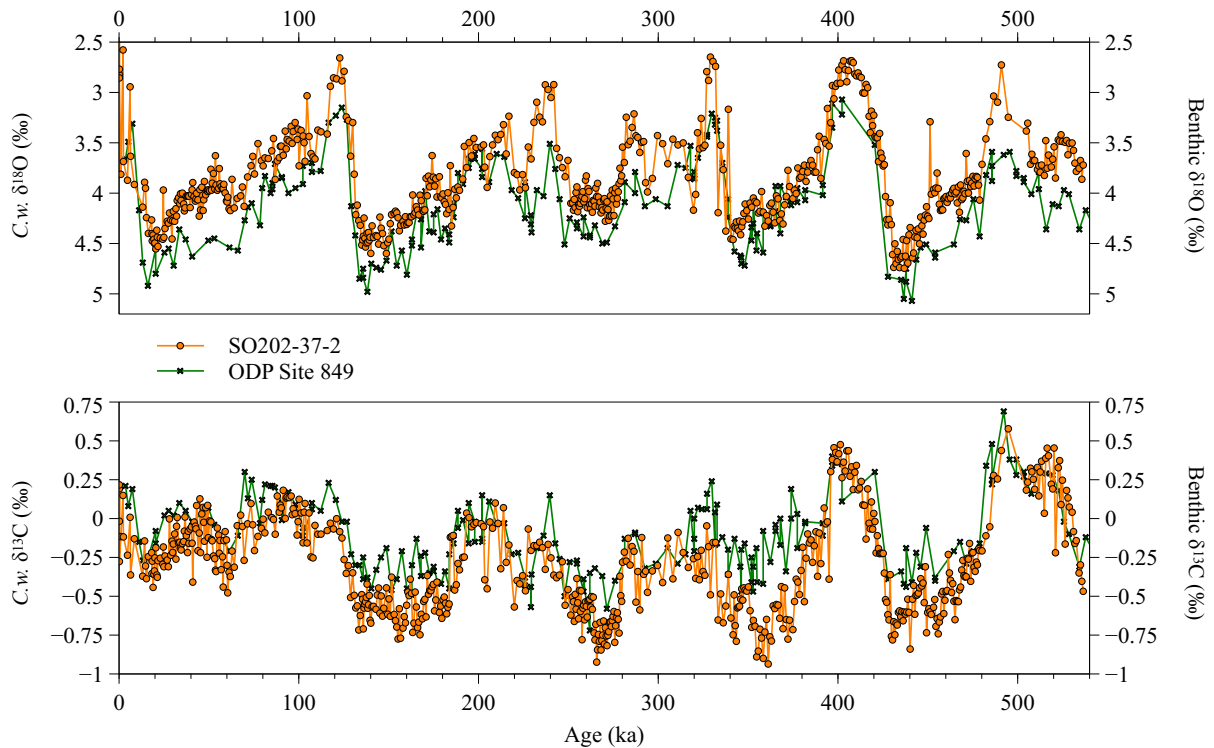
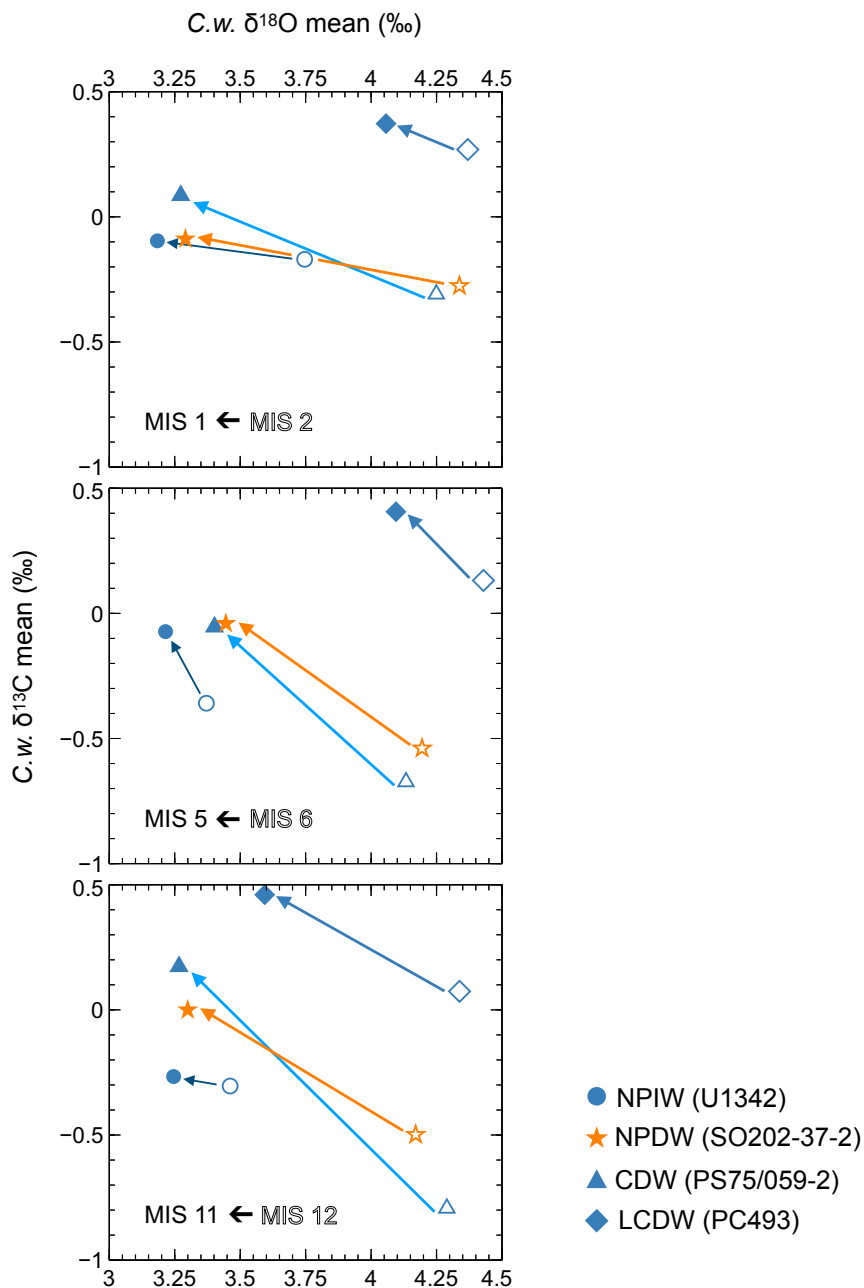


Figure S1. Benthic stable isotopes records of ODP Site 849 which partially measured on *U. peregrina* (green lines; Mix et al., 1995) and SO202-37-2 which measured solely on *C. wuellerstorfi* (orange lines; this study).

Additional figure for Result and Discussion in later version(s):



*Terminations which entering the interglacials as warm as present*

- little connection between LCDW and the other three water masses
- A trend of smaller gradient towards present, both in  $\delta^{18}\text{O}$  and  $\delta^{13}\text{C}$
- Connection between NPIW, NPDW and CDW are closer after MBT observed from  $\delta^{13}\text{C}$  gradient
- Clearly showing deep PMOC was well-ventilated than NPIW during MIS 11c than the others

## 6. Quantifying calcium carbonate and organic carbon content in marine sediments from XRF-scanning spectra with a machine learning approach

An-Sheng Lee <sup>1,2,†</sup> and Weng-Si Chao <sup>\*,3,†</sup>, Sofia Ya Hsuan Liou <sup>\*,2</sup>, Ralf Tiedemann <sup>3</sup>, Bernd Zolitschka <sup>1</sup>, Lester Lembke-Jene <sup>3</sup>

<sup>1</sup> University of Bremen, Institute of Geography, Bremen, Germany

<sup>2</sup> National Taiwan University, Department of Geosciences and Research Center for Future Earth, Taipei, Taiwan

<sup>3</sup> Alfred-Wegener-Institut Helmholtz-Zentrum für Polar- und Meeresforschung, Bremerhaven, Germany

\*Corresponding authors: yhliou@ntu.edu.tw, weng-si.chao@awi.de

† These two authors contributed equally to this work.

This article has been published on *Scientific Reports*; Citation: Lee, AS., Chao, WS., *et al.* Quantifying calcium carbonate and organic carbon content in marine sediments from XRF-scanning spectra with a machine learning approach. *Sci Rep* **12**, 20860 (2022). <https://doi.org/10.1038/s41598-022-25377-x>

Received: 26 September 2022; Accepted: 29 November 2022

Published online: 02 December 2022

### Abstract

Geochemical variations of sedimentary records contain vital information for understanding paleoenvironment and paleoclimate. However, to obtain quantitative data in the laboratory is laborious, which ultimately restricts the temporal and spatial resolution. Quantification based on fast-acquisition and high-resolution provides a potential solution but is restricted to qualitative X-ray fluorescence (XRF) core scanning data. Here, we apply machine learning (ML) to advance the quantification progress and target calcium carbonate (CaCO<sub>3</sub>) and total organic carbon (TOC) for quantification to test the potential of such an XRF-ML approach. Raw XRF spectra are used as input data instead of software-based extraction of elemental intensities to avoid bias and increase information. Our dataset comprises Pacific and Southern

Ocean marine sediment cores from high- to mid-latitudes to extend the applicability of quantification models from a site-specific to a multi-regional scale. ML-built models are carefully evaluated with a training set, a test set and a case study. The acquired ML-models provide better results with  $R^2$  of 0.96 for  $\text{CaCO}_3$  and 0.78 for TOC than conventional methods. In our case study, the ML-performance for TOC is comparably lower but still provides potential for future optimization. Altogether, this study allows to conveniently generate high-resolution bulk chemistry records without losing accuracy.

## 6.1. Introduction

Over the last decades, we have been experiencing the rapid development of machine learning (ML; Alpaydin, 2014; Jordan and Mitchell, 2015). It has been employed in different domains and tasks to improve performance by leveraging the collected data. Although ML has been transformative in many fields, there is still a lack of knowledge and applications in traditional science. In this study, we aim to improve this process by introducing ML to quantify and predict oceanographical data from marine sediments.

Marine sediments are prime recorders of Earth's environmental history through the steady accumulation of biogenic and lithogenic detritus. Qualitative and quantitative analyses of sedimentary components and their chemical properties are essential in providing information for reconstructing paleoclimatic and paleoceanographic changes from annual to orbital, and even tectonic timescales (Schulz and Zabel, 2006). Calcium carbonate ( $\text{CaCO}_3$ ) as a principal biogenic component of pelagic marine sediments and acts as a major factor in the oceanic carbon system, which in turn regulates natural atmospheric  $\text{CO}_2$  variations to a large extent (Archer and Maier-Reimer, 1994). Determination of the  $\text{CaCO}_3$  content in weight percent (wt%) is commonly calculated from the difference between total carbon content and total organic carbon content (TOC; see Materials and methods). However, laboratory analyses are time- and labor-consuming, restricting the attainable temporal and spatial resolution.

With the advantages of high-resolution ( $\geq 100\mu\text{m}$ ), non-destructive and rapid measurements, X-ray fluorescence (XRF) core scanning techniques may lift the restriction of resolution. An opened 1 m-long marine sediment core can be scanned from 1 to 3 hours, depending on scanning settings, to obtain elemental profiles with a 1 cm spatial resolution and related replicates. This method has contributed significantly to systematically recording high-resolution geochemical profiles of sediments. Moreover, its applicability covers all kinds of

natural archives, such as soft sediments, speleothems, corals, rocks and tree sections (Croudace et al., 2019). Despite these advantages, the method suffers of one major disadvantage: it only provides semi-quantitative measurements. The non-linear relation between quantitative and XRF measurements is caused by physical and matrix effects as well as a general lack of control on measurement geometry (Croudace et al., 2006; Tjallingii et al., 2007; Weltje et al., 2015). As a result, quantification of XRF measurements is in high demand.

There are several stepstones on the path to quantifying XRF measurements of sediment cores. Several attempts of quantifying elemental concentrations from the XRF intensity data via direct regression (i.e., Ordinary Squares Regression) have achieved success (e.g., Böning et al., 2007; Croudace et al., 2006; Jansen et al., 1998). Weltje and Tjallingii (2008) improved the quantification by introducing the additive log-ratio and the major axis regression to the workflow. The relation between elemental concentration and XRF elemental intensities is carefully dealt with by using detailed mathematic derivation (XRF spectrometry theory and statistical theory of compositional data) and empirical tests. However, the power of quantification is limited to “relative” element concentrations, which is constrained by the element assemblage as input. As a follow-up, Weltje et al. (2015) proposed a next level of improvement to increase the accuracy and quantify “absolute” elemental concentrations. They modified the previous workflow (Weltje and Tjallingii, 2008) by implementing centred log-ratios and Partial Least Square Regression. The idea of covariance between matrix elements is hence included. Furthermore, it introduces cross-validation (CV) to more rigorously evaluate the model’s predictive power. To make this workflow easier to be applied, the software Xelerate was developed supported by a statistically robust sampling scheme (<http://www.mennobloemsma.nl/software.php>).

Based on thriving computing power and ML techniques (Alpaydin, 2014; Jordan and Mitchell, 2015), ML applications in the field of geochemical research have been growing (e.g., Bolton et al., 2020; Kaboth-Bahr et al., 2018; Ön and Özeren, 2019). Thus, a further stepstone of quantifying XRF measurements can be achieved. First, the application should not be limited to element concentration since there are other proxies, which are of scientific interest and will benefit from high resolution, such as grain size, terrigenous input, opal, CaCO<sub>3</sub> and organic matter. Second, the elemental intensity to be quantified can be substituted by the emitted fluorescence energy and wavelength spectrum (in short: the XRF spectrum, i.e., the raw data), which records comprehensive information of scanned sediments but is a jump of two orders of magnitude in data dimension. The commonly used elemental intensity is generated by

converting the XRF spectrum using data processing software. Fine-tuning of the related software settings needs care and experience. To produce semi-quantitative data rapidly, this procedure often receives less attention than necessary. Consequently, using the XRF spectra avoids this manual bias, especially when dealing with a high quantity of sediment cores. Moreover, most of the XRF scanners cannot determine the lighter elements (atomic number < 11, such as carbon) at the low end of the energy spectrum. ML techniques may overcome this conventional XRF limitation. Third, the logarithmic data space can be extended to an infinite non-linearity space efficiently by a mathematical trick, the kernel function (Abu-Mostafa et al., 2012). It is expected to give learning algorithms higher capability to cope with the non-linear relation between semi-quantitative XRF and desired quantitative elemental measurements. Fourth, the application of a model was often considered as site- or even core-specific. Having a larger quantity of data from many cores, a kernelized learning algorithm may lift this limitation and builds a large regional quantification model, which smoothens the process of acquiring high-resolution quantitative data.

In this study, we propose an approach of building models quantifying two commonly used geochemical proxies ( $\text{CaCO}_3$  and TOC contents) from XRF spectra. This involves ML techniques and high-performance computing applied to marine sediment cores that cover multiple regions from the northern and southern pelagic Pacific Ocean (Figure 1). Two preprocessing algorithms, Principal Component Analysis (PCA) and Non-negative Matrix Factorization (NMF) as well as three supervised ML algorithms, Ridge Linear Regression (LR), kernel Support Vector Machine (SVM) and Random Forest (RF), are included for searching the optimal model. The workflow is schematically shown in Figure 2. Hopefully, this will kick-off opportunities to include more measurements covering more extensive applications for quantification, such as measurements of different proxies and scanner types. Meanwhile, all the executive codes are open source. The users can easily adopt and modify these codes for their own study and needs, rather than being restricted to a certain software.

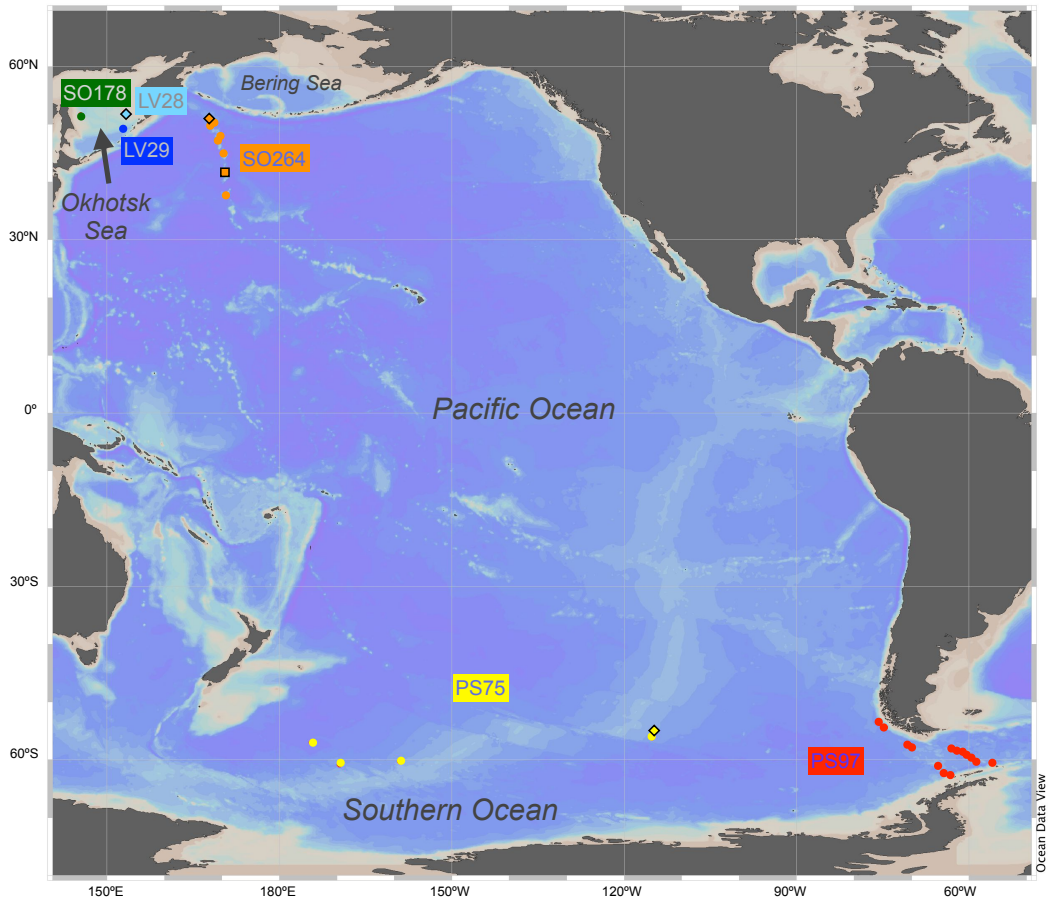


Figure 1. Map of selected pelagic sediment cores, marked by colored dots related to individual and labelled cruises. The orange square represents the pilot test core SO264-15-2. The diamonds represent the cores PS75/056-1, LV28-44-3 and SO264-69-2 used in the case study. Map is created with Ocean Data View 5.6.3 (<https://odv.awi.de/>).

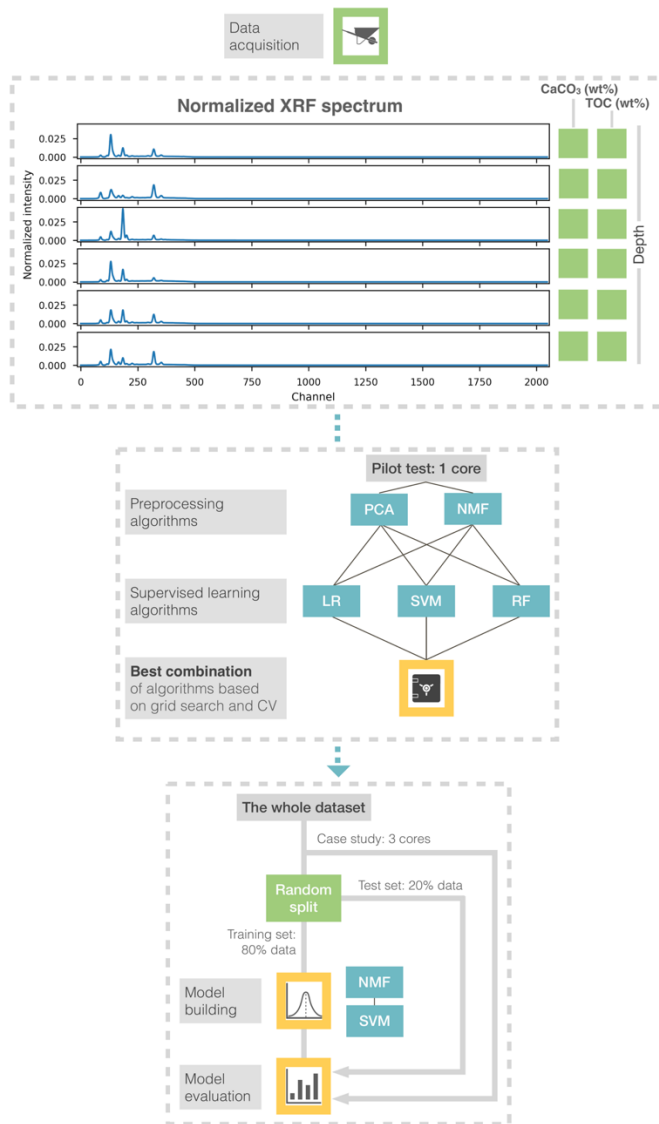


Figure 2. Workflow for the machine learning approach applied to XRF spectra.

## 6.2. Machine Learning: approach and set-up

### 6.2.1. Pilot test

Quantifying the XRF spectra to bulk geochemistry is a regression task carried out by ML algorithms to learn the relation between both data. To find a suitable combination for preprocessing and supervised learning algorithms, the XRF spectra and  $\text{CaCO}_3$  content from one recently retrieved core (SO264-15-2) were selected as pilot data. The dataset is composed of paired available geochemistry data and XRF spectra with corresponding core depth (data amount: 40). We tested two preprocessing algorithms (PCA and NMF) and three supervised learning algorithms LR, SVM and RF. PCA and NMF are commonly applied for source separation, extracting vital information from the data (Cichocki and Phan, 2009; Clifford, 2008;



Févotte and Idier, 2011). SVM has abilities to explore data relations in the infinite non-linear space and tolerate data noise (Chang and Lin, 2011). RF provides a well-regularized learning power in non-linear space based on its tree-based design (Breiman, 2001; Geurts et al., 2006). LR is an L2 regularized Ordinary Least Squares regression (Abu-Mostafa et al., 2012), included as a reference for the performance of the linear algorithm.

The `n_component` parameter for NMF was initially set following the PCA's result (explained variances of principal components). The parameters (alpha for LR, C and gamma for SVM, `max_depth` and `n_estimators` for RF) control the regularization level of the algorithms, which affect under- and over-fitting issues (Müller and Guido, 2016; Pedregosa et al., 2011). There is no universally suitable value for these values. Thus, we intuitively grid searched parameters and found a set of optimal parameters, which builds a model with best performance. Since the data is not noise-free, this grid search was integrated with a 5-fold cross-validation (CV; Abu-Mostafa et al., 2012) to be robust. The score (performance) is presented by an averaged coefficient of determination ( $R^2$ ) in CV.

### **6.2.2. Model training and evaluation**

First, the workflow was specified with the best score from the pilot test. Then the training set, which was split from the whole dataset (random 80% of data points, Figure 3), was used to train our model. The grid search was implemented again for finding optimal parameters, but integrated with 10-fold CV to increase the score's statistic robustness. The final models for quantifying  $\text{CaCO}_3$  and TOC were subsequently built by adopting the optimal parameters. Details of the grid search strategy are provided by Supplementary Material I.

Evaluating their performance in a pristine data subset is essential to understand the models' generalization, i.e., how good our models are in quantifying bulk chemistry from other cores. The test set comprises the data left after partitioning the training set from the whole dataset (Figure 3). Since it is a set of random data, it cannot illustrate a comparison between measurement and prediction for the whole core with uncertainty. In order to rigorously evaluate the models' performance, we used three additional sediment cores with comparable sedimentary facies applying our optimal models for predictions as a case study (Figure 1). During evaluation, the models read the XRF spectra of this subset of data to predict  $\text{CaCO}_3$  and TOC contents. The performance was calculated by  $R^2$ , root mean squared error (RMSE) and the ratio of performance to inter-quartile distance (RPIQ; Bellon-Maurel et al., 2010) between

actual and predicted values. Meanwhile, errors in the test set and case study were used to construct 95% confidence intervals based on the t-distribution. The uncertainty of our models was thus estimated.

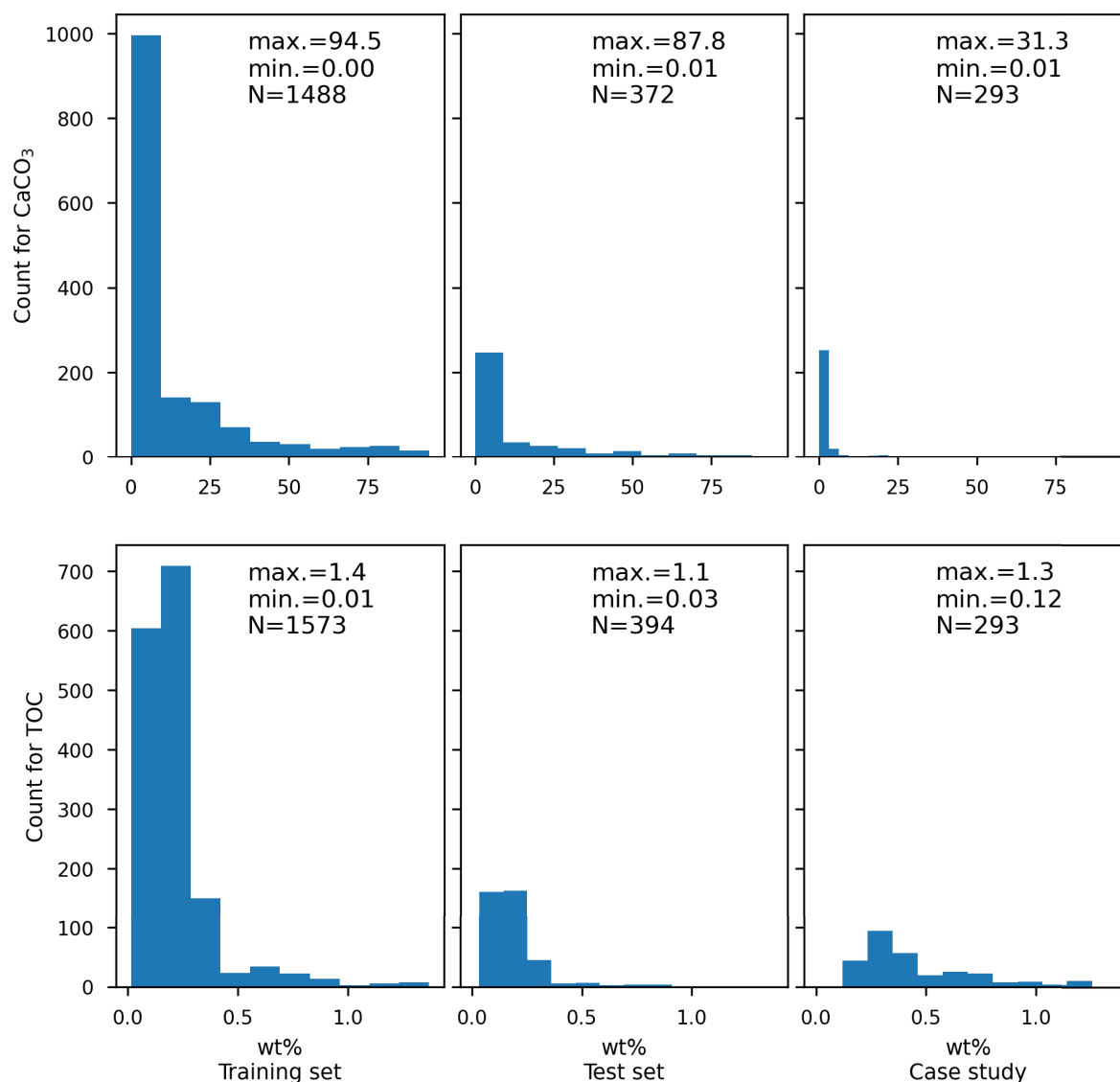


Figure 3. Data distributions of  $\text{CaCO}_3$  and TOC for the training set, test set and case study.

### 6.3. Results: Optimization of machine-learning models, evaluations of test set and case study, quantification of $\text{CaCO}_3$ and TOC

The pilot test shows that the workflow using SVM to learn from the NMF-transformed data provides the most promising results. The linear algorithm (LR) has disadvantages in giving good predictions compared to the SVM workflow. Consequently, the NMF-SVM workflow was carried out for the training set. After grid searching for the parameters, the optimal models

were built using the settings listed in Supplementary Material I. The NMF chained in the optimal models of CaCO<sub>3</sub> and TOC transformed the normalized XRF spectra into fewer features (Figure S4), expected to be vital information and promote the performance of later algorithms.

Table 3. Scores for the optimal models of calcium carbonate (CaCO<sub>3</sub>) and total organic carbon (TOC). Cross-validation (CV) score stands for the learning performance in the training set, which is the mean of R<sup>2</sup> during training iterations. R<sup>2</sup>, 95% confidence interval (CI), root mean square error (RMSE) and ratio of performance to inter-quartile distance (RPIQ) estimate the performance and uncertainty of the optimal models in the test set and case study. CI and RMSE both have wt% as the unit. \*Negative R<sup>2</sup> is considered as 0.

Analyte	Training set CV scores	Test set statistics			Case study statistics			95% CI
		R <sup>2</sup>	RMSE	RPIQ	R <sup>2</sup>	RMSE	RPIQ	
CaCO <sub>3</sub>	0.87	0.96	3.57	4.63	0.61	2.80	0.36	[-6.77, 5.91]
TOC	0.79	0.78	0.07	1.57	0*	0.37	0.91	[-0.54, 0.30]

As conventional methods tend to enhance the accuracy of a model only for training data, they cause a common mistake while evaluating a built model. For example, there are 20 CaCO<sub>3</sub> and 100 XRF measurements in a core. Operators often try to find a regression between these 20 CaCO<sub>3</sub> and corresponding XRF measurements giving the highest R<sup>2</sup>. They hence overestimate the regression's accuracy outside of the training data (20 data points). This is called overfitting in ML tasks (Abu-Mostafa et al., 2012). The model's generalization beyond the training data should be equally important.

Our optimal models were not only evaluated in the training set, estimated in CV scores, but also in the test set and case study, estimated in R<sup>2</sup>, RMSE and RPIQ. Table 1 documents that our models have a good accuracy (CV score and R<sup>2</sup>) for training and test sets, which should exclude the effects of overfitting. The models' performing statistics in the case study behave differently (Table 1). The performance of the CaCO<sub>3</sub> model remains moderate, while the one of the TOC models drops significantly compared to its performance in the test set. The 95% confidence intervals estimate constrained uncertainties of the models, which correspond to the statistics in the data subsets. Due to the implementation of the logarithm, our ML approach gives no negative values, which further reduces the prediction's uncertainty beyond the listed lower confidence interval (Table 1).

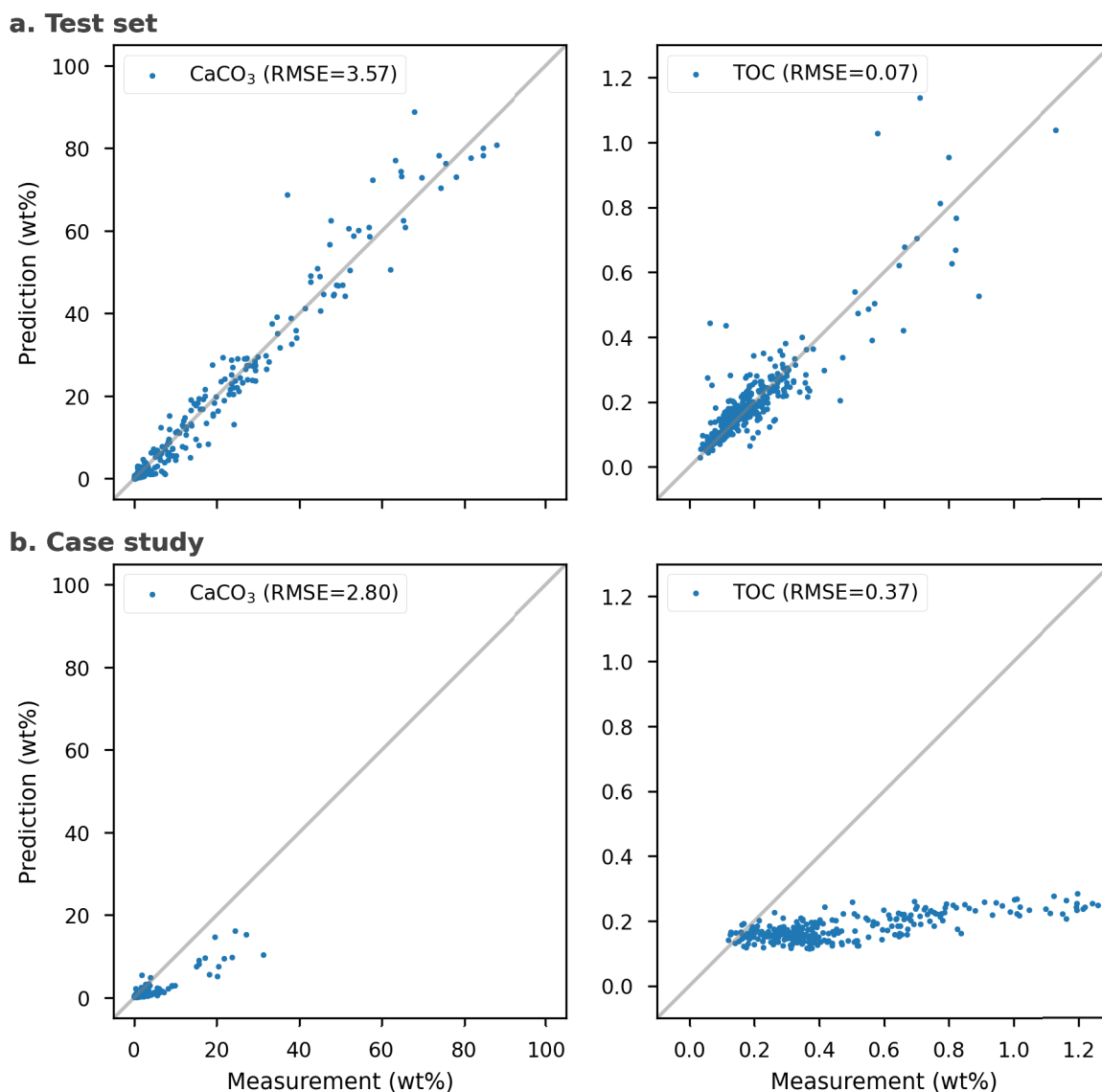


Figure 4. Measured versus predicted  $\text{CaCO}_3$  (left panels) and TOC contents (right panels) in (a) the test set and (b) the case study.

As shown in Figure 4(a), the error in the test set enlarges when the value increases. This is especially true for TOC but remains acceptable. In Figure 4(b) errors expand when compared to the test set. The values of  $R^2$  and RPIQ decrease (cf. Table 1). The TOC predictions became worse in  $R^2$  of two datasets while  $\text{CaCO}_3$  degrades mostly in RPIQ.

The optimal models were implemented to quantify the entire dataset of all cores (i.e., other data without measurements in the same core series of the training and test sets). The total number of data points with bulk geochemistry was increased from <2000 to 57,240, yielding quantified bulk geochemistry data of  $\text{CaCO}_3$  and TOC for those core intervals, which had not been sampled discretely in high-resolution (1 cm; available in Supplementary Material III). In the quantified data, only 410 data points (0.72 %) yield values >100 wt% and no negative

values occurred. Figure 6 illustrates an example for core SO264-55-1 of improved bulk chemistry resolution and surpassing accuracies comparing to the conventional method (XRF-derived proxies).

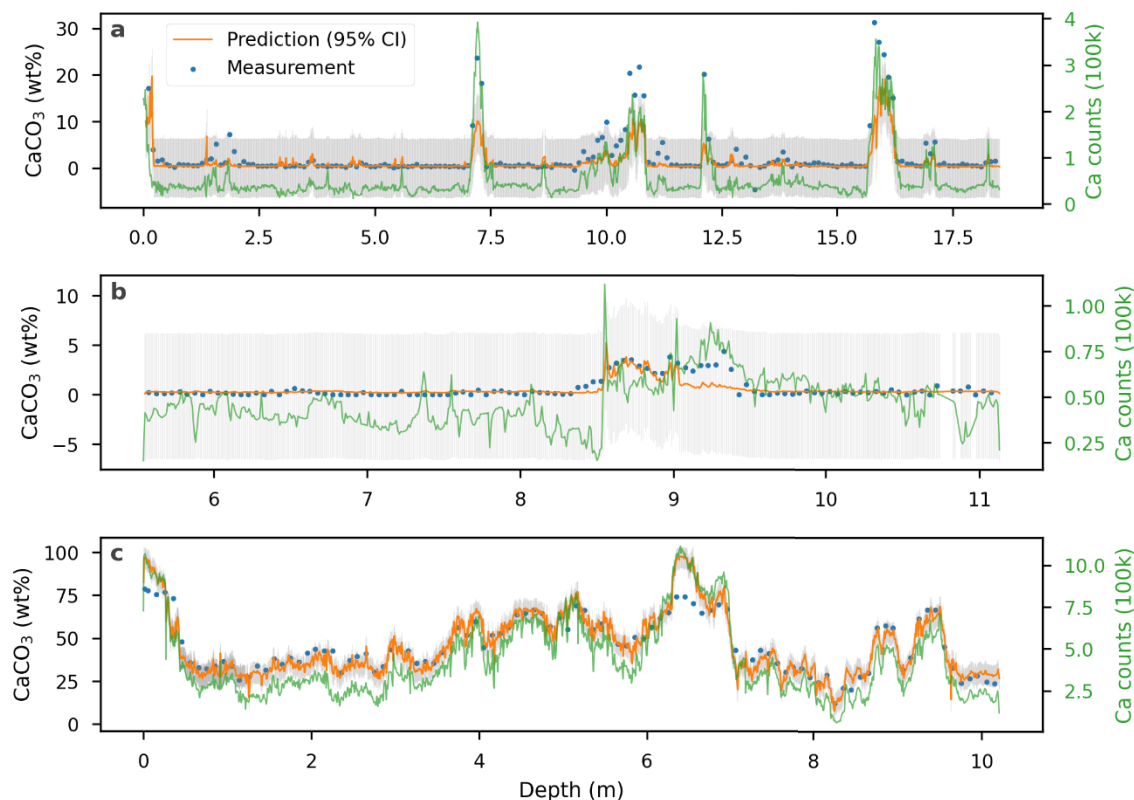


Figure 5. Measured (blue dots) and predicted (orange lines with 95% confident intervals in gray) CaCO<sub>3</sub> contents compared with the commonly applied XRF-derived proxy (Ca counts as green lines) for cores of the case study (a: SO264-69-2, b: LV28-44-3, c: PS75/056-1).

#### 6.4. Discussion: Applications in case study and whole dataset, limitations, strengths

Since the case study used continuous data from one core, the predictions can be displayed vs depth with both the actual measurements and commonly used XRF-derived element data (e.g., software-processed Ca counts, as the conventional method). The goodness of fit for the CaCO<sub>3</sub> model (Table 1) is supported by the close correspondence between actual measurements and predictions (Figure 5). Some extreme values have larger errors in prediction but the performance for moderate values is good. In contrast, the XRF-derived Ca counts show a more unrestrained behavior, in line with some extreme values, but loose accuracy in a general pattern. Thus, the improvement with our ML approach compared to the XRF-derived Ca counts for CaCO<sub>3</sub> predictions is affirmed.

Overall, the CaCO<sub>3</sub> prediction in the case study is comparable to the test set (Figure 4, Table 1), except for RPIQ. The R<sup>2</sup> degraded more than the RMSE, which is due to a smaller variance in the case study compared to the test set. Discussing RMSE is more adequate in this situation since it is a comparison within the same analyte and value scale (0-100 wt%). The normalization in the calculation of R<sup>2</sup> is redundant and biased. As a result, the comparable RMSE and almost unbiased error distribution (Figure 4) guarantee a generalization of the CaCO<sub>3</sub> model. In other words, this approach provides the opportunity to reduce the CaCO<sub>3</sub> content measuring time by applying the model to sediment cores. The drop of RPIQ implies that the skewed distribution in the case study may affect the used metrics, which will require more detailed investigation when including more data. Instead of building quantification models core by core, this approach builds a model for each analyte, quantifying cores in a batch process to increase the involved efficiency. The CaCO<sub>3</sub> model not only shortens the measurement time and the laboratory labor inherent to discrete samples, but also provides an expansion for the use of XRF-scanning spectra.

The TOC performance in the case study was relatively low, compared to that in the test set, indicating the limitation of the generalization of our TOC model. As the debut of studying TOC content directly from XRF spectra, it is an attempt to predict TOC from indirect elemental properties, while carbon itself is beyond the limits of what the scanning detector can measure. Therefore, Bromine (Br) is a commonly applied XRF-derived proxy to estimate marine organic matter (TOC) content (e.g., (Caley et al., 2011; McHugh et al., 2008; Ziegler et al., 2008)). But for the case study, Br has a poor fit to the TOC content (Figure S 5, Supplementary Material II). We consider that our TOC model develops the regression by collecting the behavior of many different elements falling into the scanner's capability. The model is learning from indirect and concealed information instead of directly from "visible" signals of organic matter. The correlation between this indirect information and TOC varies with the environmental setting, such as the source of organic matter as supported by the relatively poor fit of the XRF-derived Br from the scanning setting of 30 kV. Thus, the generalization to the cores outside of our initial dataset becomes challenging. Although the generalization of the TOC model is weak to cores beyond our initial dataset, it fulfills our fundamental expectation providing better quantification and higher resolution for our dataset compared to conventional methods (e.g., Figure 6). The performance in training and test sets gives a R<sup>2</sup> of 0.78 and 0.79 (Table 1). We assume that applying a full sets of energy spectra, this XRF-ML approach could lead to promising results and predictions of relevant elements and proxies.

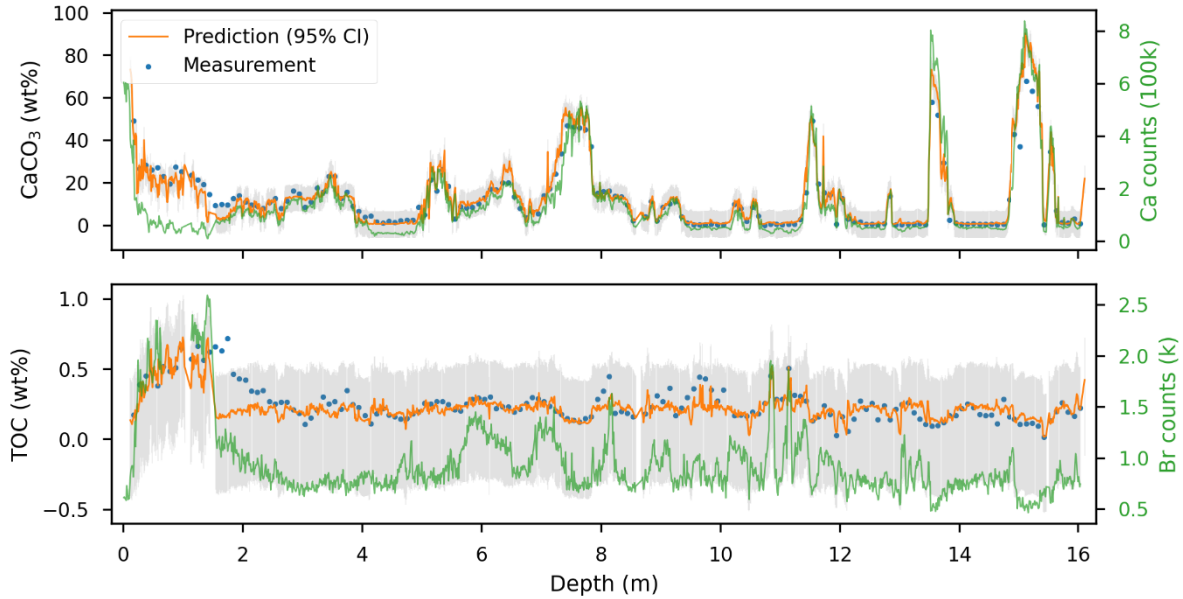


Figure 6. Measured (blue dots) and predicted (orange lines with 95% confident intervals in gray) values for  $\text{CaCO}_3$  and TOC contents in a core from the training set (SO264-55-1). The commonly applied XRF-derived proxies (Ca and Br counts) are marked as green lines.

The evaluation between test set and case study marks a concealed data-snooping issue. The test set, consisting of the data from the same core series with the training set, overestimates the performance of the TOC model. Hence, our separation of data points between training and test sets is insufficient. The splitting process requires a stricter separation by considering core series. Based on our results, data from the same core is suggested to be split into the same subset (e.g., k-fold splitting iteration with non-overlapping groups (Pedregosa et al., 2011)). This more rigorous procedure can be found in speech recognition applications that keep voice data from the same speaker in the same data split, even though the content of the voice record is different (Müller and Guido, 2016).

Regarding the very good performance of our  $\text{CaCO}_3$  model, two possible explanations emerge: First, the direct use of XRF spectra instead of elemental intensities after software processing helps the ML algorithms to learn the information without any bias caused by manual fine-tuning. This fine-tuning of software settings needs sufficient experience to adjust for sediment-property changes. The change of water content or organic matter would need corresponding adjustments of the settings. However, these adjustments are commonly ignored due to the lack of experience or tedious labor when encountering long records, which leads to biased elemental intensities. This explanation is supported by the phenomenon that the uppermost part of core SO264-55-1 (Figure 6) has noticeably biased fitting accuracy compared to the rest of the core for XRF-derived Ca, which was software-processed. This interval could

indicate sediment facies changes or very soft sediment conditions and requires respective software parameter fine tuning, which was not applied in this case. Both models overcome this issue to have consistent accuracy. Secondly, compared to software-processed elemental intensities or ratios, the spectrum provides more hidden information recorded in the entire fluorescence signal (e.g., water content). As a result, after learning from a certain amount of data points covering the entire variation of sediment properties, our XRF-ML models are able to determine unbiased multi-elemental and matrix information. This capability of non-linearity solves an existing gap between non-linear XRF elemental proxies and linear bulk chemistry measurements.

Unlike conventional quantification methods, which build site- or core-specific models (Croudace et al., 2006; Weltje et al., 2015), our approach shows that general models can be constructed accurately for quantifying  $\text{CaCO}_3$  on a larger spatial, regional to basin-wide scale. Thus, a potential demand of repeatedly building and testing traditional regression-based models is eliminated. Eventually, our models could be applied to entire core collections from specified cruises, which cover multiple sectors of e.g., the Pacific Ocean, while significantly reducing the demand of conventional laboratory measurements. With the increased provision of quantitative data by a partially automated process, the temporal and spatial resolution of paleoceanographic and paleoclimatic data can be enhanced significantly.

## **6.5. Guidelines for future applications**

For studies retrieving sediment cores in nearby regions: our  $\text{CaCO}_3$  model is ready to use. No laboratory measurement and high-performance computing is necessary. A common PC with the capability of Python coding is sufficient for adopting our models. For studies featuring cores from other study areas, the model is still worth a trial, but a test run is recommended to evaluate the accuracy. If the model fails or XRF data is acquired from different core scanners, our workflow for building models is well suited for developing own models. For improvement of this first test set of models, such as for future TOC predictions, one should consider using spectra acquired from ideally suited scanner settings, while making sure data from the same core stays in the same subset during the data splitting process. Failure of our model can be related to sediment type, sediment age range, XRF core scanner, X-ray tube and scanning settings. Any major changes of these categories from our dataset might result in notably different XRF spectra and lead to erroneous predictions. The remaining boundary conditions of our dataset are stated in “Materials and methods” section and ready for future applications.



## **6.6. Conclusions**

A new approach is presented by using machine learning (ML) techniques to build models that can quantify  $\text{CaCO}_3$  and TOC contents directly from XRF-scanning-derived spectra. The advantages of the XRF-ML approach are a quick, quantitative, precise and high-resolution data acquisition, while multiple cores can be calculated simultaneously. The use of XRF spectra reduces manual user-generated bias and increases the input information for ML algorithms. The broad data coverage, the power of ML and computing techniques lift the model's limitation off the site-specific scale. This novel quantification of  $\text{CaCO}_3$  and TOC contents and the generalization of optimal models is carefully evaluated in training and test sets as well as a case study. The uncertainty of predictions is estimated in 95% confidence intervals from the test set and the case study.

Further cores retrieved from the extratropical North and South Pacific could be quantified with high-resolution (1 cm), hitherto unattainable due to the high amount of analytical workload involved for discrete sample preparation. We provide guidelines for future applications. To progress our multi-region models towards an even broader temporal and spatial domain, we plan to incorporate more measurements, different core locations, scanner types and settings. Hopefully, this approach brings future studies towards retrieving high-resolution quantitative bulk chemistry without losing accuracy.

## **6.7. Materials and methods**

### **6.7.1. Sediment cores and bulk measurements**

In this study, spectra of 30 XRF-scanned marine sediment cores, including published and unpublished records, together with their corresponding bulk chemistry measurements were examined (in total, 2580 TOC samples and 2517 total carbon content samples; Supplementary Material III). The investigated cores are mostly retrieved from two expeditions: cruise SO264 in the subarctic Northwest Pacific with R/V SONNE in 2018 and cruise PS97 in the central Drake Passage with RV Polarstern in 2016. Another four cores and the case study core were recovered in the Pacific sector of the Southern Ocean during PS75 in 2009/2010. Additional three cores were recovered in the Okhotsk Sea during cruise KOMEX I and KOMEX II with R/V Akademik Lavrentyev in 1998 and cruise SO178 in 2004. The area of all investigated cores is mainly spreading across the high- to mid-latitude Northwest Pacific (37°N-52°N) and

the Pacific sector of the Southern Ocean (53°S-63°S), with a water depth coverage from 1211 to 4853 m. The three cores of the case study are located in the Okhotsk Sea (LV28-44-3; 52°2.5139'N 153°5.949'E; 684 m water depth), the Northwest Pacific (SO264-69-2; 50°30.877'N 167°55.478'E; 3473 m water depth) and the Southern Ocean (PS75/056-1; 55°09.74'S 114°47.31'W; 3581 m water depth).

The investigated cores are dominated by pelagic sediments and mainly consist of calcareous and siliceous ooze, and non-carbonaceous fine-grained sediments. We use cores from the pelagic ocean instead of cores close to the shore to avoid influences of coastal erosion and fluvial input (organic matter, terrigenous input). The age of the majority of the sediments ranges from the mid-Pleistocene to the Holocene (Benz et al., 2016; Chao et al., In prep.; Lamy et al., 2014; Max et al., 2012a; Nürnberg, 2018a; Ullermann et al., 2016; Wang et al., 2021a).

To determine bulk sediment parameters immediately after opening of the sediment cores on board, we took syringe samples of 10 cm<sup>3</sup> in 10 cm intervals from the working halves of the core and transferred them into pre-weighed glass vials. All samples were stored at 4° C until further shore-based processing. The samples in this study were weighed before and after freeze-drying, homogenized and measured for TC and TOC by a CNS-analyzer (Elementar vario EL III) and a carbon/sulfur analyzer (Eltra CS-800) in the laboratories at AWI in Bremerhaven. The CaCO<sub>3</sub> content was then calculated from the difference between TC and TOC as follows:

$$CaCO_3 \text{ wt\%} = (TC - TOC) \times 8.333 \times 100\%$$

### **6.7.2. Setting of the Avaatech XRF scanning and data compilation**

All XRF-scanning measurements were carried out with an Avaatech XRF core scanner at the AWI in Bremerhaven. The X-ray excitation scanning settings were 10 kV at 150 mA with no filter for a count time of 10 s. A rhodium target X-ray tube was deployed. This setting is optimized for producing signals related to CaCO<sub>3</sub> because it is used as the main estimation for discussing oceanic carbon system. Sample distance was 10 mm, with a 10 mm x 12 mm slit size. In order to include comprehensive information and avoid the software bias, which could be caused by manual operation, the raw spectrum (2048 channels) for each scanning point was chosen instead of processed elemental intensities. The XRF spectra were normalized by the sum of channel signals for each data point to prevent bias from X-ray tube aging. Next, the normalized spectra were standardized to zero mean and unit variance, which balances the importance of each channel number. This is an important pre-treatment prior to PCA and NMF.

The bulk geochemistry (CaCO<sub>3</sub>, TOC) was collected and transformed with a natural logarithm to avoid predicting negative contents later in the model. The XRF spectra were aligned to the bulk chemistry measurements by depth.

### **6.7.3. Use of machine learning programming**

The developing codes were written in Python scripts and Jupyter notebooks by implementing Python3 built-in functions and SciPy ecosystem packages (Numpy, pandas and scikit-learn) (Harris et al., 2020; McKinney, 2010; Millman and Aivazis, 2011; Pedregosa et al., 2011; Thomas et al., 2016; Virtanen et al., 2020). The visualizations were conducted using Matplotlib and Seaborn packages (Hunter, 2007; Waskom, 2021). We rely on a high-performance computing system managed by Slurm (Klimageographie, University of Bremen) to facilitate the heavy computation for model building. The developing steps were carefully recorded via Git. To promote the FAIR principle (Wilkinson et al., 2016), models, codes and package dependencies are all open access on Github ([https://github.com/dispink/CaCO3\\_NWP](https://github.com/dispink/CaCO3_NWP)).

## **6.8. Data availability**

The datasets generated during and/or analyzed during the current study are available in the Pangaea in accordance with and under the license of CC-BY: Creative Commons Attribution 4.0 International. Chao, Weng-si; Lee, An-Sheng; Tiedemann, Ralf; Lembke-Jene, Lester; Lamy, Frank (2022): XRF down-core scanning and bulk chemistry measurements of sediments from the high latitude sectors of Pacific Ocean. PANGAEA, <https://doi.org/10.1594/PANGAEA.949225>. The analyzing results is included in the supplement.

## **6.9. References**

- Abu-Mostafa, Y.S., Magdon-Ismail, M. and Lin, H.-T., 2012. Learning From Data: A Short Course. AMLBook.
- Alpaydin, E., 2014. Introduction to Machine Learning (Adaptive Computation and Machine Learning series). The MIT Press, 640 pp.
- Archer, D. and Maier-Reimer, E., 1994. Effect of deep-sea sedimentary calcite preservation on atmospheric CO<sub>2</sub> concentration. *Nature*, 367(6460): 260-263.
- Bellon-Maurel, V., Fernandez-Ahumada, E., Palagos, B., Roger, J.-M. and McBratney, A., 2010. Critical review of chemometric indicators commonly used for assessing the quality of the prediction of soil attributes by NIR spectroscopy. *TrAC Trends in Analytical Chemistry*, 29(9): 1073-1081.

- Benz, V., Oliver, E., Rainer, G., Frank, L. and Ralf, T., 2016. Last Glacial Maximum sea surface temperature and sea-ice extent in the Pacific sector of the Southern Ocean. *Quaternary Science Reviews*, 146: 216--237.
- Bolton, M.S.M., Jensen, B.J.L., Wallace, K., Praet, N., Fortin, D., Kaufman, D. and De Batist, M., 2020. Machine learning classifiers for attributing tephra to source volcanoes: an evaluation of methods for Alaska tephtras. *Journal of Quaternary Science*, 35: 81-92.
- Böning, P., Bard, E. and Rose, J., 2007. Toward direct, micron-scale XRF elemental maps and quantitative profiles of wet marine sediments. *Geochemistry, Geophysics, Geosystems*, 8(5).
- Breiman, L., 2001. Random forests, *Machine Learning*. Springer, pp. 5-32.
- Caley, T., Malaizé, B., Zaragosi, S., Rossignol, L., Bourget, J., Eynaud, F., Martinez, P., Giraudeau, J., Charlier, K. and Ellouz-Zimmermann, N., 2011. New Arabian Sea records help decipher orbital timing of Indo-Asian monsoon. *Earth and Planetary Science Letters*, 308(3-4): 433-444.
- Chang, C.-C. and Lin, C.-J., 2011. LIBSVM: A Library for Support Vector Machines. *ACM Transactions on Intelligent Systems and Technology*, 2(3): 1-27.
- Chao, W.-S., Jacobi, L., Niederbockstruck, B., Nürnberg, D., Langemann, L., Kuhn, G., Bubenchshikova, N., Zou, J.-J., Shi, X.-F., Tiedemann, R. and Lembke-Jene, L., In prep. Glacial-interglacial variations in productivity and carbonate deposition in the Northwest Pacific during the last 500,000 years. *Frontiers in Earth Science*.
- Cichocki, A. and Phan, A.-H., 2009. Fast local algorithms for large scale nonnegative matrix and tensor factorizations. *IEICE transactions on fundamentals of electronics, communications and computer sciences*, 92(3): 708-721.
- Clifford, G., 2008. Chapter 15-BLIND SOURCE SEPARATION: Principal & Independent Component Analysis, *Biomedical Signal and Image Processing*. MIT Electrical Engineering and Computer Science.
- Croudace, I.W., Löwemark, L., Tjallingii, R. and Zolitschka, B., 2019. Current perspectives on the capabilities of high resolution XRF core scanners. *Quaternary International*, 514: 5-15.
- Croudace, I.W., Rindby, A. and Rothwell, R.G., 2006. ITRAX: description and evaluation of a new multi-function X-ray core scanner. *Geological Society, London, Special Publications*, 267(1): 51-63.
- Févotte, C. and Idier, J., 2011. Algorithms for nonnegative matrix factorization with the  $\beta$ -divergence. *Neural computation*, 23(9): 2421-2456.
- Geurts, P., Ernst, D. and Wehenkel, L., 2006. Extremely randomized trees. *Machine learning*, 63(1): 3-42.
- Harris, C.R., Millman, K.J., van der Walt, S.J., Gommers, R., Virtanen, P., Cournapeau, D., Wieser, E., Taylor, J., Berg, S., Smith, N.J., Kern, R., Picus, M., Hoyer, S., van Kerkwijk, M.H., Brett, M., Haldane, A., del Río, J.F., Wiebe, M., Peterson, P., Gérard-Marchant, P., Sheppard, K., Reddy, T., Weckesser, W., Abbasi, H., Gohlke, C. and Oliphant, T.E., 2020. Array programming with NumPy. *Nature*, 585: 357-362.
- Hunter, J.D., 2007. Matplotlib: A 2D graphics environment. *Computing in Science and Engineering*, 9: 99-104.
- Jansen, J., Van der Gaast, S., Koster, B. and Vaars, A., 1998. CORTEX, a shipboard XRF-scanner for element analyses in split sediment cores. *Marine geology*, 151(1-4): 143-153.
- Jordan, M.I. and Mitchell, T.M., 2015. Machine learning: Trends, perspectives, and prospects. *Science*, 349: 255-260.

- Kaboth-Bahr, S., Denis, V., Su, C.-C., O'Regan, M., Gyllencreutz, R., Jakobsson, M. and Löwemark, L., 2018. Deciphering ~45.000 years of Arctic Ocean lithostratigraphic variability through multivariate statistical analysis. *Quaternary International*.
- Lamy, F., Gersonde, R., Winckler, G., Esper, O., Jaeschke, A., Kuhn, G., Ullermann, J., Martinez-Garcia, A., Lambert, F. and Kilian, R., 2014. Increased Dust Deposition in the Pacific Southern Ocean During Glacial Periods. *Science*, 343(6169): 403-407.
- Max, L., Riethdorf, J.-R., Tiedemann, R., Smirnova, M., Lembke-Jene, L., Fahl, K., Nürnberg, D., Matul, A. and Mollenhauer, G., 2012. Sea surface temperature variability and sea-ice extent in the subarctic northwest Pacific during the past 15,000 years. *Paleoceanography*, 27(3).
- McHugh, C.M., Gurung, D., Giosan, L., Ryan, W.B., Mart, Y., Sancar, U., Burckle, L. and Cagatay, M.N., 2008. The last reconnection of the Marmara Sea (Turkey) to the World Ocean: A paleoceanographic and paleoclimatic perspective. *Marine Geology*, 255(1-2): 64-82.
- McKinney, W., 2010. Data Structures for Statistical Computing in Python, The 9th Python in Science Conference, pp. 56-61.
- Millman, K.J. and Aivazis, M., 2011. Python for scientists and engineers. *Computing in Science and Engineering*, 13: 9-12.
- Müller, A.C. and Guido, S., 2016. *Introduction to Machine Learning with Python: A Guide for Data Scientists*. O'Reilly Media.
- Nürnberg, D., 2018. RV SONNE Fahrtbericht / Cruise Report SO264 - SONNE-EMPEROR: The Plio/Pleistocene to Holocene development of the pelagic North Pacific from surface to depth – assessing its role for the global carbon budget and Earth's climate, Suva (Fiji) – Yokohama (Japan), 30.6. – 24.8.2018, GEOMAR Helmholtz-Zentrum für Ozeanforschung, Kiel, Germany.
- Ön, Z.B. and Özeren, M.S., 2019. Temperature and precipitation variability in eastern Anatolia: Results from independent component analysis of Lake Van sediment data spanning the last 250 kyr BP. *Quaternary International*, 514: 119-129.
- Pedregosa, F., Varoquaux, G., Gramfort, A., Michel, V., Thirion, B., Grisel, O., Blondel, M., Prettenhofer, P., Weiss, R., Dubourg, V., Vanderplas, J., Passos, A., Cournapeau, D., Brucher, M., Perrot, M. and Duchesnay, É., 2011. Scikit-learn: Machine Learning in Python. *Journal of Machine Learning Research*, 12: 2825-2830.
- Schulz, H. and Zabel, M., 2006. *Marine Geochemistry*. Springer, Berlin, Heidelberg.
- Thomas, K., Benjamin, R.-K., Fernando, P., Brian, G., Matthias, B., Jonathan, F., Kyle, K., Jessica, H., Jason, G., Sylvain, C., Paul, I., Damin, A., Safia, A. and Carol, W., 2016. Jupyter Notebooks -- a publishing format for reproducible computational workflows. In: F. Loizides and B. Schmidt (Editors), *Positioning and Power in Academic Publishing: Players, Agents and Agendas*, pp. 87 - 90.
- Tjallingii, R., Röhl, U., Kölling, M. and Bickert, T., 2007. Influence of the water content on X-ray fluorescence core-scanning measurements in soft marine sediments. *Geochemistry, Geophysics, Geosystems*, 8(2).
- Ullermann, J., Lamy, F., Ninnemann, U., Lembke-Jene, L., Gersonde, R. and Tiedemann, R., 2016. Pacific-Atlantic Circumpolar Deep Water coupling during the last 500 ka. *Paleoceanography*, 31(6): 639-650.
- Virtanen, P., Gommers, R., Oliphant, T.E., Haberland, M., Reddy, T., Cournapeau, D., Burovski, E., Peterson, P., Weckesser, W., Bright, J., Van Der Walt, S.J., Brett, M., Wilson, J., Millman, K.J., Mayorov, N., Nelson, A.R.J., Jones, E., Kern, R., Larson, E., Carey, C., Polat, İ., Feng, Y., Moore, E.W., VanderPlas, J., Laxalde, D., Perktold, J., Cimrman, R., Henriksen, I., Quintero, E.A., Harris, C.R., Archibald, A.M., Ribeiro, A.H., Pedregosa, F., van Mulbregt, P. and Contributors, S., 2020. *SciPy 1.0--*

- Fundamental Algorithms for Scientific Computing in Python. *Nature Methods*, 17: 261-272.
- Wang, W., Dobeneck, T.v., Frederichs, T., Zhang, Y., Lembke-Jene, L., Tiedemann, R., Winklhofer, M. and Nürnberg, D., 2021. Dating North Pacific Abyssal Sediments by Geomagnetic Paleointensity: Implications of Magnetization Carriers, Plio-Pleistocene Climate Change, and Benthic Redox Conditions. *Frontiers in Earth Science*: 577.
- Waskom, M.L., 2021. seaborn: statistical data visualization, *J. Open Source Softw.*, 6, 3021. *Journal of Open Source Software*, 6(60): 3021.
- Weltje, G.J., Bloemsa, M.R., Tjallingii, R., Heslop, D., Röhl, U. and Croudace, I.W., 2015. Prediction of Geochemical Composition from XRF Core Scanner Data: A New Multivariate Approach Including Automatic Selection of Calibration Samples and Quantification of Uncertainties. In: I.W. Croudace and R.G. Rothwell (Editors), *Micro-XRF Studies of Sediment Cores: Applications of a non-destructive tool for the environmental sciences*. Springer Netherlands, Dordrecht, pp. 507-534.
- Weltje, G.J. and Tjallingii, R., 2008. Calibration of XRF core scanners for quantitative geochemical logging of sediment cores: Theory and application. *Earth and Planetary Science Letters*, 274(3-4): 423-438.
- Wilkinson, M.D., Dumontier, M., Aalbersberg, I.J., Appleton, G., Axton, M., Baak, A., Blomberg, N., Boiten, J.-W., da Silva Santos, L.B., Bourne, P.E., Bouwman, J., Brookes, A.J., Clark, T., Crosas, M., Dillo, I., Dumon, O., Edmunds, S., Evelo, C.T., Finkers, R., Gonzalez-Beltran, A., Gray, A.J.G., Groth, P., Goble, C., Grethe, J.S., Heringa, J., 't Hoen, P.A.C., Hooft, R., Kuhn, T., Kok, R., Kok, J., Lusher, S.J., Martone, M.E., Mons, A., Packer, A.L., Persson, B., Rocca-Serra, P., Roos, M., van Schaik, R., Sansone, S.-A., Schultes, E., Sengstag, T., Slater, T., Strawn, G., Swertz, M.A., Thompson, M., van der Lei, J., van Mulligen, E., Velterop, J., Waagmeester, A., Wittenburg, P., Wolstencroft, K., Zhao, J. and Mons, B., 2016. The FAIR Guiding Principles for scientific data management and stewardship. *Scientific Data*, 3(1): 160018.
- Ziegler, M., Jilbert, T., de Lange, G.J., Lourens, L.J. and Reichert, G.J., 2008. Bromine counts from XRF scanning as an estimate of the marine organic carbon content of sediment cores. *Geochemistry, Geophysics, Geosystems*, 9(5).

## 6.10. Acknowledgments

We thank the crew and the science parties of different cruises for their contributions to core and sample acquisition on the respective expeditions. We are very grateful to Dr. Frank Lamy for providing data from the Southern Ocean. We also sincerely thank Valéa Schumacher, Susanne Wiebe, and Rita Fröhlking and student assistants at the AWI Marine Geology Laboratory in Bremerhaven for technical assistance with XRF-scanning, CaCO<sub>3</sub> and TOC measurements. We also acknowledge Ben Marzeion and Timo Rothenpieler (Klimageographie, University of Bremen) for generously providing access and support to their high-performance computing power.

We acknowledge financial support from the Wadden Sea Archive (WASA) project funded by the ‘Niedersächsisches Vorab’ of the VolkswagenStiftung within the funding initiative ‘Küsten und Meeresforschung in Niedersachsen’ of the Ministry of Science and Culture of Lower Saxony, Germany (project VW ZN3197), the Ministry of Science and Technology of Taiwan (project number: MOST 110-2116-M-002-023), the AWI institutional budget under “PACES-II” (2018-20), the German Federal Ministry for Education and Research (BMBF) grants no. 03G0264B “SO264-EMPEROR” and 03F0785B “NOPAWAC”, and the 2022 Ørsted’s Green Energy Scholarship Program.

## **6.11. Author contributions**

ASL and WSC: Conceptualization, Methodology, Investigation, Data curation, Writing – original draft.

RT, LLJ, BZ, and SYHL.: Supervision, Writing – review and editing, Resources, Funding acquisition.

## **6.12. Supplementary**

### **6.12.1. Detailed grid search results**

During a pilot test, the number of principal components was chosen as 5, i.e. before the explained variance flattened (Figure S 1, Left). This number was also adopted later for the initial grid search of the Non-negative Matrix Factorization (NMF). Figure S 1 (Right) indicates that the combination of NMF and kernel Support Vector Machine (SVM) gives the best performance ( $R^2 = 0.91$ ). The Ridge Linear Regression (LR) shows the slightly worse performance, while the Random Forest (RF) has the worst performance.

There are three parameters that need to be fine-tuned in building models:  $n\_components$  for NMF,  $C$  and  $\gamma$  for SVM. Based on the Principal Component Analysis (PCA) results of the pilot test (Figure S 1), we initially tried  $n\_components$  from 5. For each setting of components, ranges of  $C$  and  $\gamma$  have been searched in logarithmic scales to find the model with best performance. When the optimal combination of parameters locates away from the edge of the plot (Figures S 2 and S 3, i.e., ranges of parameters), it is chosen to build the optimal model. The optimal component amount for the TOC model was set to 13, at the edge of the

searching range. The reason why upward searching was not continued is that the model's fitting time extends noticeably when increased.

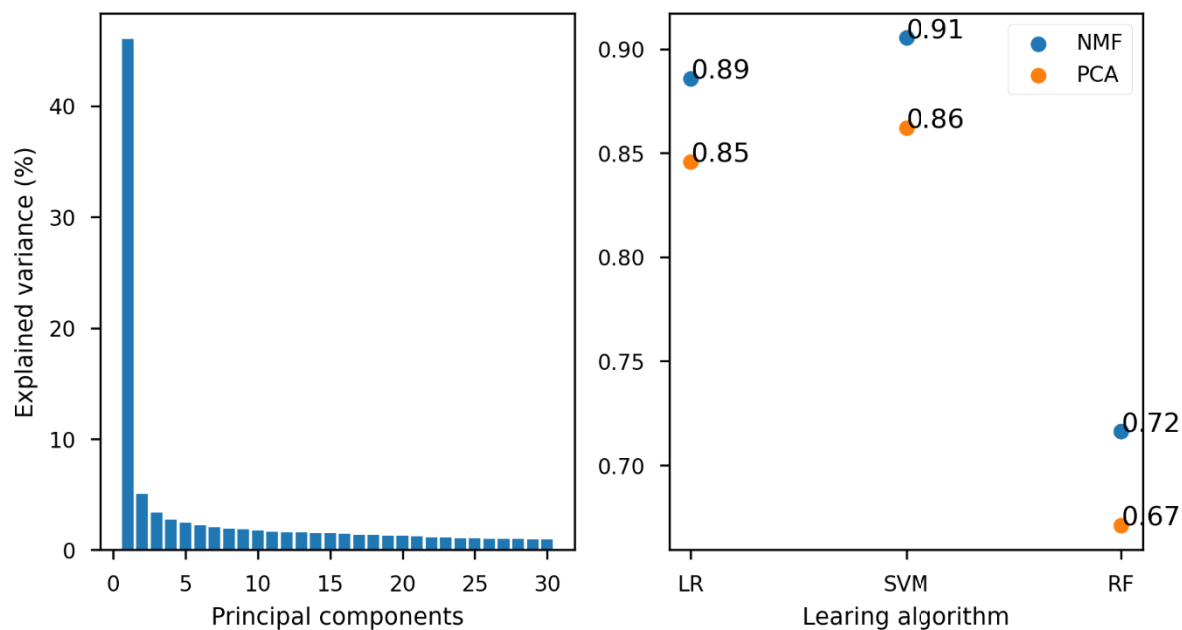


Figure S 1. Results of the pilot test. Left: Explained variance of each principal component. Right: Best performance ( $R^2$ ) of each workflow.

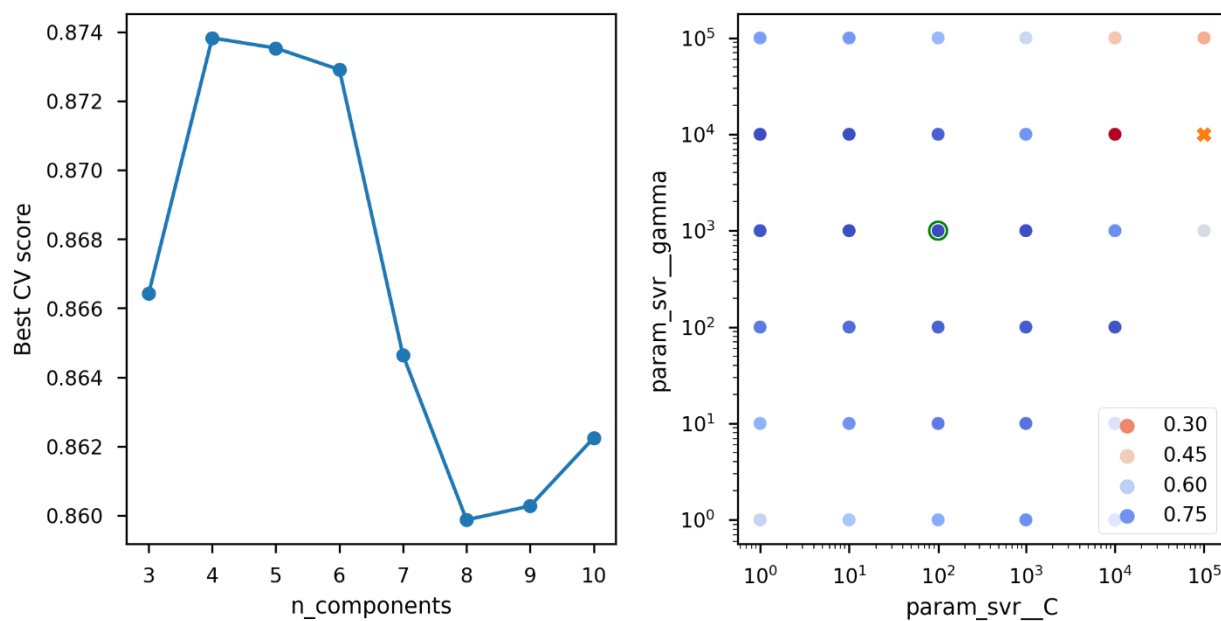


Figure S 2. Visualization of grid search results for  $\text{CaCO}_3$ . Left: Best CV score for each setting of  $n\_components$  for NMF. Right: CV score grid of the pair of SVM parameters under  $n\_components = 4$ . The optimal pair of SVM parameters is marked by a green circle.



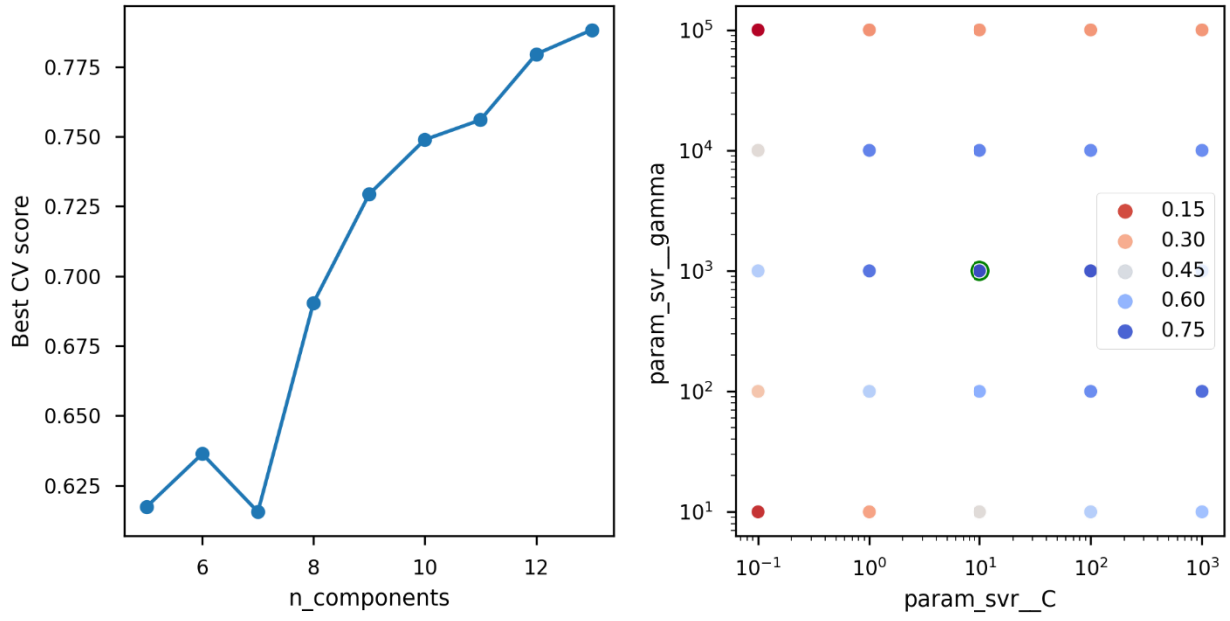


Figure S 3. Visualization of grid search results for TOC. Left: Best CV score in each setting of  $n\_components$  for NMF. Right: CV score grid of the pair of SVM parameters under  $n\_components = 13$ . The optimal pair of SVM parameters is marked by a green circle.

Table S 1. Parameter settings for the optimal model for calcium carbonate ( $\text{CaCO}_3$ ) and total organic carbon (TOC).  $n\_components$  is for NMF.  $C$  and  $\gamma$  are for SVM.

Analyte	$n\_components$	$C$	$\gamma$
$\text{CaCO}_3$	4	100	1000
TOC	13	10	1000

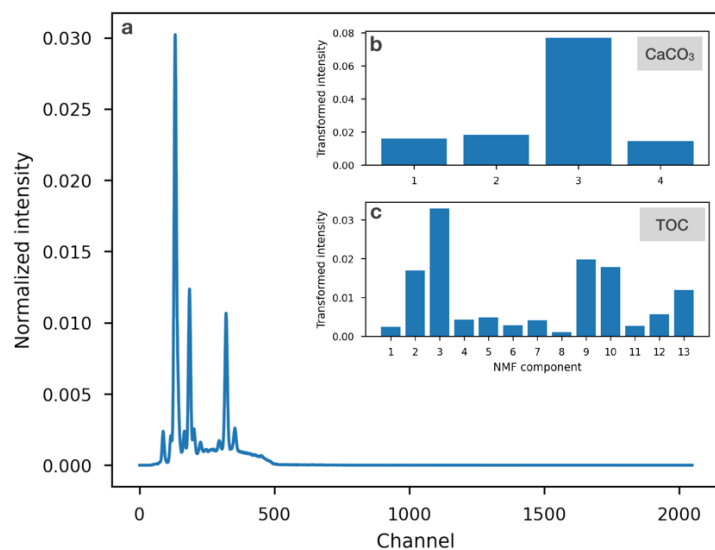


Figure S 4. (a) Example for a normalized spectrum of the data point at 105 mm depth of the case study core (SO264-69-2). Transformed spectra by NMF chained in the optimal models of (b)  $\text{CaCO}_3$  and (c) TOC from the spectrum (a).

Dataset S1. Grid search results of the pilot research.

pilot\_grid\_ridge\_20210823.csv

pilot\_grid\_svr\_20210318.csv

pilot\_grid\_rf\_20210822.csv

(<https://drive.google.com/file/d/1TWIsOJ8UGHBZvvUZ-hiKQpwHGw3Oc4Es/view?usp=sharing>)

Dataset S2. Grid search result of building models for  $\text{CaCO}_3$  and TOC.

grid\_caco3+toc\_compile\_20210823.csv

(<https://drive.google.com/file/d/1TWIsOJ8UGHBZvvUZ-hiKQpwHGw3Oc4Es/view?usp=sharing>)

### 6.12.2. Evaluation in case study

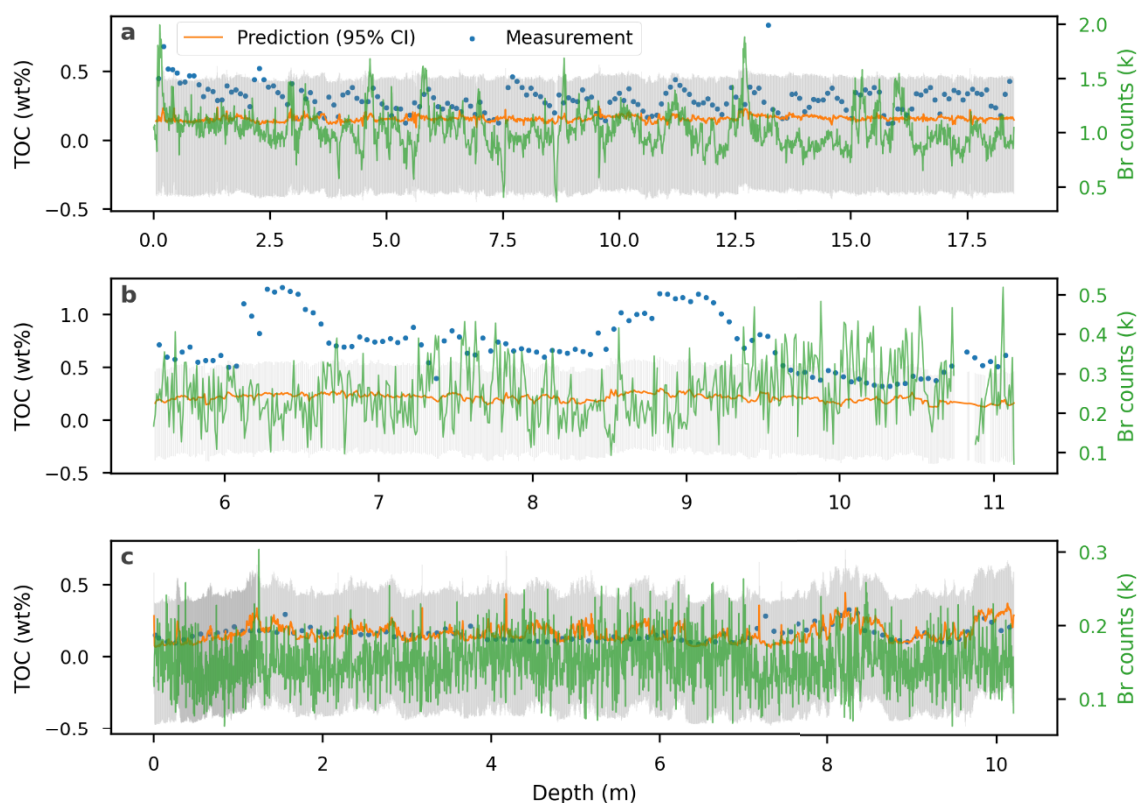


Figure S 5. Measured (blue dots) and predicted (orange lines with 95 % confident intervals as gray bars) TOC contents estimated with the commonly applied XRF proxy Br (counts in green from 30 kV-runs) in the case study cores (a: SO264-69-2, b: LV28-44-3, c: PS75/056-1).

### 6.12.3. Info and exported data

Dataset S3. High-resolution (10 mm) quantified  $\text{CaCO}_3$  and TOC.

predict\_202200629.csv on Pangaea (waiting for Pangaea for data curation)

XRF setting: Avaatech XRF core scanner with the X-ray excitation scanning settings, 10 kV at 150 mA with no filter for a count time of 10 s, and a rhodium target X-ray tube was deployed.

Table S 2. Station list of the studied cores for the whole dataset with relevant information including amount of measurements, dating methods, core age and references.

Station	Latitude (°N)	Longitude (°E)	Water depth (m)	Core length (m)	TOC % data amount	TC % data amount	Bulk measurement reference	Core bottom ca. age (ka)	Chrono-stratigraphic methods	Age data reference	Notes
LV29-114-3	49.375667	152.877933	1762	9.5	72	72	<i>Max et al. 2012</i>	26.87 (@5.02m)	<sup>14</sup> C, XRF*	<i>Max et al., 2012</i>	Upper 5 m was studied
SO178-12-3	51.605367	145.4357	1211	16.99	63	n.d.	unpublished data			unpublished data	Upper 6.62 m was studied
SO264-13-2	37.79775	170.72211	3935	13.81	39	39	unpublished data		XRF	unpublished data	
SO264-15-2	41.85472	170.51111	3662	14.48	40	40	<i>Chao</i>	947	XRF, stableisotope	<i>Chao</i>	
SO264-28-2	45.00166	170.32305	1935	7.64	39	39	unpublished data	1400	<sup>14</sup> C, XRF, stable isotope	unpublished data	
SO264-55-1	47.32027	169.4975	2936	16.11	159	159	<i>Chao</i>	450	<sup>14</sup> C, XRF, stable isotope, tephra	<i>Nürnberg, 2018</i>	
SO264-56-2	47.94222	169.77722	3973	12.66	35	35	unpublished data	1152	XRF, tephra, paleomag.	<i>Wang et al., 2021; Nürnberg, 2018</i>	
SO264-64-1	50.12055	168.34666	3495	18.55	36	36	unpublished data	678	XRF	unpublished data	
SO264-66-2	50.26861	168.51138	2751	15.04	40	40	<i>Chao</i>	734	XRF	<i>Chao</i>	
PS97/27-2	-54.384833	-74.605833	2341.8	2.01	20	20	unpublished data			unpublished data	
PS97/46-4	-60.997167	-65.356167	2775.3	2.26	21	21	unpublished data			unpublished data	XRF only until 126cm
PS97/52-4	-62.499	-64.293667	2890.4	3.14	30	30	unpublished data			unpublished data	
PS97/53-2	-62.662833	-63.0935	2016.1	2	17	17	unpublished data			unpublished data	
PS97/78-1	-60.6525	-55.839667	3666.4	2.23	21	21	unpublished data			unpublished data	

PS97/79-2	-60.142333	-58.991333	3541.3	8.28	83	83	unpublished data			unpublished data	1st core section no XRF
PS97/80-1	-59.674667	-59.631333	3105.9	1.24	11	11	unpublished data			unpublished data	
PS97/83-2	-58.994333	-60.570333	3762.3	6.08	60	60	unpublished data			unpublished data	
PS97/84-1	-58.869	-60.865667	3557	10.94	109	109	unpublished data			unpublished data	1st core section no XRF
PS97/84-1 TC				9	8	8	unpublished data			unpublished data	TC = trigger core
PS97/85-3	-58.3545	-62.167167	3090.8	14.43	145	145	unpublished data			unpublished data	
PS97/85-3 TC				8.9	8	8	unpublished data			unpublished data	TC = trigger core
PS97/89-1	-58.226667	-62.7265	3437.2	10.02	100	100	unpublished data			unpublished data	
PS97/89-1 TC				9	8	8	unpublished data			unpublished data	TC = trigger core
PS97/92-1	-57.763	-69.878833	3823.7	7.89	78	78	unpublished data			unpublished data	
PS97/93-2	-57.499167	-70.274667	3782.2	16.45	162	162	unpublished data			unpublished data	
PS97/128-2	-53.634330	-75.54583	2313.4	10.69	104	104	unpublished data			unpublished data	XRF only until 167cm
PS75/054-1	-56.15175	-115.133033	4113	22.38	224	224	unpublished data	160	XRF	<i>Benz et al., 2016</i>	
PS75/083-1	-60.268833	-159.059833	3599	13.13	131	131	unpublished data	268	Fe - dust	<i>Lamy et al., 2014</i>	
PS75/083-1 TC				0.37	4	4	unpublished data				TC = trigger core
PS75/093-1	-60.872167	-169.548167	3762	12.84	129	129	unpublished data	528	<sup>14</sup> C, XRF	<i>Benz et al., 2016</i>	
PS75/093-1 TC				0.92	9	9	unpublished data				TC = trigger core
PS75/095-5	-57.019667	-174.43	4853	17.85	177	177	unpublished data				

Case study core										
PS75/056-1	-55.162333	-114.7885	3581	10.21	103	103	unpublished data	256	stable isotope	<i>Ullermann et al., 2016</i>
SO264-69-2	50.514480	167.92488	3473	18.55	184	184	unpublished data	450	XRF	<i>Chao</i>
LV28-44-3	52.0419	153.09915	684	11.13	111	111	unpublished data			Upper 5.59 m was studied

\* pattern correlation of XRF ratios/elements that is associated between core(s) and published record(s) is used as a chronostratigraphic approach here. See Chao (in prep.) and Max, L et al. (2012).

n.d. = not determined

### Reference

Benz, V et al. (2016): Last Glacial Maximum sea surface temperature and sea-ice extent in the Pacific sector of the Southern Ocean. *Quaternary Science Reviews*, 146, 216-237

Chao, W.-S. et al. Glacial-interglacial variations in productivity and carbonate deposition in the Northwest Pacific during the last 500,000 years. *Frontiers in Earth Science* (In prep.)

Lamy, F et al. (2014): Increased dust deposition in the Pacific Southern Ocean during glacial periods. *Science*, 343(6169), 403-407

Max, L et al. (2012): Sea surface temperature variability and sea-ice extent in the subarctic northwest Pacific during the past 15,000 years. *Paleoceanography*, 27(3), PA3213

Nürnberg, D ed. (2018) RV SONNE Fahrtbericht / Cruise Report SO264 - SONNE-EMPEROR: The Plio/Pleistocene to Holocene development of the pelagic North Pacific from surface to depth – assessing its role for the global carbon budget and Earth's climate, Suva (Fiji) – Yokohama (Japan), 30.6. – 24.8.2018.

Ullermann, J et al. (2016): Pacific-Atlantic Circumpolar Deep Water coupling during the last 500 ka. *Paleoceanography*, 31(6), 639-65

Wang, W et al. (2021). Dating North Pacific Abyssal Sediments by Geomagnetic Paleointensity: Implications of Magnetization Carriers, Plio-Pleistocene Climate Change, and Benthic Redox Conditions. *Frontiers in Earth Science*, 577.

## 7. Synthesis and Outlook

### 7.1. Synthesis

This thesis has provided new information on paleoceanographic changes in the NW Pacific during the last 550,000 years, in order to achieve a better understanding on the role of the deep North Pacific in the global oceanic overturning circulation and the marine carbon cycle. A variety of different geochemical proxies and methods were used to investigate the variations and relationship between biological export production and carbonate deposition, as well as the deep water ventilation and circulation history in the NW Pacific. In this thesis, I also presented a new approach of using machine learning (ML) to quantify bulk chemistry data from X-ray fluorescence (XRF) spectra.

The cruise SO264 succeeded in obtaining sediment cores along the Emperor Seamount Chain to address the topics above. All cores were XRF-scanned to obtain semi-quantitative, but high-resolution downcore elemental profiles (Appendix 1). In the first part of the thesis, I presented the regional age model approach for the sediment cores elaborated on in chapter 3. The XRF-based age model was corroborated by benthic oxygen isotope stratigraphy and radiocarbon dating, showing the potential to establish coherent age models leading to a regional stratigraphic framework in the NW Pacific. A significant correlation emerged between XRF-Ba/Ti ratios used as proxy for paleo-productivity, Ca/Ti ratios indicative of carbonate production, and the large-scale climate development reflected in global reference records, e.g., the EPICA Dome C atmospheric CO<sub>2</sub> record and or the global benthic  $\delta^{18}\text{O}$  stack, with maxima in the used proxy records matching interglacial periods.

Based on this age model approach, a reconstruction of NW Pacific export production changes and its relation to carbonate deposition and dissolution on suborbital to orbital timescales was carried out for the last 500 kyr BP (chapter 4). I highlighted the importance of this region and outlined its differences to other basins of the world ocean in CaCO<sub>3</sub> content and flux preservation, prominently expressed in a regionally reversing carbonate deposition pattern along the meridional transect of the studied sites. Several factors were likely responsible for shaping the reconstructed proxy variations in close alignment with glacial-interglacial climate changes. In particular changes in the macronutrient supply to the upper oceanic from deeper water masses, linked to changes in both surface and deep-intermediate ocean stratification, and the closely connected dynamic contraction and expansion of the NW Pacific subarctic and

subtropical gyre likely caused or promoted the carbonate-corrosiveness of bathyal water masses and their relation to carbonate chemistry in the subarctic Pacific. While the underlying mechanisms and forcing factors remain uncertain, it became evident that the subarctic Pacific carbonate cycle is more complicated than previously assumed.

In a subsequent step, the ventilation history of the deep North Pacific was investigated for the last 540 ka (chapter 5). A new monospecific epibenthic foraminiferal (*C. wuellerstorfi*) record from the deep NW Pacific provides new information on the ventilation history of NPDW and allows to relate changes in its stable carbon and oxygen isotope characteristics to its source water masses. My observations provide complementary evidence for the assumption that the glacial bathyal NW Pacific repeatedly became more isolated from more expanded, better ventilated mid-depth water masses sourced from the northern marginal seas. During these boundary conditions, glacial North Pacific Deep Water was potentially more closely connected to abyssal water masses sourced from the polar Pacific sector of the Southern Ocean and likely contained an expanded carbon reservoir in a more stagnant overturning setting. This bathyal to abyssal deep ocean became a major source of rising atmospheric CO<sub>2</sub> via deep water carbon efflux during glacial terminations and subsequent interglacials. Transient collapses of the halocline and increased ocean ventilation during terminations accompanied the release of <sup>13</sup>C-depleted carbon to the atmosphere from the deep NW Pacific.

However, the carbonate-carbon cycle and the budget of carbon storage in the NW Pacific remain ambiguous. A better resolved reconstruction of the expansion and contraction of regional carbonate preservation through time is indispensable to quantify and assess the subarctic Pacific carbon marine reservoir domain. Such a task remains laborious, ultimately restricting the temporal and spatial resolution to obtain large amounts of quantitative CaCO<sub>3</sub> content data at present. One new approach to improve the generation of temporally and spatially highly-resolved time series process is introduced in the final part of this thesis (chapter 6), using machine learning to quantify and predict geochemical data in sediments from raw XRF spectra. Based on this study, most sediment records from the mid- to high-latitude Pacific with associated XRF-scanning data could be used to provide quantitative CaCO<sub>3</sub> content data. Further guidelines for future users are provided, who want to adopt this approach or develop an own model based on their records. This study hopefully will inspire the palaeoceanographic community to carry out future studies and enable calculation of high-resolution quantitative bulk chemistry data without losing accuracy compared to established methods.



## **1.1. Outlook**

### **7.1.1. High Resolution Reconstruction of Calcium Carbonate Preservation in Northwest Pacific**

In order to gain a better understanding of the CO<sub>2</sub> buffer capacity and the potential of the North Pacific Ocean influencing the atmospheric CO<sub>2</sub>, a reconstruction of the marine CaCO<sub>3</sub> preservation through time is essential. Due to the steep gradient and shallow lysocline in North Pacific and the lack of available records in this vast ocean basin, multi-site reconstructions of Pacific carbonate system variations are demanding. Only few studies presented carbonate preservation patterns by using cores from the East Equatorial Pacific and NE Pacific, with relatively low resolution in the discrete carbonate data (Farrell and Prell, 1989; Zahn et al., 1991). However, a more complete picture of the spatial and temporal variations in the carbonate cycle of the entire Pacific is still needed. Based on the results from chapter 4, one could assume a highly diverse carbonate distribution pattern through time between the NW and NE Pacific, comprising the subarctic and subtropical regions. Given that carbonate preservation is regulated via the interplay between ocean chemistry (dissolution) and productivity (deposition), the differentiation of the characteristics in the North Pacific water masses could modify all these factors. Variations in carbonate depositional history based on a complete coverage of the study region, from shallow to abyssal water depths, and from subpolar to subtropical regions by using a comprehensive collection of marine sediment cores would provide new insights into the spatially resolved role of the NW Pacific in the marine carbon cycle through time, encompassing different climate stages. The XRF-ML approach presented in this thesis improves on the analytical processing time needed and hence the acquisition of sufficiently resolved results to allow for a quantitative reconstruction and synthesis of regional to basin-wide carbonate chemistry signatures, and its relation to the global climate.

A preliminary result of NW Pacific carbonate distribution over the last 800 ka by using the XRF-ML approach is presented here (Figure 7.2.1). The CCD was relatively shallow and its variations through time were significant and larger than envisioned in previous studies based on more limited data from the Eastern Equatorial Pacific (Farrell and Prell, 1989). However, further investigations and amendments to the present data status are needed to gain a complete understanding on rapid CCD changes in the Pacific and its underlying forcing factors.

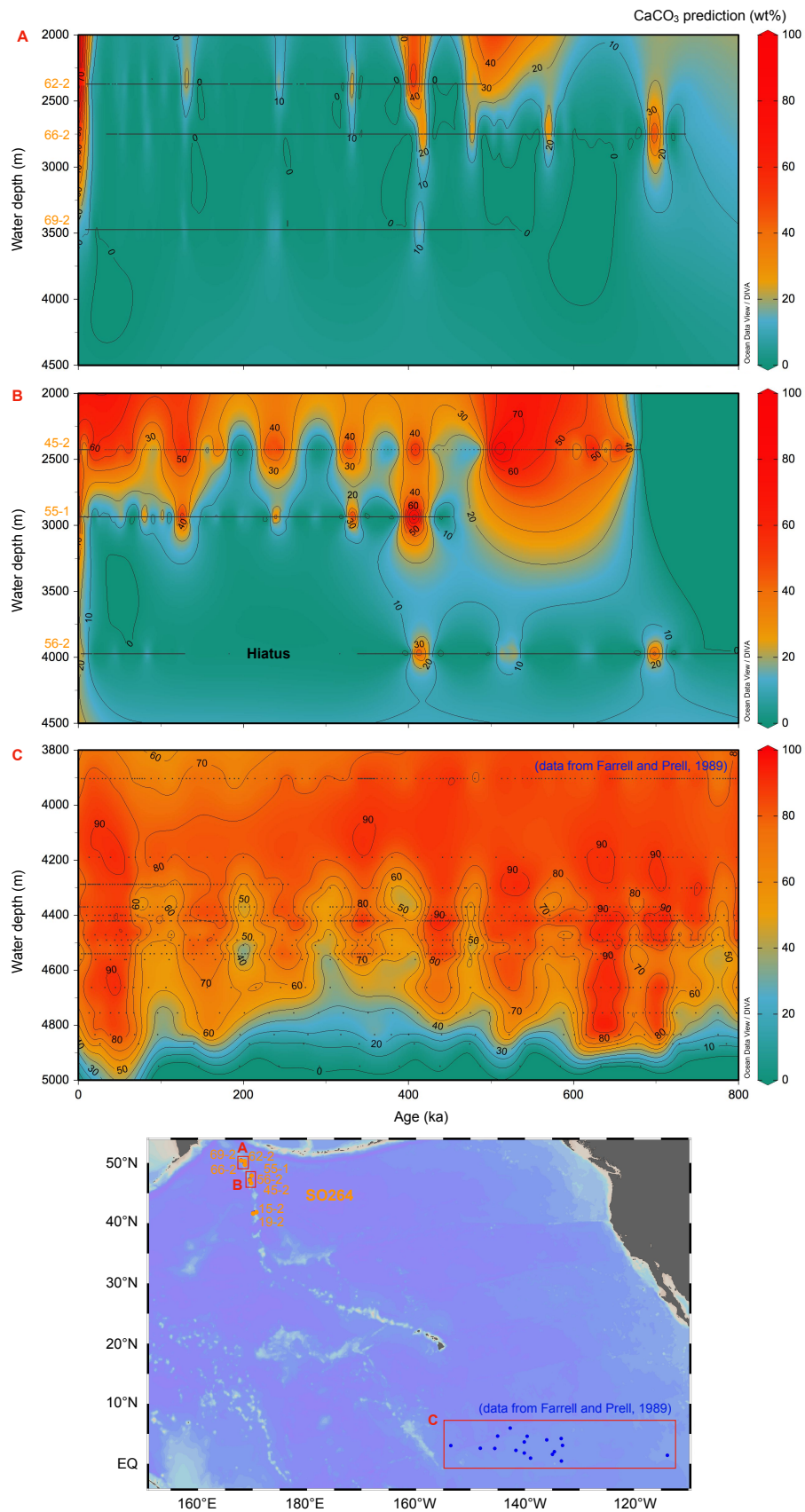


Figure 7.2.1. Cross section A, B and C of  $\text{CaCO}_3$  (wt%) over the last 800 ka BP with their respective location marked by red boxes in the lower map. A and B represent SO264 cores with  $\text{CaCO}_3$  prediction by the XRF-ML approach, with age models based on chapter 3. C shows carbonate distribution from Farrell and Prell (1989).

### 7.1.2. Ventilation Age Changes in the Northwest Pacific

The North Pacific is presumed to be a prime candidate for enhanced glacial carbon storage due to its vast size and the accumulation of the oldest water masses in the world ocean. Thus, it is a key region potentially contributing to both glacial lowering of atmospheric CO<sub>2</sub> and anomalously old late glacial to deglacial <sup>14</sup>C. However, evidence for the existence of a large marine bathyal to abyssal reservoir of an “old” carbon are scarce to date. The failure of attempts to find an isolated reservoir in the deep Equatorial Pacific and NE Pacific has historically led to difficulties in explaining the decrease in atmospheric Δ<sup>14</sup>C during the deglacial (Broecker and Barker, 2007; Broecker and Clark, 2010; Broecker et al., 2008), the “mystery interval” (Broecker and Barker, 2007; Lund et al., 2011). However, evidence from the Pacific sector of the Southern Ocean suggests that a glacial deep water mass from the bathyal, i.e. 2000-3500 m depth domain originating in the North Pacific may hold significant amounts of aged, <sup>14</sup>C-depleted carbon (Ronge et al., 2016). Following these studies, radiocarbon measurements on select cores from the study area were initiated from cores in the NW Pacific to identify the ventilation changes in the framework of this thesis and a complementary M.Sc. thesis (Langemann, 2021). Resulting calculated ages on co-existing benthic and planktic (B-P) foraminifera pairs from sediment cores SO202-37-2 and SO264-55-2, bathed in NPDW at water depths of 3568 m and 2936 m, respectively, show a regionalized, inhomogenous pattern (Figure 7.2.2). B-P ventilation ages from SO264-55-2 and implications were presented before (Langemann, 2021). The preliminary results from SO202-37-2 also show anomalously high B-P ventilation ages, with maxima around 5000 years, however in different time intervals compared to maxima of up to 8000 years in SO264-55-2 (Figure 7.2.2). The development of such old ages remains difficult to interpret, compared to previous studies that the ventilation age was around 2000 years (Ronge et al., 2016). Broecker and Barker (2007) had discussed different scenarios that influence atmospheric Δ<sup>14</sup>C changes, it is possible that in the NW Pacific methane addition or hydrothermal activities might have contributed to generate such high ages along scenarios proposed for other regions (Stott et al., 2019a; Stott et al., 2009; Stott and Timmermann, 2011; Stott et al., 2019b). Nevertheless, the preliminary results indicate the existence of an old carbon reservoir during glacials. However, due to the uncertainties in timing and the potential regionalization of the carbon content of deep and bottom water masses in the NW Pacific indicated in the initial data (Figure 7.2.2), further data from additional core sites and water depths are needed to understand the role of the deep water mass geometries and their carbon characteristics. The potentially critical role of North Pacific in CO<sub>2</sub> outgassing, as well

as the size and volumetric extent of this large carbon reservoir still warrant more evidence to be acquired in this region of global significance to Earth's climate and carbon cycle.

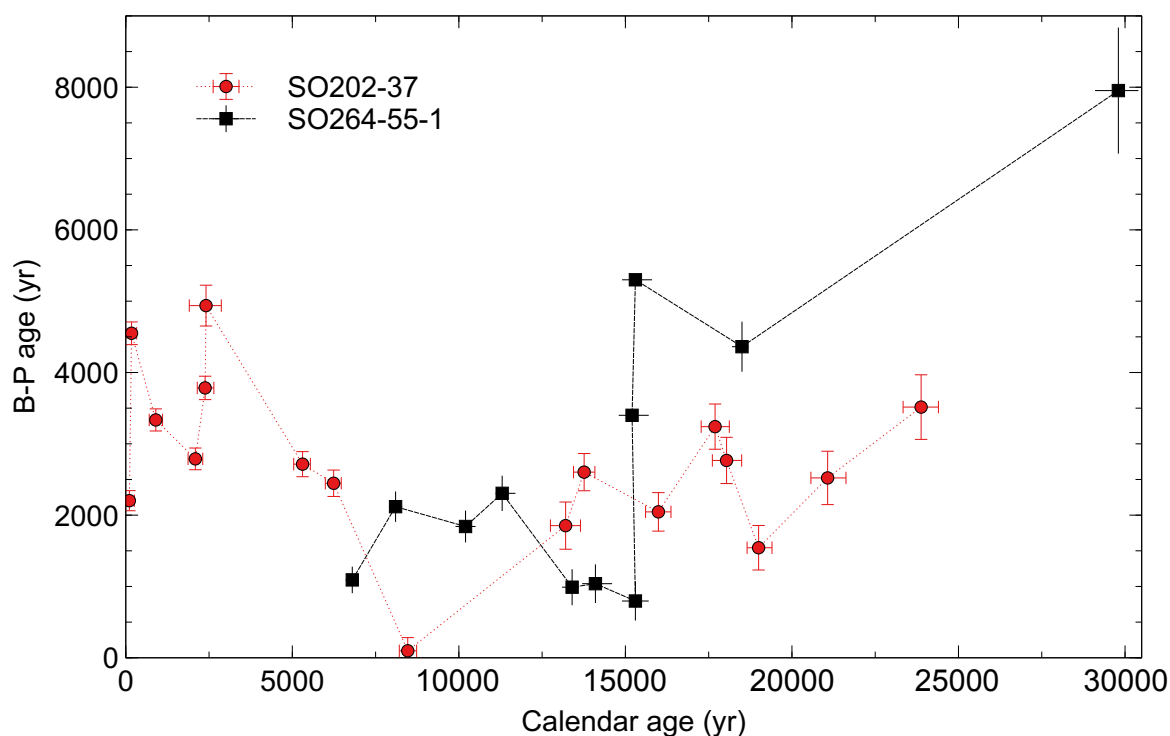


Figure 7.2.2. Benthic-Planktic ventilation ages of cores SO202-37 (combined trigger core SO202-37-1 with piston core SO202-37-2) and SO264-55-1.

## 7.2. References

- Broecker, W. and Barker, S., 2007. A 190‰ drop in atmosphere's  $\Delta^{14}\text{C}$  during the “Mystery Interval”(17.5 to 14.5 kyr). *Earth and Planetary Science Letters*, 256(1-2): 90-99.
- Broecker, W. and Clark, E., 2010. Search for a glacial-age  $^{14}\text{C}$ -depleted ocean reservoir. *Geophysical research letters*, 37(13).
- Broecker, W., Clark, E. and Barker, S., 2008. Near constancy of the Pacific Ocean surface to mid-depth radiocarbon-age difference over the last 20 kyr. *Earth and Planetary Science Letters*, 274(3-4): 322-326.
- Farrell, J.W. and Prell, W.L., 1989. Climatic change and  $\text{CaCO}_3$  preservation: An 800,000 year bathymetric reconstruction from the central equatorial Pacific Ocean. *Paleoceanography*, 4(4): 447-466.
- Langemann, L., 2021. North Pacific Deep Water circulation during the last 160 ka - Implications for the marine carbon pool and atmospheric  $\text{CO}_2$  changes. Master Thesis, Universität Bremen.
- Lund, D.C., Mix, A.C. and Southon, J., 2011. Increased ventilation age of the deep northeast Pacific Ocean during the last deglaciation. *Nature Geoscience*, 4(11): 771-774.
- Ronge, T.A., Tiedemann, R., Lamy, F., Kohler, P., Alloway, B.V., De Pol-Holz, R., Pahnke, K., Southon, J. and Wacker, L., 2016. Radiocarbon constraints on the extent and evolution of the South Pacific glacial carbon pool. *Nat Commun*, 7: 11487.

- Stott, L., Davy, B., Shao, J., Coffin, R., Pecher, I., Neil, H., Rose, P. and Bialas, J., 2019a. CO<sub>2</sub> Release From Pockmarks on the Chatham Rise-Bounty Trough at the Glacial Termination. *Paleoceanography and Paleoclimatology*, 34(11): 1726-1743.
- Stott, L., Southon, J., Timmermann, A. and Koutavas, A., 2009. Radiocarbon age anomaly at intermediate water depth in the Pacific Ocean during the last deglaciation. *Paleoceanography*, 24(2).
- Stott, L. and Timmermann, A., 2011. Hypothesized link between glacial/interglacial atmospheric CO<sub>2</sub> cycles and storage/release of CO<sub>2</sub>-rich fluids from deep-sea sediments. *Geophysical Monograph Series*, 193: 123-138.
- Stott, L.D., Harazin, K.M. and Krupinski, N.B.Q., 2019b. Hydrothermal carbon release to the ocean and atmosphere from the eastern equatorial Pacific during the last glacial termination. *Environmental Research Letters*, 14(2): 025007.
- Zahn, R., Rushdi, A., Pisias, N.G., Bornhold, B.D., Blaise, B. and Karlin, R., 1991. Carbonate deposition and benthic  $\delta^{13}\text{C}$  in the subarctic Pacific: implications for changes of the oceanic carbonate system during the past 750,000 years. *Earth and planetary science letters*, 103(1-4): 116-132.

## **Data Availability of this thesis**

The datasets used and analyzed during this thesis are available on Pangaea and/or from the author or project PI on request.

## **Appendix**

### **i. Additional Manuscript Related to The Thesis**

## **ENSO vs glacial-interglacial-induced changes in the Kuroshio-Oyashio transition zone during the Pleistocene**

Lara Jacobi<sup>1\*</sup>, Dirk Nürnberg<sup>1</sup>, Weng-Si Chao<sup>2</sup>, Lester Lembke-Jene<sup>2</sup>, Ralf Tiedemann<sup>2</sup>

<sup>1</sup>GEOMAR - Helmholtz Centre for Ocean Research Kiel, Kiel, Germany

<sup>2</sup>Alfred-Wegener-Institute - Helmholtz Centre for Polar and Marine Research, Bremerhaven, Germany

\*Corresponding author [ljacobi@geomar.de](mailto:ljacobi@geomar.de)

Keywords: foraminiferal geochemistry, Mg/Ca SSTs, Ba/Ti ratio, North Pacific, Kuroshio, Emperor Seamount chain, Subarctic Front

Submitted to *Frontiers in Marine Science*

Last updated: 20.10.2022

## **Abstract**

The subarctic front (SAF) in the pelagic North Pacific is the northernmost front of the Kuroshio-Oyashio transition zone separating the subpolar- and subtropical gyre and is marked by a strong sea surface temperature gradient. A complex, not yet entirely understood interplay of e.g., variations of currents, the wind system and other forcing mechanisms causes shifts of the SAF's position on timescales from interannual to glacial/interglacial. In this study, we

present proxy data from the Emperor Seamount chain, which reveals a link between long-term ENSO (El Niño/Southern Oscillation) dynamics in the tropics and shifts of the SAF. Based on sediment core SO264-45-2 (46°33.792'N, 169°36.072'E), located close to the modern position of the SAF we reconstruct: changes in (sub)surface temperature ((sub)SST<sub>Mg/Ca</sub>) and  $\delta^{18}\text{O}_{\text{sw-ivc}}$  (approximating salinities) via combined Mg/Ca and  $\delta^{18}\text{O}$  analyses of the shallow-dwelling foraminifera *Globigerina bulloides* and the near-thermocline-dwelling *Neogloboquadrina pachyderma*, biological productivity (XRF-based Ba/Ti ratios), and terrigenous input via dust (XRF-based Fe). From ~600 to ~280 ka BP we observe significantly higher SST<sub>Mg/Ca</sub> than after an abrupt change at 280 ka BP. We assume that during this time water from the Kuroshio-Oyashio transition zone reached the core site which would reflect a shift of the SAF from a position at or even north of our study site prior to 280 ka BP to a position south of our study site after 280 ka BP. We propose that such a northward displacement of the SAF between 600-280 ka BP was induced by sustained La Niña-like conditions, which led to increased transport of tropical ocean heat into the Kuroshio-Oyashio transition zone via the Kuroshio Current. After ~280 ka BP, the change to more El Niño-like conditions led to less heat transfer via the Kuroshio Current so that the SAF remained south of the core location. In contrast, our productivity record shows a clear glacial-interglacial pattern that is common in the North Pacific. We assume that this pattern is connected to changes in nutrient supply or utilization which are not primarily driven by changes of the Kuroshio and Oyashio Currents or the SAF.

## Appendix 1: Cores and measurements done in this thesis

Core ID	Area / Seamount	Latitude	Longitude	Water depth (m)	Core length (m)	XRF	Paleo-mag	Sampled at AWI / GEOMAR	Density	CaCO <sub>3</sub> (TC, TOC)	AMS	Isotope	ICP-MS&OES +Th excess	opal	MUC (+iso)	Bio marker	SS	Pore water
SO202-37-1	northern Hess Rise	37.76861	176.27027	3568	0.19	X		AWI			X	X						
SO202-37-2	northern Hess Rise	37.76861	176.27027	3568	24.35	X	X	sec 1-13	X	X	X	X		X	X	X		
SO264-09-2	Koko	34.78295	172.34978	3865	15.69	X			X									
SO264-13-2	Ojin&Jingu	34.79775	170.72211	3935	13.81	X				X								
SO264-14-1	Nintoku	40.8339	170.90335	3739	18.41	X												
SO264-15-2	east of Ninigi	41.85472	170.51111	3662	14.48	X	X(FIO)	AWI	X	X		X			x	X		
SO264-16-2	east of Ninigi	41.58189	170.42971	3570	14.8	X												X
SO264-19-2	west of Nintoku	41.73055	170.11444	5307	14.37	X	X(Tilo)				surface(?)				x			
SO264-22-2	near Soga	44.0475	171.00083	5704	16.21	X	X(Tilo)								x			
SO264-24-3	Suiko	44.80101	170.59795	4295	14.8	X												
SO264-26-2	Suiko	44.88111	170.25694	1771	16.43	X					surface(?)				x			
SO264-28-2	Suiko	45.00166	170.32305	1935	7.64	X		GEOMAR		X	surface(?)	X			x			
SO264-32-2	Suiko	45.2	170.47777	3200	19.35	X												
SO264-34-2	Suiko	45.03086	170.22588	2622	1.95	X												
SO264-41-2	Suiko	45.945	170.23333	3645	9.47	X	X(FIO)											
SO264-44-2	Jimmu	46.25496	169.33436	1893	2.31	X												
SO264-44-3	Jimmu	46.25511	169.3344	1894	9.26	X												



SO264-45-2	Jimmu	46.77	169.62	2425	8.35	X		GEOMAR			surface(?)	X			x			
SO264-46-5	Minnetonka	46.81568	169.41101	3992	8.93	X												
SO264-47-2	Minnetonka	47.17611	169.53527	2647	6.94	X									x			
SO264-49-2	Minnetonka	47.68115	169.02365	2400	5.87	X												
SO264-51-2	Minnetonka	47.1758	169.42136	2933	7.71	X		AWI								X		
SO264-52-2	Minnetonka	47.12118	169.16448	2752	8	X												
SO264-53-2	Minnetonka	47.89277	169.44916	2325	8.63	X		GEOMAR			surface(?)							
SO264-54-2	Minnetonka	47.705	169.47	2139	11.43	X			X		surface(?)				x			
SO264-55-1	Minnetonka	47.32027	169.4975	2936	15.11	X		GEOMAR	X	X	X	X						
SO264-56-2	Minnetonka	47.94222	169.77722	3973	12.66	X	X(Tilo)	AWI	X	X	X	X	X		x	X	X	X
SO264-57-2	Tenji	48.84691	168.49996	2356	15.4	X												
SO264-60-12	Tenji	49.42333	168.66833	5275	10.57	X	X(Tilo)		X	TOC					x			X
SO264-62-2	north of Tenji	49.95	168.555	2373	15.5	X			MUC		surface(?)				x			
SO264-64-1	south of Detroit	50.12055	168.34666	3495	18.55	X		3 sec. every 10	X	X	surface	X			x			
SO264-66-2	south of Detroit	50.26861	168.51138	2751	15.04	X	X(FIO)		X	X					x			
SO264-69-2	Detroit	50.51461	167.92463	3473	18.55	X	X	AWI	X	X		X					X	
SO264-70-1	Detroit	50.82083	168.14777	3917	5	X									x			
SO264-76-1KAL	Detroit	50.48398	167.85821	3297	4.24	X												

